A 22.2 GHz Antenna for Water Vapour Radiometry

by

William Jacques Cerfonteyn

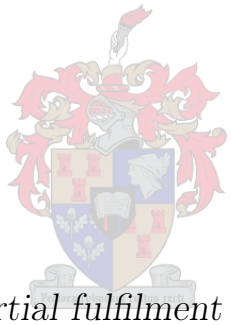

Thesis presented in partial fulfilment of the requirements for the degree of Master of Engineering (Electronic) in the Faculty of Engineering at Stellenbosch University

Supervisor: Prof. D.I.L. De Villiers

April 2019

Declaration

By submitting this thesis electronically, I declare that the entirety of the work contained therein is my own, original work, that I am the sole author thereof (save to the extent explicitly otherwise stated), that reproduction and publication thereof by Stellenbosch University will not infringe any third party rights and that I have not previously in its entirety or in part submitted it for obtaining any qualification.

Date: April 2019

Abstract

A 22.2 GHz Antenna for Water Vapour Radiometry

WJ. Cerfonteyn

Department of Electrical and Electronic Engineering,
University of Stellenbosch,
Private Bag X1, Matieland 7602, South Africa.

Thesis: MEng (Electronic)

November 2018

For this thesis a low-cost antenna solution for a low-cost water vapour radiometry system is designed. The most important specifications for the antenna is that it has to have a -20 dB sidelobe level, a 3° -3 dB beamwidth and have to be electronically steerable. It also has to be low-cost.

The first design that is considered is the phased array solution as it can be electronically steered. Since components can be etched onto the design the manufacturing cost is also reduced. The number of elements required for this design to reach the specifications is determined to be more than 16x16 elements, and thus proves to be cost impractical. The analysis is tested by designing a 1x4 and 2x2 multilayered aperture coupled patch antenna array with a corporate feed network, to both test if a better antenna element design can improve the results, and if the analysis is accurate in determining the impracticality of an array design. This also proves that the array design is infeasible.

A reflector solution is then considered. The reflector system is designed to statically observe in a few specified directions, removing the need for electronic steering. Two parabolic reflectors and a conical horn is designed. The reflectors are combined through interpolation into one larger reflector. After the horn design proves to be ineffective, a new horn is considered that almost allows the reflector system to meet the specifications.

Finally the system is measured, but unfortunately the measured result proves that the physical system does not meet all the specifications. The sidelobe level is around -16 dB, however, the -3 dB beamwidth is well below 3°.

Opsomming

'n 22.2 GHz Antenna vir Water Damp Radiometrie

WJ. Cerfonteyn

Departement Elektriese en Elektroniese Ingenieurswese,
Universiteit van Stellenbosch,
Privaatsak X1, Matieland 7602, Suid Afrika.

Tesis: MIng (Elektronies)

November 2018

Vir hierdie tesis is 'n lae koste antenna oplossing vir 'n lae koste water damp radiometrie stelsel ontwerp. Die belangrikste spesifikasies vir die antenna is dat dit 'n -20 dB sylob vlak het, 'n 3° -3 dB bundelwydte het en elektronies stuurbaar is. Dit moet ook 'n lae koste ontwerp wees.

Die eerste ontwerp wat oorweeg word is die fase stuur samestelling oplossing omdat dit elektronies gestuur kan word. Aangesien die komponente ingeëts kan word in die ontwerp, word die vervaardigings koste ook verminder. Die hoeveelheid elemente wat benodig word vir hierdie ontwerp om die spesifikasies te bereik word bepaal om meer as 16x16 elemente te wees, en dus bewys dit om koste oneffektief te wees. Die analiese is getoets deur die ontwerping van 'n 1x4 en 2x2 multilaag opening gekoppelde mikrostrook antenna samestelling met 'n corporatiewe voer netwerk, om beide te toets of 'n beter antenna element ontwerp die resultate kan verbeter en of die analiese akkuraat is in die bepaling van hoe onprakties die antenna ontwerp is. Hierdie bewys ook dat die antenna ontwerp koste oneffektief is.

'n Reflektor oplossing is dan oorweeg. Die reflektor sisteem is ontwerp om staties in 'n paar spesifieke rigtings te observeer, wat die behoefte vir elektroniese stuurbaarheid verwyder. Twee paraboliese reflektors en 'n koniese horing antenna is ontwerp. Die reflektors is gekombineered deur interpolasie in een groter reflektor. Na die horing ontwerp bewys word om oneffektief te wees, word 'n nuwe horing oorweeg wat amper die reflektor sisteem toelaat om die spesifikasies te bereik.

Uiteindelik word die sisteem gemeet, maar ongelukkig bewys die gemete resultate dat die fisiese sisteem nie al die spesifikasies bereik nie. Die sylob vlak is ongeveer -16 dB, maar die -3 dB bundelwydte is goed onder 3°.

Acknowledgements

I would like to express my sincere gratitude to the following people and organisations ...

Prof. D.I.L De Villiers, for assisting me throughout my entire masters degree project.

Prof. P. Meyer, for helping me pursue this masters degree project.

N.R.F, for providing the financial support necessary for me to finish this project.

University Stellenbosch, for providing me the opportunity to do this masters degree project.

Contents

List of Figures

List of Tables

Chapter 1

Introduction

1.1 Project Overview

Water Vapour Radiometry (WVR) is a field of study with the goal of correcting for signal path length changes which occurs as they travel through the atmosphere. There are many WVRs, which is a physical system designed to determine the amount of electromagnetic radiation that gases radiate, after having absorbed radiation, to determine through some post processing the amount of gases present. The goal of the project is to design a low cost WVR, where this thesis has the goal of designing the antenna for this system.

1.2 Project Participants

The University Stellenbosch works in collaboration with University of Pretoria, Tshwane University of Technology and North-West University to design and implement a low cost Water Vapour Radiometer system. The responsibilities of each are as follows [6]:

1) University Stellenbosch: Antenna Design.

2) University of Pretoria: Receiver components and testing.

3) Tshwane University of Technology: System design and Digital Microwave Engineering.

4) North-West University: Retrieval Algorithms and Site surveys.

1.3 Antenna Design

1.3.1 Antenna Specifications

The antenna designed in this thesis is a proof of concept, meaning it does not reach all the specifications necessary for a working radiometer design. Most specifically, it will not be dual band, but will only function at the 22.2 GHz frequency. The antenna designed for the low cost water vapour radiometry system needs to adhere to the following specifications:

1) Electronically Steered: Even though low cost is the fundamental goal of the project, it is vital that the antenna can be electronically steered, as steering is required to reach the objectives set out for the antenna, thus being able to scan in specific directions to deduce the amount of gas in that area. Mechanical steering, however, leads to requiring maintenance for the motors responsible for ensuring the steering, which increases cost.

2) Low sidelobes: The radiometer, or more accurately the antenna, has to focus in a specific direction to determine the amount of gases in that region. If the sidelobes are high, there would be significant interference or noise from the radiation emitted from the gases outside the region being considered, and as such invalid results would be obtained.

3) Highly directive and narrow beamwidth: This requirement is tied to high gain. By having high gain, there has to be high directivity. The receiving antenna can only be highly sensitive in a certain direction, not in all directions. This is due to the physics argument that if a finite amount of energy is available, then directing the energy will necessarily reduce the energy in the non-directed regions, to adhere to the conservation of energy. It has to be highly directive, so that a certain region of gases can be analysed respectively. With a highly directive antenna, a narrow beamwidth is also implied. The beamwidth in which the antenna is highly sensitive has to be low, if the antenna is highly directive.

4) Low cost and low maintenance: Although this has been stated, it is stated again in bullet form. In theory and practise there are many designs that solves the radiometer problem, as has been implemented in the past, but a low cost design is necessary, also implying low maintenance in this case. This is important as site surveys will be done, where the device will be left in the field for an extended time to do measurements to see if the location is dry enough for millimetre wave radio astronomy. For that purpose no moving parts and low maintenance is wanted.

5) Moderate bandwidth: Due to the nature of high frequency design especially in manufacturing of the components, the tolerances lead to imperfect practical outcomes compared to the theoretical design. This

leads to a physical product that performs differently than expected. In such a case it is crucial that the antenna performs well over a range of frequencies from the centre frequency which it was designed for, so that even with a imperfect physical outcome of the antenna, it still functions properly. The information at the desired frequency is retained while the rest is filtered out at a later stage in the radiometer system.

These specifications listed are necessary for a successful implementation of an antenna that can detect the radiation emitted by atmospheric gases.

1.3.2 Antenna Implementations

To reach the design specifications, two antennas were considered. The first was the Phased Array, specifically the multi-layered aperture coupled patch antenna element array, due to it having a relatively high bandwidth compared to other patch antennas, which is useful for high frequency design, and due to it being able to be electronically steered. The shortcoming of the design proved to be in its cost and implementation to reach the specifications, because of how many elements would be needed to create a three degree -3 dB beamwidth making it impractical for the low cost design requirement.

Secondly, the reflector design, specifically a paraboloidal reflector being fed by multiple horn antennas, was investigated and implemented. An important requirement with this design was the requirement that the design would need to be electronically steerable. For the reflector system, electronic steering is achieved by a switched beam approach, with the system designed for 4 distinct static beams.

Both these designs were done using a combination of Matlab for the analysis and manipulation part of the design and FEKO [7] for the simulation and implementation of the design. The reflector was also analysed in GRASP [8] using ray tracing to determine key characteristics of the reflector design, including the shape of the reflector, its position and the position of the horn antennas. Physical Optics (PO) was also used in GRASP to analyse the electrical behaviour of the reflector system. The reflector was initially comprised of two different reflectors, merged into one reflector, mainly for manufacturing benefit.

This reflector system proved to be a design that could meet the specifications, but only half of it was designed and simulated as it is fully symmetrical around its center plane. This system was then mechanically designed, built and tested.

Finally the reflector system could not reach the specification or theoretical simulation results in its physical form. A less than three degree -3 dB beamwidth

was reached, and is within specification, but the sidelobe level was at about -16 dB, which is -4 dB short of the specification value of -20 dB. The sidelobe level can, however, easily be reduced to specification by using bigger reflectors.

Chapter 2

Water vapour radiometry

2.1 Water Vapour Radiometry Basics

A radiometer is an apparatus designed to determine the level of radiant flux of electromagnetic radiation. Water vapour radiometry is a subcategory of microwave radiometry. A microwave radiometer is a radiometer that operates in the microwave frequency range which quantifies in some cases the amount of thermal electromagnetic radiation of atmospheric gases, where as a water vapour radiometer specifically studies the water vapour/liquid water in the atmosphere.

Microwave radiometers, and always by extension water vapour radiometers, are used in practical applications such as radio astronomy, weather forecasting and climate monitoring. In its application regarding climate and weather, these devices can either function from space or from the ground. It is especially important when they are active in remote regions that they are autonomous and work regularly, which implies needing low maintenance to reduce the frequency and probability of breakdowns.

A black body refers to the concept of an idealised physical body that will absorb all electromagnetic radiation interacting with it, thus no reflection. Black body radiation is the thermal electromagnetic radiation emitted by a black body. Brightness temperature is the temperature a black body has to have while in thermal equilibrium with its environment to mimic the intensity of a grey body, a non ideal body that only partially absorbs and reflects the radiation incident on it, at a specific frequency.

In the microwave region (1 - 1000 GHz), especially in the spectral range (1 - 300 GHz), the atmosphere and vegetation becomes somewhat transparent, which results in water vapour, dry gases and hydro-meteors (rain drops, snow, hail etc.) absorbing and radiating electromagnetic radiation. Vertical temper-

ature, humidity profile, columnar water vapour amount and columnar water vapour paths can all be determined by using microwave radiometers together with radar and lidar technology.

The measure of radiation collected by a microwave radiometer is indicated by brightness temperature. Some atmospheric gases have rotational lines at the microwave frequency range, which shows certain absorption features necessary to obtain information surrounding their vertical structure and how much of the gas is present. A water vapour absorption line is found at 22.235 GHz, which will be the main focus frequency for this thesis, and is used to discover information regarding the vertical profile of humidity. There is also an absorption line at 183.31 GHz, belonging to water vapour absorption, and its purpose is to examine water vapour under dry conditions or from satellites. The absorption line at 183.31 GHz is not being designed for in this thesis, and can be done as further investigation to improve the water vapour radiometry system. Furthermore, an oxygen absorption complex exists around the region of 60 GHz which is needed for temperature profiles. There is also an absorption line at 118.75 GHz, which is an oxygen absorption line.

Additionally, there are also non-resonant contributions from hydro-meteors. The level of radiation that liquid water exerts is a monotonically increasing function of frequency. This has the implication of producing data relevant to the columnar amount of water vapour, as well as the columnar amount of liquid water, respectively, requiring a two channel water vapour radiometer. Two frequency locations are usually considered, the first being at 22.235 GHz which is the water vapour absorption line, and the other at 31 GHz which is dominated by liquid absorption. To have an effective water vapour radiometer one requires both these channels, however, the antenna design in this thesis is only implemented for the 22.235 GHz water vapour absorption line, as it serves as a proof of concept and prototyping phase for a larger project.

2.2 Water Vapour Radiometer Systems

As hinted throughout the text so far a radiometer requires an antenna, which is designed in this thesis. It has a back-end designed to do signal processing. Furthermore, ground based radiometers are normally supplied with environmental sensors such as rain-, temperature- and humidity sensors, and GPS receivers to have a time and location reference. The antenna receives through a foam layer/window to keep the antenna free of dust,water and ice. This foam layer is invisible in the microwave frequency spectrum. Keeping the temperature stable, which is not done in this project yet, is highly important for both avoiding receiver drift but also keeping dew and liquid drops off of the foam layer/window because they are strong emitters in the microwave frequency

region. It is also necessary to keep the system clean of ice and snow. The radiometer thus receives a signal through its antenna, uses a Dicke Switch for high frequency calibration and then a low noise amplifier to boost the signal power, after which a filter removes the noise. It then uses a spectrometer to split the signal into multiple frequencies after which there is a data processing step to interpret the physical measurements into something useful. Figure 2.1 shows a schematic of the described radiometer design.

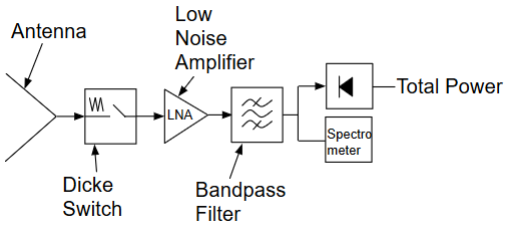

Figure 2.1: Example of radiometer design

An important procedure for a microwave radiometer is its calibration, which leads to accurate brightness temperature readings and by extent accurate data interpretation. Using two black bodies at known but different "hot" and "cold" temperatures, and assuming a linear relation between the input power and output voltage of the detector, their brightness temperatures can be determined and corresponded to the voltages of the detector of the radiometer. This effectively means that the linear relationship between the brightness temperatures and voltages can be found. To convert the radiation received by the microwave radiometer into meaningful physical values require retrieval algorithms.

2.2.1 Water Vapour Radiometer Antennas

As already stated in the Introduction where the Objectives of this Study were discussed, the requirements for a radiometer antenna is stringent, and rightly so. While the exact reasons will not be repeated here, it is of interest to note NASA requirements for their PR-2230 hand held radiometer (Which will not work in this case, since the antenna and radiometer needs to be autonomous). Table 2.1 shows the key requirements:
Of particular interest is the sidelobe level of -30 dB. Reaching this sidelobe level requires a careful antenna design. A goal of -20 dB, which is already low, is more feasible to reach for a low cost design.

Additionally a beamwidth of 3 deg will prove challenging to reach. Finally a bandwidth of 10 - 20% should remove most manufacturing tolerance problems.

Table 2.1: Key radiometer specifications [2]

Parameter	**Specification**
Operating Frequency	22 - 30 GHz selectable in 21 steps
IF Bandwidth	150 MHz double sideband
Antenna Beamwidth	3°
Antenna Sidelobe Level	< -30 dB
Calibrated Brightness Temperature Accuracy	0.2 + 0.002*|Tref-Tsky| K
Measurement Resolution	0.05 K @ 1 s integration time (measured)
Power Requirements	22-30 VDC; 100 W max
Data Interface	ASCII over RS232/RS422/485
Operating Temperature Range	-55° Cel to 55° Cel
Mass	9 kg

Since beamwidth implies gain and directivity requirements, the only requirements that are left is that the antenna has to be electronically steerable and low cost.

2.2.2 Example Systems

NASA launched the Juno spacecraft on August 5, 2011 with the intent of studying various properties of Jupiter, such as the amount of water in Jupiter's atmosphere [9]. Multiple Radiometer antennas are found on the Juno spacecraft, yet at 22 GHz, the frequency the antenna in this thesis is designed for, a corrugated horn antenna was used. Despite any further investigation, it is clear that due to the nature of its antenna class, it will need to be mechanically steered to scan in multiple directions, which makes it non-viable for our design. It is also large and expensive to make. Figure 2.2 shows the antenna designed.

Figure 2.2: Antenna design for the NASA spacecraft Juno [1]

Additionally NASA also constructed ground based radiometers. Figure 2.3 shows such a system. The constraint, as with the horn, is that mechanical

steering is required, invalidating it for the antenna design necessary for this project.

Figure 2.3: Ground based radiometer by NASA [2]

2.2.3 Candidate Antenna Configurations for this Project

For the Water Vapour Radiometer antenna to reach the specified requirements, it is imperative before any other concerns that the antenna can be electronically steered to reduce maintenance costs and keep the system low cost. Even though a reflector would satisfy the rest of the requirements, it would not be electronically steered but can only be mechanically steered. Unless an alternative method can be found to either mimic electronic steering or remove its need all together, a reflector is simply not viable in any capacity. This leads to the candidacy of the Phased Array, which can be electronically steered. The concern with this design is with the amount of elements and general size of the array necessary to reach the specifications set out.

Chapter 3

Phased Array Antennas for Water Vapour Radiometry

3.1 Antenna Basics

The following section is largely done with reference to [10].

An array is a collection of antennas working together to form a single radiation pattern. Electronic steering means the array can observe in different directions by means of using electricity and not a physical mechanism, like a motor used to physically orientate the array in a different direction. Phased Arrays, are normal arrays, but the distinction indicates the implied ability to be electronically steered, meaning no motors are necessary. This means the array does not have to move to change where it is observing which can be very useful.

Antennas have radiation patterns, which describes how sensitive they are to radiating or absorbing energy from certain directions. Due to the reciprocity theorem, antennas radiate energy exactly the same as they absorb energy, meaning an antenna built and simulated using power sources so that it radiates energy can be used to know how the antenna will behave to absorb energy. This is extremely useful in antenna design since a power source can be added to know the radiation pattern, instead of trying to simulate a radiating element somewhere in space accurately and have the antenna react to it. The antennas in this thesis are built using radiating antennas for the design and implementation of absorbing antennas.

A radiation pattern of an directional antenna is shown in Figure 3.1 below. The mainlobe is usually the direction in which the antenna is supposed to be sensitive for radiation (or absorption), and it is this direction which is designed for. The sidelobes and the backlobe is usually unintended, but necessarily re-

sulting directions of sensitivity for radiation. It thus becomes important to maximize the mainlobe, while minimizing the sidelobes (backlobe too), but these goals usually clash and results in a trade-off. The Figure 3.1 shows the antenna's radiation if it was exactly in the middle with a top view (looking from above at the antenna). Usually radiation patterns are described in terms of θ and ϕ directions, where θ is polar angle in 3D (3-Dimensional) space and ϕ is azimuth in 3D space. Thus the Figure 3.1 would be the antennas radiation pattern with the 3D space projected to 2D, eliminating the ϕ component, and observing the antennas radiation sensitivity in the θ direction.

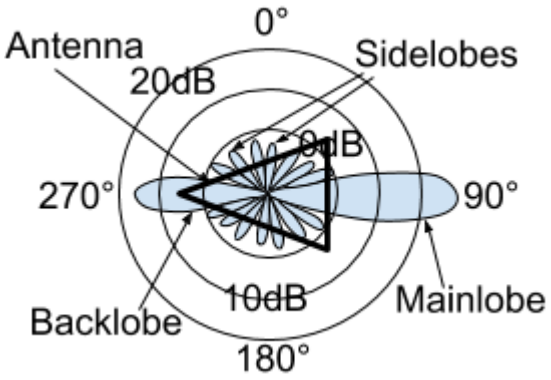

Figure 3.1: Polar Radiation Pattern of antenna

Additionally the Figure 3.2 below shows the Cartesian view of the radiation pattern, where the Figure 3.1 above showed the Polar view. It is assumed the reader knows the different coordinate systems. Both representations are useful and used throughout the text to describe and analyse the radiation patterns of the antennas.

Antennas have distinct field regions where the near field, close to the antenna, are dominated by reactive fields, but the far field far away from the antenna, are dominated by radiating fields, and in this region the radiation pattern is independent of the distance from the antenna. In the spherical coordinate system this distance variable is r if the antenna is placed at the coordinate system origin. Since radiated fields (and the antenna's sensitivity to received fields due to the reciprocal theorem) is of concern, the far field radiation patterns are used. An antenna's (far field) radiation pattern will be described as $(\mathrm{R}(\theta, \phi))$ in this thesis, which is independent of r. The Figure 3.3 below gives a graphical representation of the discussion. The variable λ is the free space wavelength of the wave and is described as $\lambda = \frac{c}{f}$, where c is the speed of light and f is the frequency of the wave.

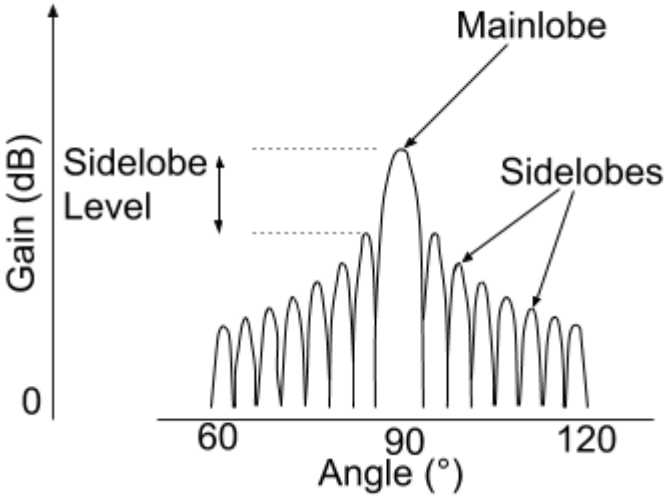

Figure 3.2: Cartesian Radiation Pattern of antenna

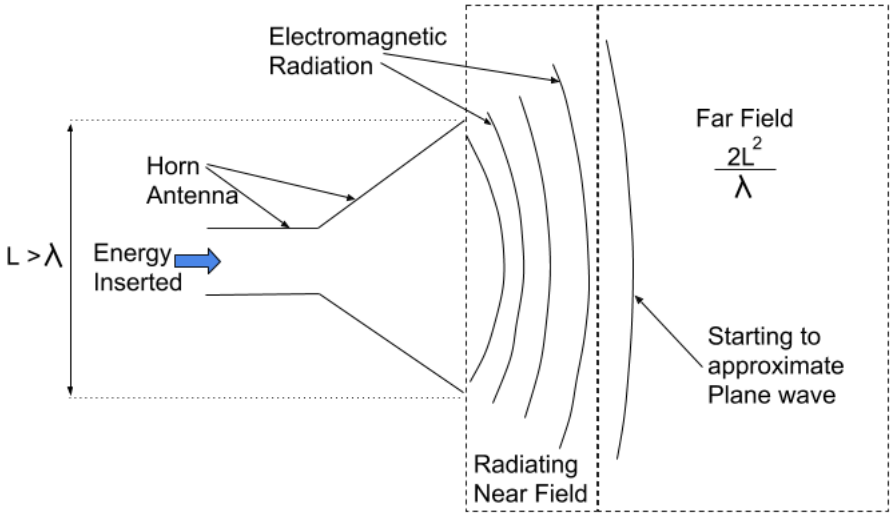

Figure 3.3: Plane wave approximation in far field

3.2 Phased Array Antenna Basics

Arrays are a collection of antenna elements, or more informally, antennas. The goal of an array is usually to combine the radiation of multiple antennas. An important aspect in arrays are phase and directly relates to electronic steering. Consider the Figure 3.4 below, where there are eight antenna elements and they are all connected through feed lines to the (power) source where the energy is injected into the system. They are radiating (narrow band harmonic signals) at different times as indicated by the propagating half ellipses, repre-

senting the propagating electromagnetic waves. This is especially clear when considering the electromagnetic waves just after the antennas radiate them. By delaying radiation it is possible to direct the combined radiation of the antennas by making the radiated electromagnetic waves add up in phase in certain directions. In this case, that direction is the θ direction. Notice that this implies that there is already a phase delay.

The same concept applies if a wave is received. If the wave were to come from the θ direction inwards towards the antenna, then the antennas would receive the wave at the same intervals as they would have radiated the wave. It is important to understand that although this discussion is in terms of time, it is the phase of the wave that matters. The ϕ squares in front of the antennas indicate phase shifters. Phase shifters are responsible for shifting the phase of the wave by a set amount. Thus by shifting the phase of each received or transmitted wave (relative to each other) by a certain amount of degrees, a time delay is implicated in how the waves are radiated. In the event of receiving them, the phase shifters change the phase of the received waves so that in a certain direction they positively interfere, because of the combined wave reaching the source in phase, and in this case in the θ direction. By changing the phase of the phase shifters, the waves add up in another direction, and thus the array is effectively being steered to observe in different directions.

Phase shifters have phase drift. Phase drift introduces error around the phase value of the phase shifter and thus this value does not remain constant or accurate to the expected phase of the phase shifter. This means phase shifters are unreliable in keeping all the signals in phase for a certain direction. The array thus remains sensitive in unwanted directions as radiation in the main direction, or steered direction, is relatively lower compared to the non-steered directions. This is because all the signals no longer add up together in the steered direction and because waves might add up in the unwanted directions, both of which increases the sidelobe level which is generally, and in this case, undesirable.

Notice also that in the direction normal to the θ direction of the Figure 3.4, the radiation starts looking more like a line, or a plane wave in 3D. This is due to the fact that as the spherical energy radiates, and thus expands from the antenna that radiated it, then after a time if a certain portion of the expanded sphere of energy were to be considered, it would appear to be relatively flat. This leads to the fact that as energy radiates, the more distance it propagates, the more it starts acting like a plane wave.

An important characteristic of arrays is that they generally become increasingly more directive, the more elements there are together. Many difficult design specifications can theoretically be reached by combining enough ele-

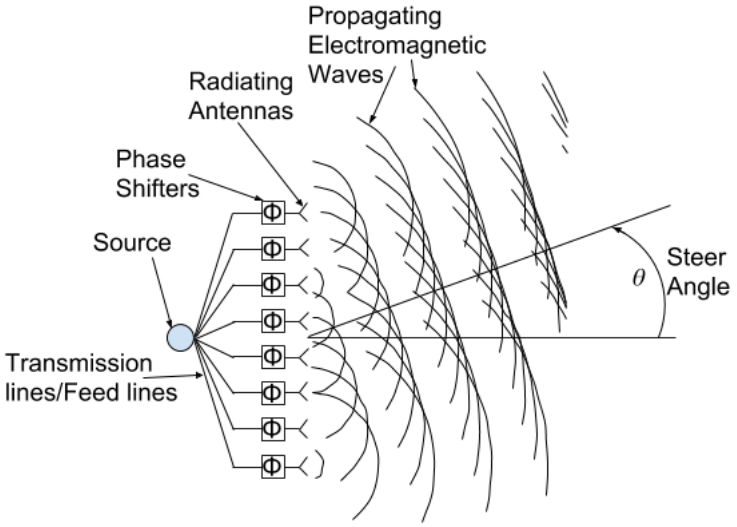

Figure 3.4: Steered Phased Array

ments together, however, it does become a cost constraint when the amount of elements becomes large.

A physical example of an antenna array is shown in the Figure 3.5 below. It is a 2x2 array, consisting of four patch antennas fed by a corporate feed network. Notice that this design does not include a phase shifter. As the energy is launched from the centre, it propagates through the transmission lines and into the antennas. This is an example of a non phased array, since the phase cannot be changed here, the energy will simply travel through the transmission lines into the array and reach it at a certain phase. Notice the symmetry in the system, this is to ensure that all the elements receive the wave at the same time, the same phase. The phase difference between the elements receiving the signal is thus zero, they all receive or propagate the wave at the same time and thus the θ direction here would be zero.

3.3 Electromagnetic Basics

Electromagnetic waves travel at the speed of light. Because these waves are modelled as time harmonic waves, which are periodic, it makes intuitive sense that as the frequency of the signal (or trigonometric function) increases, it will have faster phase changes per second, as the signal has to oscillate quicker between its peaks and valleys. The Figure 3.6 visually displays what is meant.

The wavenumber, k, specifies the phase change of a wave per meter. It is important to note that this value is constrained by the limit that waves moves

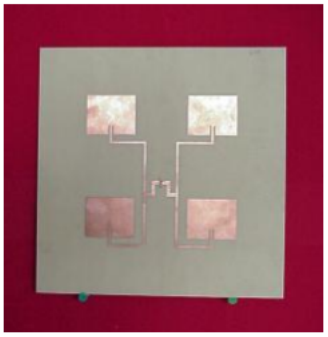

Figure 3.5: Physical 2x2 array

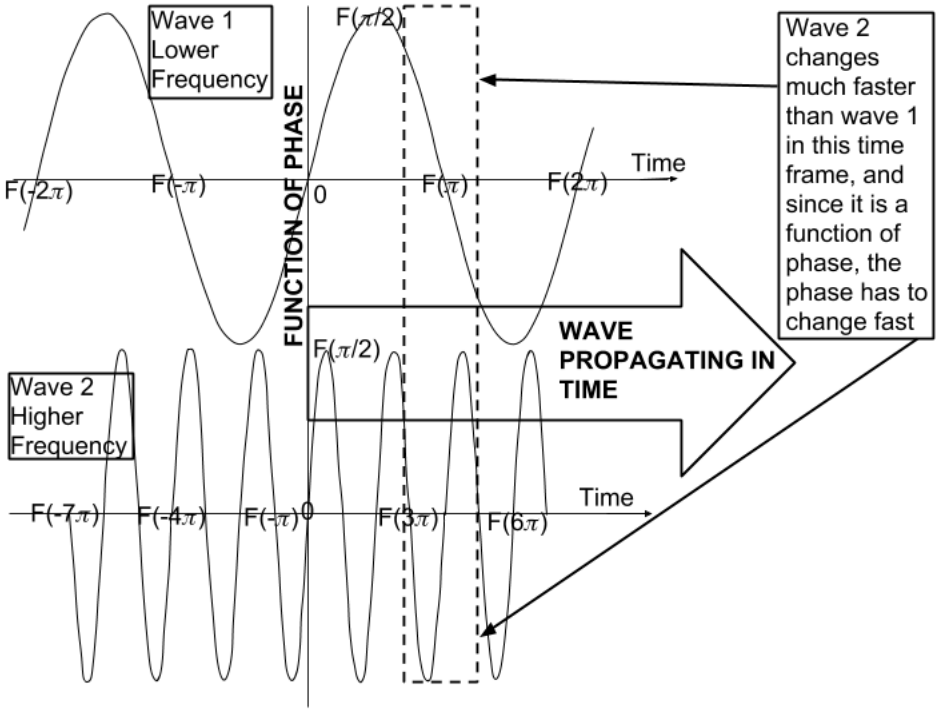

Figure 3.6: Waves travelling in time

at the speed of light, c. The phase change per meter is thus only dependant on a single variable, namely frequency, f, as seen in (3.1):

$$k = \frac{2\pi}{\lambda} = \frac{2\pi f}{c}. \tag{3.1}$$

As the frequency f increases, the phase change per meter linearly increases.

Since the wavenumber is only dependant on a single variable namely frequency, it has to be a scalar value as frequency is a scalar value (all the constants are also scalar), meaning it is independent of the direction the wave travels at. It

is the total phase change the wave experiences per meter.

When the wave travels through a medium, the equation changes slightly as to normalise not with respect to the speed in a vacuum, but to the speed in the medium, as shown in (3.3). The permittivity of a vacuum is denoted as ϵ_0. The relative permittivity of the medium is denoted as ϵ_r. The permeability of a vacuum is denoted as μ_0. The relative permeability of the medium is denoted as μ_r.

$$k = 2\pi f\sqrt{\mu\epsilon} \tag{3.2}$$
$$k = 2\pi f\sqrt{\mu_r\epsilon_r\mu_0\epsilon_0}. \tag{3.3}$$

The wavevector in antennas is used to describe the rate of phase change for a propagating plane wave in 3-orthogonal directions, it is thus the vector format of the wavenumber in 3D, and gives a better description of the phase changes in each direction. This is of course useful due to how the rate of phase change, in each direction, of the plane wave that is incident on an array, determines in which direction it is sensitive. Considering the spherical coordinate system, the conversation to Cartesian is as shown in (3.6):

$$x = r\sin\theta\cos\phi \tag{3.4}$$
$$y = r\sin\theta\sin\phi \tag{3.5}$$
$$z = r\cos\theta. \tag{3.6}$$

If the wave is thus propagating in 3D space,

$$\boldsymbol{k} = (k_x\hat{\boldsymbol{x}} + k_y\hat{\boldsymbol{y}} + k_z\hat{\boldsymbol{z}}) = \tfrac{2\pi}{\lambda}(\sin\theta\cos\phi\hat{\boldsymbol{x}} + \sin\theta\sin\phi\hat{\boldsymbol{y}} + \cos\theta\hat{\boldsymbol{z}}). \tag{3.7}$$

Note the first term is the wavenumber discussed earlier. Since the wavenumber is the phase variation a wave experiences, it is impossible for the total phase variation (so the magnitude) to be more than the wavenumber.

With the understanding of phase variation in plane waves, the fundamental mathematics of antenna arrays can be discussed.

3.4 Antenna Arrays Mathematical Fundamentals

Suppose there is a plane wave travelling to an array:

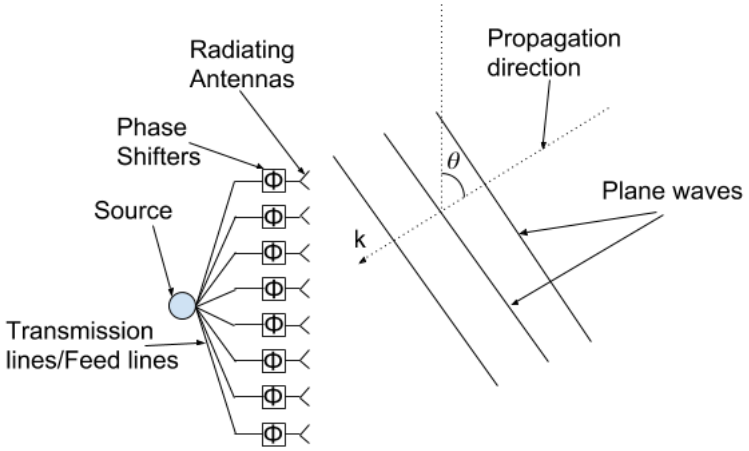

Figure 3.7: Plane wave incident on array

The E-field, or electric field of the plane wave, would have the following mathematical description:

$$E(x,y,z) = e^{-j(k_x\hat{\boldsymbol{x}}+k_y\hat{\boldsymbol{y}}+k_z\hat{\boldsymbol{z}})} \tag{3.8}$$

$$E(x,y,z) = e^{-j|\boldsymbol{k}|(\sin\theta\cos\phi\hat{\boldsymbol{x}}+\sin\theta\sin\phi\hat{\boldsymbol{y}}+\cos\theta\hat{\boldsymbol{z}})} \tag{3.9}$$

$$E(x,y,z) = e^{-j\boldsymbol{k}\cdot\boldsymbol{r}}. \tag{3.10}$$

The mathematical description above makes the following assumptions. First that it propagates in 3D space, using the Cartesian coordinate system, which is why it has an x, y and z component. Then it assumes there is a constant amplitude of one, which is why there is no constant or function in front of the phase term (the exponential term). Notice that in the phase term, the wavevector can be seen. This is because the wavevector determines the plane wave phase variation, so it has to exist in the phase term, and it fully describes it.

The simplification of the equation results in a dot product between the wavevector k and the direction the wave propagates in, r. This effectively mathematically applies the wavevector on the wave in the direction it is travelling in, resulting in an answer that describes the phase variation of the specific propagating wave in each direction, coordinate axis x, y and z.

If the following situation were to be taken:

Three antennas, separated by a distance of a half-wavelength each are connected to form an array. They will receive the plane wave at the exact same x and y coordinates, however, the z coordinate will be a half-wavelength from each previous antenna. Since the phase variation will determine the phase

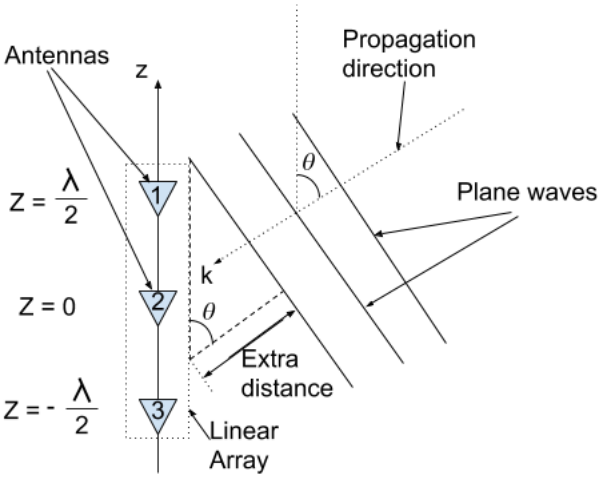

Figure 3.8: Plane wave incident on array

difference at each receiving antenna, it makes sense that if the antennas only receive the wave at a different z coordinate value, then the phase variation of z will be the only difference in phase between the antennas at the point of receiving the signal.

Furthermore, to simplify the discussion, if the antennas are isotropic sensors, then they will have equal sensitivity for the incoming radiation in all directions, thus R(θ, ϕ) = 1. This leads to the following statement:

$$X_i = e^{-j\frac{2\pi}{\lambda}\cos\theta z_i}. \tag{3.11}$$

X_i here denotes the wave each antenna will receive, the only difference is the z_i term which is the z coordinate for each antenna. Notice that the phase term consists only of the phase variation in the z direction. Furthermore, the z_i takes into account each separation distance between the antennas to effectively calculate the phase variation at that point. If all the antennas' received waves add together, then:

$$Y = e^{-j\frac{2\pi}{\lambda}\cos\theta z_1} + e^{-j\frac{2\pi}{\lambda}\cos\theta z_2} + e^{-j\frac{2\pi}{\lambda}\cos\theta z_3} \tag{3.12}$$

$$Y = \sum_{i=1}^{3} e^{-j\frac{2\pi}{\lambda}\cos\theta z_i} \tag{3.13}$$

$$Y = \sum_{m=-1}^{1} e^{-jm\pi\cos\theta}. \tag{3.14}$$

The only difference between the waves is the z coordinate. Since the antennas are separated by a half-wavelength, it reduces to (3.14). Simply substitute the

z values in to take into account the phase variation at those z values.

Finally, notice that due to the cosine term, the expression above will have zero in the exponent of the phase term where $\cos\theta$ is zero, thus at $\theta = 90°$, 270° there will be no phase difference between the received waves. This array is thus not steered at all just yet, and will observe (or be maximally sensitive) at $\theta = 90°$, 270°. If, however, another phase term were to be added (physically adding a phase shifter before each antenna element), to change the phase of the received signals, then the optimal observing direction would not be $\theta = 90°$, 270° any more, but something else. This is how phased arrays are steered electronically.

The phase shifter or extra phase term would have the following format:

$$W_m = e^{jm\theta_d}. \tag{3.15}$$

Notice that if (3.15) where to be inserted into (3.14) above (thus add a phase shifter before each element physically and mathematically another phase term), it would change the zero point of the exponent. This is shown in (3.19) below.

$$W_m = e^{jm\theta_d} \tag{3.16}$$

$$Y = \sum_{m=-1}^{1} e^{-jm\pi\cos\theta} e^{jm\theta_d} \tag{3.17}$$

$$Y = \sum_{m=-1}^{1} e^{-jm\pi\cos\theta + jm\theta_d} \tag{3.18}$$

$$Y = \sum_{m=-1}^{1} e^{-jm\pi(\cos\theta - \theta_d)}. \tag{3.19}$$

If the phased array is to be steered to S, then the following equation describes the value of θ_d to achieve this:

$$\theta_s = S \tag{3.20}$$

$$d = \frac{\lambda}{2} \tag{3.21}$$

$$k = \frac{2\pi}{\lambda} \tag{3.22}$$

$$\theta_d = kd\cos(\theta_s). \tag{3.23}$$

Now instead of having an isotropic sensor, an antenna element with a radiation pattern of R(θ, ϕ) is used.

Also assume now that phase shifters have been added before each antenna

element, or even more generally, a weight, carrying both magnitude and phase adjustments to the wave received by the antenna element. By taking the general case as shown in Figure 3.7 the following equation changes from,

$$E(x, y, z) = e^{-j\boldsymbol{k}\cdot\boldsymbol{r}} \tag{3.24}$$

$$Y = e^{-j\boldsymbol{k}\cdot\boldsymbol{r_1}} + e^{-j\boldsymbol{k}\cdot\boldsymbol{r_2}} + ... + e^{-j\boldsymbol{k}\cdot\boldsymbol{r_N}}, \tag{3.25}$$

to,

$$Y = w_1 e^{-j\boldsymbol{k}\cdot\boldsymbol{r_1}} + w_2 e^{-j\boldsymbol{k}\cdot\boldsymbol{r_2}} + ... + w_N e^{-j\boldsymbol{k}\cdot\boldsymbol{r_N}}, \tag{3.26}$$

and finally, by using a non-isotropic antenna element,

$$Y = R(\theta, \phi) w_1 e^{-j\boldsymbol{k}\cdot\boldsymbol{r_1}} + R(\theta, \phi) w_2 e^{-j\boldsymbol{k}\cdot\boldsymbol{r_2}} + ... + R(\theta, \phi) w_N e^{-j\boldsymbol{k}\cdot\boldsymbol{r_N}}. \tag{3.27}$$

Notice also how the phase term is written generally. This equation has the generalisation that the elements need not be ordered in the z axis as they were previously defined in the explanation of phase importance in arrays.

Careful inspection of the equation above, leads to the following simplification:

$$Y = R(\theta, \phi) \sum_{i=1}^{N} w_i e^{-j\boldsymbol{k}\cdot\boldsymbol{r_i}} \tag{3.28}$$

$$Y = R(\theta, \phi)\mathrm{AF} \tag{3.29}$$

$$\mathrm{AF} = \sum_{i=1}^{N} w_i e^{-j\boldsymbol{k}\cdot\boldsymbol{r_i}}. \tag{3.30}$$

AF is known as the array factor. As previously stated by changing the weights, adding a phase shifter for example before each antenna element, the antenna can be steered to observe in a different direction. Additionally, this begs the question of what techniques exist to determine which array factor would be best suited for a specific goal. Changing the phase leads to steering, but changing the amplitude or magnitude of each antenna element's received or transmitted wave respectively, through using the weights, leads to the changing of the resulting radiation pattern of the array, which is useful to reduce sidelobes.

As noted earlier, the sidelobes of the radiation pattern are not all equal in magnitude. The sidelobe level, however, is measured from the highest sidelobe's magnitude to the main beam's magnitude. Thus it would be effective if the sidelobes' energy could be distributed in such a manner that they all are the same level. This would reduce the sidelobe level which is important. This is shown in Figure 3.10. Figure 3.9 shows no weight modification.

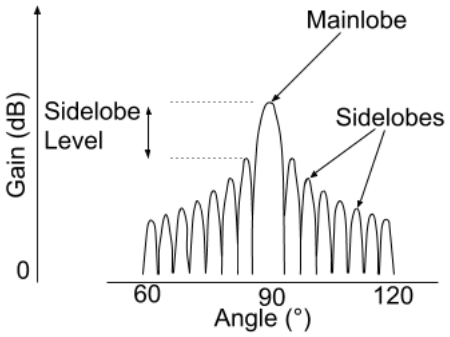

Figure 3.9: Cartesian Radiation Pattern of antenna

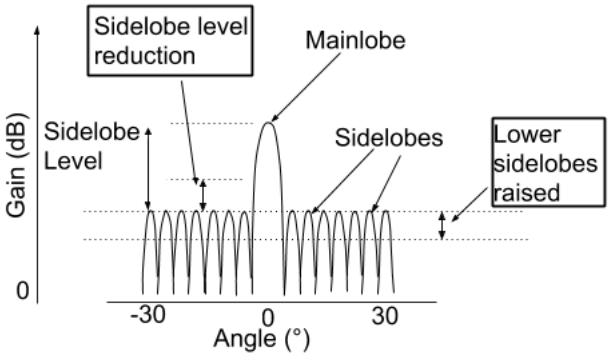

Figure 3.10: Magnitude modification leading to sidelobe level reduction

3.5 Dolph-Chebyshev (Chebyshev) Method

The Dolph-Chebyshev or Chebyshev (sometimes spelt Tschebyscheff) technique does just this. The technique allows the specification of a certain desired sidelobe level that all the sidelobes will be at and produces the weights necessary in the array factor to yield it. It also provides the smallest half-power (main) beamwidth (thus -3 dB from the direction of the mainbeam) that can be obtained with that sidelobe level. This is equally important in ensuring the sensitivity of the array in the mainbeam's direction, so that a precise area can be observed, without much noise from the surrounding area. When beamwidth is mentioned it refers to HPBW, or half-power beamwidth. The HPBW is visually described in Figure 3.11 below.

While this seems very useful the technique was designed for a certain situation. The technique is designed for arrays steered to broadside $\theta_d = 90°$. Thus the weights produced leads to a radiation pattern that has equal level sidelobes, and the smallest beamwidth possible for the equal sidelobe level, for a

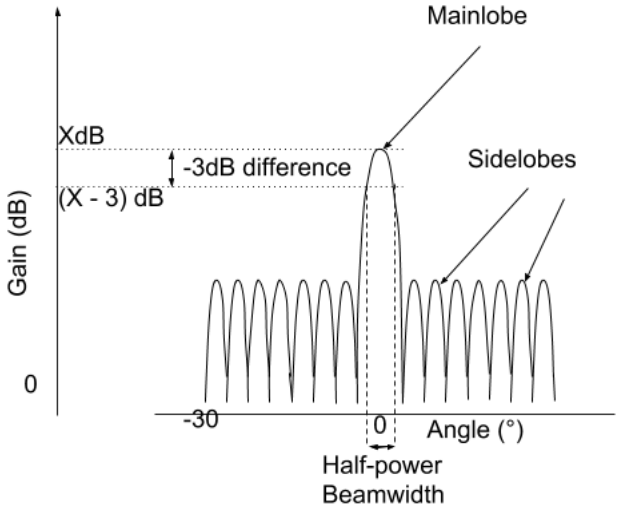

Figure 3.11: Half-power (-3 dB) beamwidth described

broadside array. This will give an indication of how well the array performs in a broadside situation, and how feasible the array design is before starting to design a steered system.

There are other techniques too, that serve different purposes. For example the uniform weights, thus equal amplitudes, lead to the smallest mainlobe beamwidth, but the sidelobes are higher than with Chebyshev. The binomial weights lead to smaller sidelobes than Chebyshev, but a higher mainlobe beamwidth. Since both of these specifications are important to reach, the middle option was chosen.

The Chebyshev technique presented below was largely obtained from two lectures [11], [12] and the Antenna Theory textbook from Balanis [10].

The Chebyshev polynomials (will always refer to the first order Chebyshev polynomials in this thesis) all have equal amplitudes (of 1) in the range from $-1 \leq z \leq 1$. Some of these polynomials are shown in the figure below.

These polynomials have the relationship as indicated in the next equation, where m is the order of the polynomial:

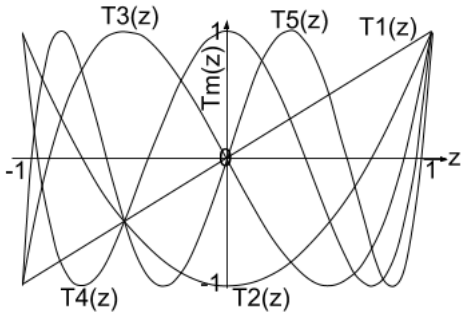

Figure 3.12: Chebyshev Polynomials

$$
\begin{aligned}
T_0(z) &= 1 \qquad m = 0 \\
T_1(z) &= z \qquad m = 1 \\
T_2(z) &= 2z^2 - 1 \quad m = 2 \\
T_3(z) &= 4z^3 - 3z \quad m = 3 \\
T_4(z) &= 8z^4 - 8z^2 + 1 \quad m = 4 \\
T_5(z) &= 16z^5 - 20z^3 + 5z \quad m = 5 \\
T_m(z) &= 2zT_{m-1}(z) - T_{m-2}(z), \quad m = 2, 3, ... \qquad (3.31)
\end{aligned}
$$

It can also be presented in the following manner:

$$T_m(z) = \cos\left(m \cos^{-1} z\right), \qquad -1 \leq z \leq 1 \qquad (3.32)$$

$$T_m(z) = \cosh\left(m \cosh^{-1} z\right), \qquad z < -1, z > 1. \qquad (3.33)$$

If, somehow, these polynomials with their coefficients could be matched to the array factor, then the array factor would have equal ripple which leads to all the sidelobes having the same sidelobe level. This is the idea of the Dolph-Chebyshev technique.

Consider a situation where all the elements are positioned on the z axis (a linear array design), and the array and the weights are both symmetric around the y axis. The number of elements are N. The value of the product dn for an odd number of elements, or $d\frac{(2n-1)}{2}$ for an even number of elements, is the z coordinate of the elements, respectively, where d is the distance between each element and n (which is a natural number) is the element being considered. The Figure 3.13 below shows such a case visually.

The array factor for an array with an even number of elements, where the number of elements, N, is equal to $N = 2M$, is written as shown in (3.34) below. Since the weights are symmetric around the y-axis, $w_n = w_{-n}$.

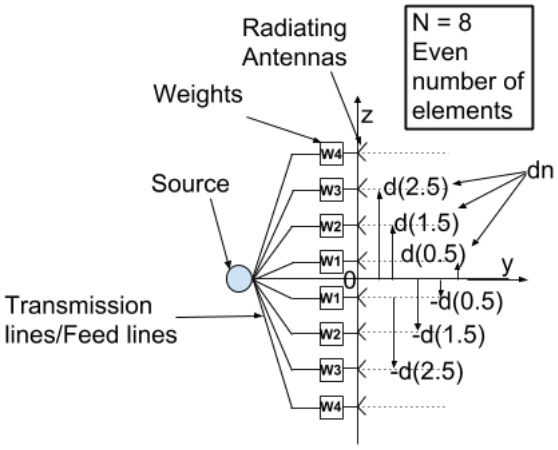

Figure 3.13: A linear array design with weights

$$\text{AF} = \sum_{n=1}^{M} w_n e^{-jk(2n-1)\frac{d}{2}\cos\theta} + \sum_{n=-M}^{-1} w_n e^{-jk(2n+1)\frac{d}{2}\cos\theta}. \tag{3.34}$$

The array factor for an array with an odd number of elements, where the number of elements, N, is equal to $N = 2M + 1$, is written as:

$$\text{AF} = \sum_{n=-M}^{M} w_n e^{-jknd\cos\theta}. \tag{3.35}$$

Notice also that there is no θ_d variable here. This array factor is for an array that is implicitly steered to broadside where $\theta = 90°$. These array factors have cosine components. By considering the complex exponential formula for the cosine function:

$$\cos\theta = \frac{e^{j\theta}+e^{-j\theta}}{2}, \tag{3.36}$$

the array factor, for an even and odd array respectively, can be rewritten as shown in (3.37) below. Note again, $w_n = w_{-n}$ and $\frac{w_n}{2}$ is chosen as w_n. An explanation on this is given below.

$$\begin{aligned} \text{AF} &= \sum_{n=1}^{M} w_n \cos\left((2n-1)u\right) \qquad \text{(EVEN)} \\ \text{AF} &= \sum_{n=0}^{M} w_n \cos\left(2nu\right) \qquad \text{(ODD)} \\ u &= \tfrac{kd\cos\theta}{2}. \end{aligned} \tag{3.37}$$

It can also be written as below, where $a_n = w_n$:

$$(\mathrm{AF})_{2M} = \sum_{n=1}^{M} a_n \cos\left(\tfrac{(2n-1)}{2} kd\cos\theta\right) \quad \text{(EVEN) } N = 2M \tag{3.38}$$

$$(\mathrm{AF})_{2M+1} = \sum_{n=1}^{M+1} a_n \cos\left((n-1)kd\cos\theta\right) \quad \text{(ODD) } N = 2M+1 \tag{3.39}$$

$$(\mathrm{AF})_{2M} = \sum_{n=1}^{M} a_n \cos\left((2n-1)u\right) \quad \text{(EVEN) } N = 2M \tag{3.40}$$

$$u = \tfrac{kd\cos\theta}{2} = \tfrac{d\pi\cos\theta}{\lambda}. \tag{3.41}$$

During the simplification (which is not explicitly shown as it is straight forward mathematics) the $\frac{w_n}{2}$ simplifies to w_n as the term is simply a weight and the coefficients are combined in it.

The array factor can be expanded into a polynomial equation and (the coefficients) matched with the Chebyshev polynomials to calculate weights for equal level sidelobes.

To further clarify this expansion, an example for the array factor for an $N = 6$ array is shown below:

$$\mathrm{AF}_6 = a_1\cos(u) + a_2\cos(3u) + a_3\cos(5u). \tag{3.42}$$

The cosine terms can be expanded into powers of cosines:

$$\cos(3u) = 4\cos^3 u - 3\cos u \tag{3.43}$$

$$\cos(5u) = 16\cos^5 u - 20\cos^3 u + 5\cos u. \tag{3.44}$$

Only the odd cosine arguments, as shown above, are of importance due to the array factors shown above only having odd cosine arguments. The array factor can thus be rewritten in terms of cosine powers.

Consider the following comparison:

$$T_3(z) = 4z^3 - 3z \quad m = 3 \tag{3.45}$$

$$\cos(3u) = 4\cos^3 u - 3\cos u \tag{3.46}$$

$$T_5(z) = 16z^5 - 20z^3 + 5z \quad m = 5 \tag{3.47}$$

$$\cos(5u) = 16\cos^5 u - 20\cos^3 u + 5\cos u. \tag{3.48}$$

Thus, the cosine functions' expansions as shown above are related to the Chebyshev polynomials if -1 $\leq$ z $\leq$ 1. The cosines and the Chebyshev polynomials have amplitudes of 1, between -1 $\leq$ z $\leq$ 1. The Chebyshev argument z is related to the cosine argument u as shown in the equation below:

$$z = \cos u \tag{3.49}$$
$$u = \cos^{-1} z. \tag{3.50}$$

Thus, for example, $\cos(3u)$ and $T_3(z)$ are related as shown below. The same procedure can be followed for the other cases to arrive at similar comparisons.

$$\cos(3u) = \cos(3\cos^{-1} z) = 4(\cos(\cos^{-1} z))^3 - 3\cos(\cos^{-1} z) \tag{3.51}$$
$$= 4z^3 - 3z = T_3(z). \tag{3.52}$$

The z_0 variable is used to determine the coefficients to ensure equal level sidelobes for a specific sidelobe level. The point $z = z_0$ has to be found so $T_{N-1}(z_0) = R_0$, where R_0 is the sidelobe level chosen. The design method requires that the Chebyschev polynomial in the range $-1 \leq z \leq z_1$, where z_1 is the null nearest to $z = 1$, be used to represent the minor lobes of the array. The major lobe of the pattern is formed from the remaining part of the polynomial up to point $z_0(z_1 < z \leq z_0)$. The substitution changes to:

$$\frac{z}{z_0} = \cos u. \tag{3.53}$$

With this substitution the entire array factor can be written as a polynomial with no trigonometric functions present and matched to the Chebyshev polynomials to produce equal level sidelobes.

The z_0 variable has to be calculated and is dependant on the sidelobe level R_0 chosen as follows:

$$T_{N-1}(z_0) = \cosh(N-1)\cosh^{-1} z_0 = R_0. \tag{3.54}$$

Rewriting this equation by making the z_0 variable the subject leads to:

$$z_0 = \cosh(\tfrac{\cosh^{-1} R_0}{N-1}). \tag{3.55}$$

By using the (3.55) above, z_0 can be determined. All that remains now is to match the array factor polynomial expansion to the chebyshev polynomial and to obtain the coefficients. The array factor will then assume the same behaviour the Chebyshev polynomials has which is to have equal sidelobes. Note that the order of the Chebyshev polynomial to which the array factor's coefficients will be matched will always be one less than the number of elements, N. This is because this polynomial has the same form as the array factor and can thus be matched. This will be made clear in an example, below.

Finally, a quick partial example is shown to finish the discussion on the Chebyshev technique. For a 4 elements ($N = 4$) array, the array factor is:

$$\mathrm{AF}_4 = a_1 \cos(u) + a_2 \cos(3u). \tag{3.56}$$

Using the cosine power expansion in (3.57) below:

$$\cos(3u) = 4\cos^3 u - 3\cos u. \tag{3.57}$$

The array factor expands to:

$$\mathrm{AF} = a_1 \cos(u) + a_2(4\cos^3 u - 3\cos u) \tag{3.58}$$
$$\mathrm{AF} = \cos(u)(a_1 - 3a_2) + \cos^3 u(4a_2) \tag{3.59}$$
$$\mathrm{AF} = \tfrac{z}{z_0}(a_1 - 3a_2) + \tfrac{z^3}{z_0^3}(4a_2). \tag{3.60}$$

This array factor now has to be matched with the Chebyshev polynomial of order $(N-1)$:

$$T_3(z) = 4z^3 - 3z. \tag{3.61}$$

The variable z_0 is calculated using the chosen sidelobe level, R_0, and the number of elements, N:

$$z_0 = \cosh(\tfrac{\cosh^{-1} R_0}{N-1}). \tag{3.62}$$

Matching the coefficients leads to the following equation:

$$\tfrac{z}{z_0}(a_1 - 3a_2) + \tfrac{z^3}{z_0^3}(4a_2) = 4z^3 - 3z \tag{3.63}$$
$$4a_2 = 4z_0^3 \tag{3.64}$$
$$a_1 - 3a_2 = -3z_0. \tag{3.65}$$

At this point, the coefficients (or weights) a_1 and a_2 can be calculated.

3.6 Investigation into array solution feasibility

One of the questions when designing arrays is how far the elements should be from each other. One of the problems that arises when the elements are relatively far apart is grating lobes.

Grating lobes are main lobes in undesired directions and can thus be considered an exaggerated sidelobe. It is generally considered a priority to design so that the system does not have any grating lobes. For uniformly spaced linear arrays (ULAs) grating lobes will start occurring when the elements are spaced more than a wavelength apart and sometimes at closer spacings. Scanning can also lead to grating lobes appearing. In this thesis antenna elements will be no further away from each other than $\frac{1}{2}$ a wavelength.

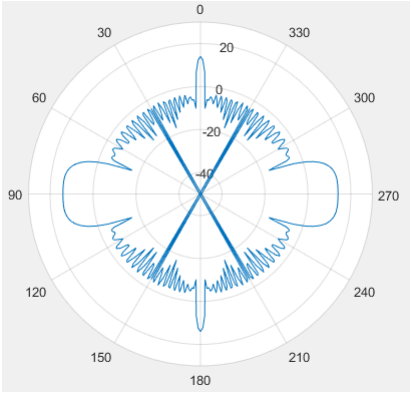

Figure 3.14: Polar far field pattern. Grating lobes present at sides

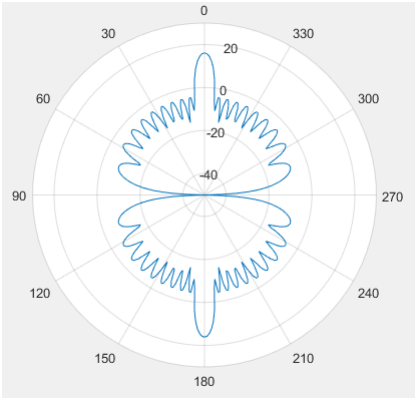

Figure 3.15: Polar far field pattern. No Grating lobes present at sides

The figures' Figure 3.14 and Figure 3.15 describes a linear half wavelength (0.48λ to be exact) dipole array pattern for both a wavelength spacing and a $\frac{1}{2}$ wavelength spacing, respectively. When discussing dipoles in this thesis, it refers to half wavelength dipoles. Clearly at a wavelength spacing there are grating lobes present, which are noticed as the two lobes at each side. This is removed when the spacing is closer together at $\frac{1}{2}$ wavelength.

One of the biggest questions when considering an array solution to the low-cost water vapour radiometer antenna problem is how many elements will be required to achieve this goal. By using the Chebyshev technique the sidelobe levels can be tuned, however, a mainlobe beamwidth is still associated with that sidelobe level for a specific number of elements, N. To reduce the mainlobe beamwidth too, the number of elements have to be increased. This question is especially pertinent since a low-cost solution is required - more elements increases the cost.

Firstly, when designing an array, the more elements work together in the array, the narrower the mainlobe beam will become. This is because more elements have their radiating waves add up in phase in the direction it has been steered, to raise the gain or directivity in that direction.

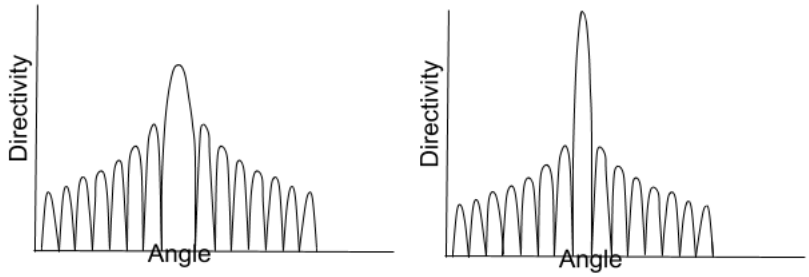

Figure 3.16: Higher directivity leads to lower beamwidth

The two primary factors affecting the beamwidth of the mainlobe or the directivity, is the array factor, which is independent of the elements the array consists of, and the other important factor is the elements themselves that the array is made up of. Since the biggest contribution stems from the array factor, a dipole element can be used in the array for an analysis on how many elements are required to achieve a relatively high directivity. If this analysis yields an answer which seems reasonable, the elements will also be specifically designed to determine the performance of the system.

The total gain pattern of the array (assuming no coupling) is the product of the radiation pattern of the antenna element used in the array, and the array factor. If only the array factor is to be analysed in isolation, an isotropic antenna element needs to be chosen. Isotropic elements are elements which radiates the same amount of electromagnetic energy in all directions or have a directivity of 1 (or 0 dB). Since isotropic elements are ideal elements and do not exist physically, an alternative is to use an omnidirectional antenna.

Omnidirectional antennas radiate the same amount of electromagnetic energy over a certain angle, but not in all directions. If, however, the radiation pattern is considered over the angle in which the pattern radiates equally, it resembles an isotropic element over that region, with the only difference being a constant magnitude that it is higher than an isotropic element's. This makes sense as the energy that is not radiated in the other directions is now added in this section. When considering the total gain pattern, the only effect the omni directional antenna element would have over the region in which it radiates equally is to multiply the total gain by a constant. The rest of the contribution would be due to the array factor. Using this approach makes it possible to isolate the effect of the array factor, especially the effect it has on increasing the directivity (narrowness of the main beam) of the total gain pattern, in which the omnidirectional antenna would have no contribution due to it's equal radiation over that region.

Figure 3.17 shows the 3D radiation pattern of an omnidirectional antenna. Figure 3.18 shows, from left to right, an isotropic antenna's 3D radiation pattern and a directive pattern in 3D. The equation below shows mathematically the total gain pattern relation to the array factor when using an omnidirectional antenna.

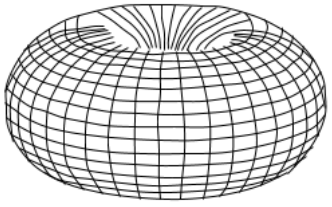

Figure 3.17: Omnidirectional radiation pattern in 3 dimensions

$$Y = R(\theta, \phi) \sum_{i=1}^{N} w_i e^{-jk \cdot r_i} \tag{3.66}$$

$$Y = R(\theta, \phi)\mathrm{AF} \tag{3.67}$$

$$R(\theta, \phi) = 1 \quad \mathrm{ISOT} \tag{3.68}$$

$$R(\theta, \phi) = C \quad \theta = 90, \mathrm{OMNI} \tag{3.69}$$

$$Y = CAF \quad \theta = 90, \mathrm{OMNI}. \tag{3.70}$$

$$\tag{3.71}$$

To determine how many elements would be required to reach the specifications for the low-cost water vapour radiometer antenna design, a full goal pattern

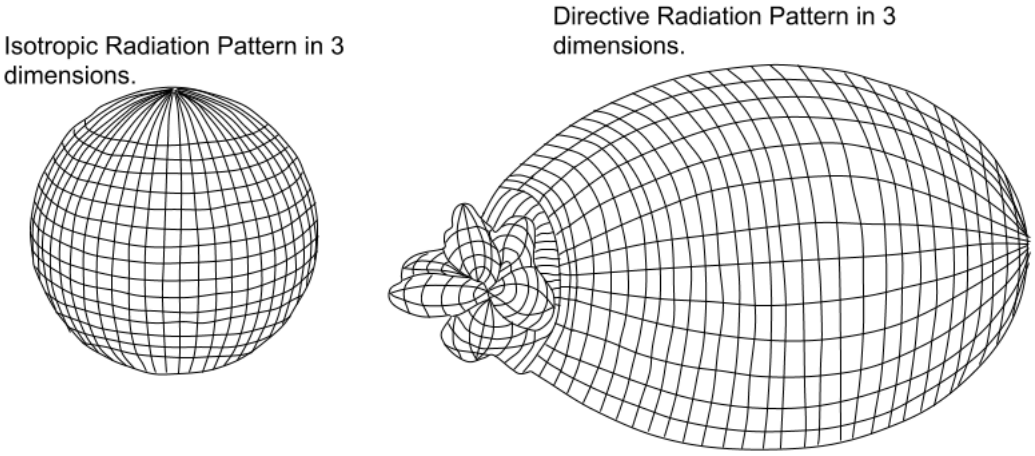

Figure 3.18: Isotropic and Directive patterns in 3 dimensions, respectively

was first created. The radiation pattern of the array design will try to be approximated as the full goal pattern. The full goal pattern does not come from a simulation, it is created by determining the Chebyshev excitations or weights for a relatively large number of elements $N = 14$, so that the beamwidth can be adequately reduced, and then an array factor is created using those weights. The large number of elements reduces the mainbeam beamwidth, while the sidelobe level is set to -20 dB using the Chebyshev technique. The resulting full goal pattern can be seen in Figure 3.19.

The full goal pattern is also steered to 30° from broadside. Steering away from broadside increases the beamwidth. This is because the perceived aperture forming the steered beam reduces as the steering angle increases. Reduced aperture increases the beamwidth, and is explained in more detail in Chapter 4. Figure 3.20 describes the discussion visually. Thus if the array design functions well at the steered angle, it will function well if not steered at all. It is important to design with steering in mind, as the array has to be able to steer and retain acceptable performance.

As this full goal pattern is created using only an array factor, it implies that there is no antenna element contribution, or that the antenna elements are isotropic. If, however, an antenna element were to be used that were non-isotropic, but had a directive pattern, then more elements would be required to reduce the beamwidth to an acceptable level.

This is because the total gain pattern is the product of the element pattern and the array factor. When the array factor is steered, the product at the steered angle is that of a sidelobe of the element pattern and the mainbeam of the array factor. The product is thus notably reduced, compared to if it

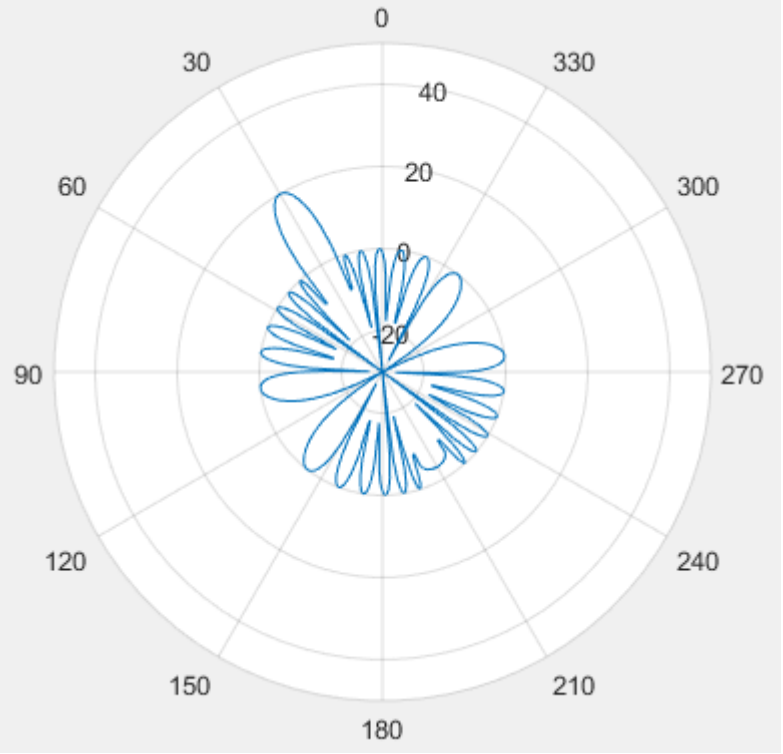

Figure 3.19: Full goal pattern

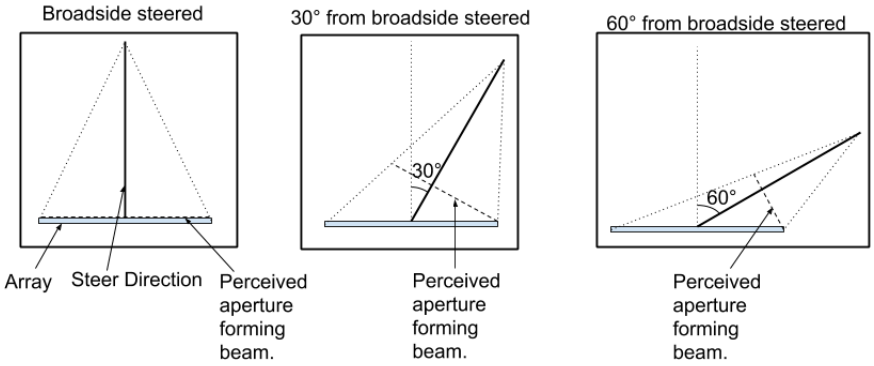

Figure 3.20: Steering away from broadside increases the beamwidth

would be a isotropic element pattern. This is shown in Figure 3.21.

Thus, for the array design to reach the beamwidth of the full goal pattern, more than 14 elements would be required.

After the full goal pattern has been created, an array is created in FEKO and simulated. This array consists of microstrip patch antenna elements. The reason for this is that the design will likely require a microstrip patch antenna

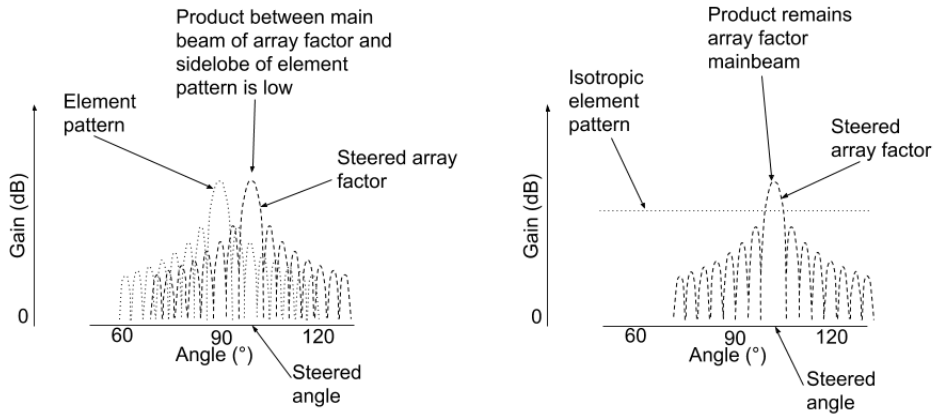

Figure 3.21: Directive element pattern reduces beamwidth of array at steered angle

element as the components can be etched onto the structure which reduces cost, as opposed to dipoles.

As an aside, the Chebychev technique does enable the setting of the sidelobe level, but this is only valid for the array factor. As soon as an element pattern is introduced, the sidelobes will necessary change as the total pattern is the function of both the element pattern and the array factor. Thus, unequal sidelobes are expected from the simulated design.

The amount of elements, N, is sent to FEKO from Matlab. After the array creation and simulation, it returns N embedded element patterns (EEP) to Matlab. An EEP is created by zeroing all the other sources for the other antennas in the array, except for the current antenna, and loading them with their source's characteristic impedance. The radiation pattern is then simulated and that EEP is obtained. This process is repeated for all the antenna elements and thus N EEPs are made. The EEPs were made from sources with uniform weights (not Chebyshev) and no phase steering.

In Matlab, the total gain pattern of the array simulation is found by summing all the EEPs together as shown in (3.72) below. The EEPs takes the effect of mutual coupling between the elements into account as well, which is important to model as this effect will exist in a physical implementation. Figure 3.22 shows the total gain pattern for the array at $N = 8$ amount of elements.

$$Y = \sum_{n=1}^{N} \text{EEP}_n. \tag{3.72}$$

The EEPs are then multiplied with a phase term to steer the pattern and

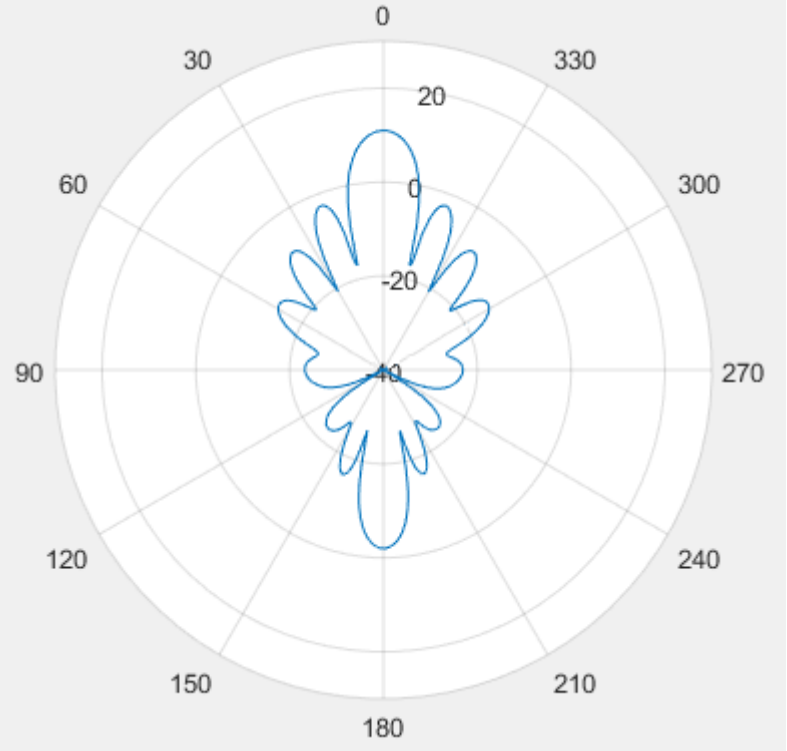

Figure 3.22: Total gain pattern from summing EEPs using uniform weights and no steering

Chebyshev weights to reduce the sidelobes. This is shown in (3.77) below, and Figure 3.23 shows the resulting pattern.

$$\theta_a = 30 \tag{3.73}$$
$$d = \frac{\lambda}{2} \tag{3.74}$$
$$k = \frac{2\pi}{\lambda} \tag{3.75}$$
$$\theta_s = kdcos\theta_a \tag{3.76}$$
$$Y = \sum_{n=1}^{N} w_n e^{-jn\theta_s} \mathrm{EEP}_n. \tag{3.77}$$

Equation (3.77) can be rewritten to combine the weights and the phase into one complex term as shown below in (3.79).

$$Y = \sum_{n=1}^{N} w_n e^{-jn\theta_s} \mathrm{EEP}_n \tag{3.78}$$
$$Y = \sum_{n=1}^{N} C_n \mathrm{EEP}_n. \tag{3.79}$$

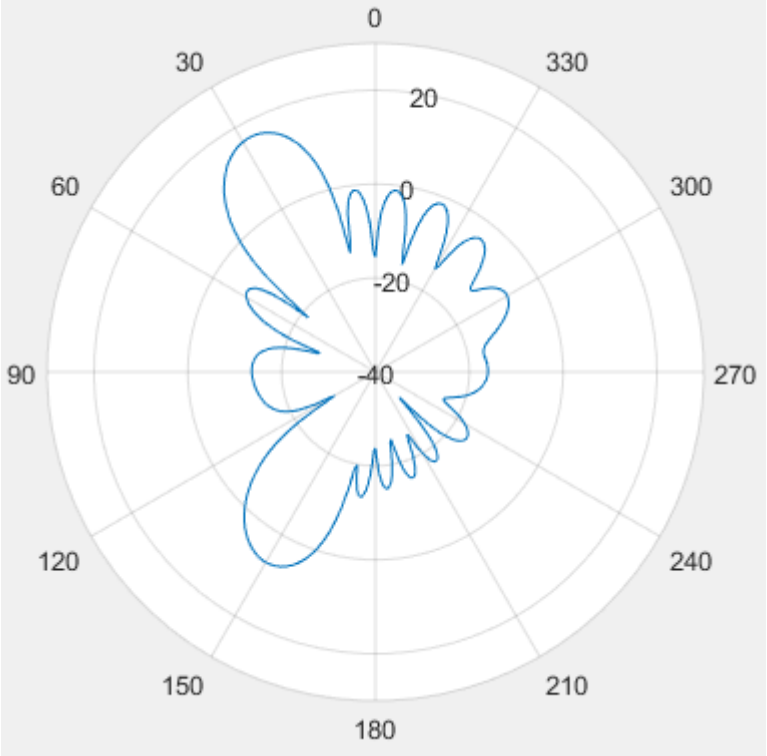

Figure 3.23: Total gain pattern from summing EEPs using Chebyshev weights and steered

For an equation of the form as shown in (3.80) below,

$$f(x,\beta) = \sum_{j=1}^{N} \beta_j \phi_j(x), \tag{3.80}$$

the least squares method determines the weights β_j to best make the sum of the product of the weights and the term ϕ_j approximate the function $f(x,\beta)$. Notice that this form is the same as in (3.79) above, where $f(x,\beta)$ would be the full goal pattern instead of the total gain pattern, Y, as the full goal pattern has to be approximated. Thus, the linear least squares method can be used to find better weights and phases to make the sum of the product of the EEPs and their weights more closely approximate the full goal pattern desired. Since the Chebyshev technique does not take the element pattern into account, the least squares weights could potentially yield better weights to make the sum of the product of the EEPs and their weights more closely approximate the desired full goal pattern shape.

The pattern for the Chebyshev weighted and steered array at $N = 16$ is shown below in Figure 3.24. The backlobe radiation at 150° can be ignored as the physical implementation will cover the back of the antenna. The sidelobes are

at -18 dB which is barely acceptable and the beamwidth is still relatively high at 7°.

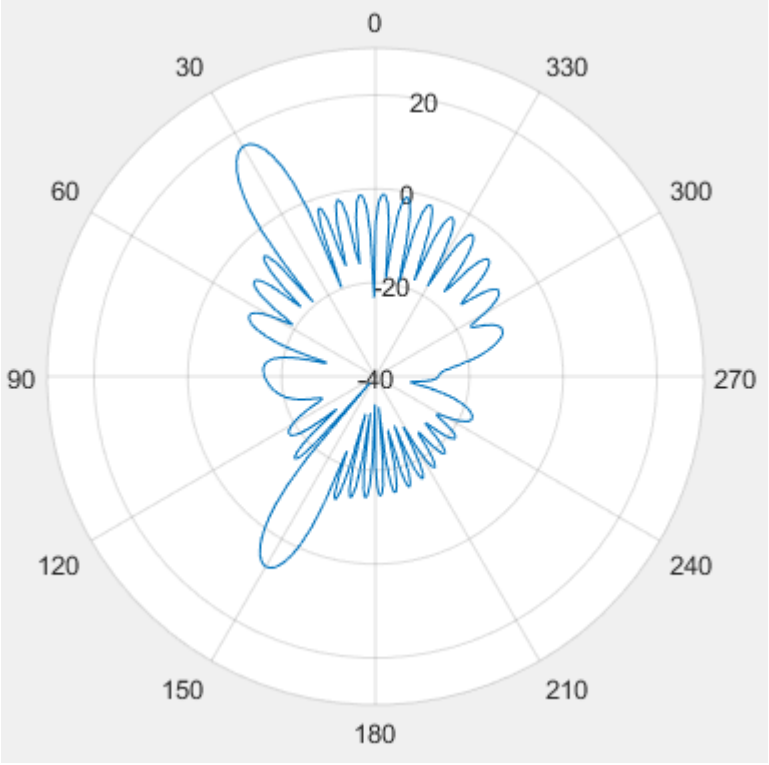

Figure 3.24: Total gain pattern from summing EEPs using Chebyshev weights and steered

The number of elements have to be squared, since if it is only linear array a fan beam will be created, however, to create a pencil beam a planar array is needed. This is shown in Figure 3.25 below.

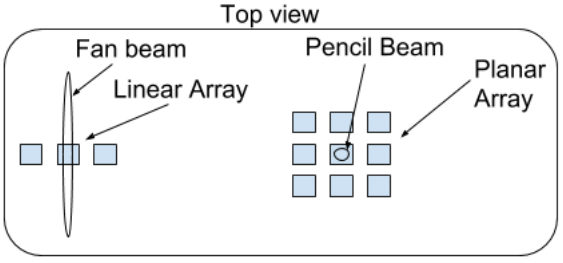

Figure 3.25: Types of beams formed by types of arrays

Even at $N = 16$ elements, it is simply not cost effective to have 16x16 elements, with 16 phase shifters. An additional problem is that phase shifters have phase drift. Making sure that 16 phase shifters are all synchronised would prove difficult to do. If the phase shifters are unsynchronised, all the waves will not positively interfere at the steered angle, which would reduce the mainlobe gain as less waves add up, and increase the sidelobes as signals might add up in unintended directions.

The cost of phase shifters is around $103,76 [13] and 16 will be needed. Additionally, the board layout for 256 elements (16x16) where the board dimensions will be 108mm x 108mm for a planar array of 16 x 16 elements, each separated a half wavelength at 22.2 GHz, with four layers for the multilayer aperture coupled patch antenna array will cost $3 709 [14]. This brings the total cost of the array system already to about ($103.76 x 16 + $3 709) x R13.60 = R73 020.58. For reference, the reflector system designed later on will cost around R25 000, which is significantly cheaper.

Unfortunately the least squares approach does not work particularly well as the sidelobes are notably higher compared to normal steering and Chebyshev weights as shown in Figure 3.26 below. The Chebyshev excitation pattern is orange, and the least squares excitations pattern is blue. This is for $N = 16$ elements. A possible reason for the weak performance of the least squares method is due to having only 16 weights to optimise the 361 data points in each EEP, respectively, so that they add up to the data points of the full goal pattern. If 300 weights could be used, a much better result would probably be obtained, but that requires 300 elements. Additionally, using weighted least squares, or optimising less data points in each EEP, is not effective as keeping the sidelobes down is just as important as having a relatively narrow beamwidth.

Microstrip patches generally have a relatively similar main beam pattern meaning that no significant beamwidth increase can be done for the element by choosing different patches. An element beamwidth increase would lead to less elements necessary to make the array design have a relatively narrow beamwidth, when steered. Patches have relatively high beamwidth and are useful because the components can be etched onto the design reducing cost, which is not the case for using dipoles.

Even though this analysis showed it is not particularly viable a physical design was done, using an improved patch design, a multilayered aperture coupled patch antenna. By doing this, the validity of the analysis can be tested as well as the assumption that a different patch design would not have a significant impact on the amount of antennas required to have an acceptable array design. Furthermore, it is also necessary to design the feed network and see how a real

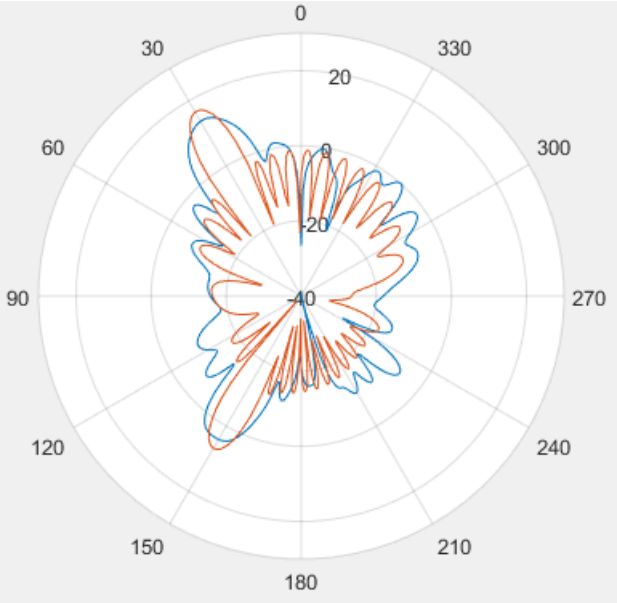

Figure 3.26: Chebyshev excitations vs Least Squares excitations for antenna elements

design would perform.

3.7 Array and feed network designs in FEKO

A multilayered aperture coupled patch antenna is a patch antenna that consists of multiple layers of interchanging materials. Additionally the antenna has an aperture or slot (opening) where the electromagnetic energy couples through to the patches from the transmission line or feed line. In Figure 3.27 a design of one is shown, and for this thesis this design was implemented. The FEKO design of this patch is shown in Figure 3.28.

In Figure 3.28, the patch design consists of a upper patch which is modelled as a PEC (Perfect Electric Conductor) material. Underneath it is a dielectric material (Upper substrate) with dielectric constant $\epsilon_r = 3.55$. Underneath that dielectric material is another patch (Lower patch) modelled as a PEC. It does not have the same dimensions as the upper patch. Underneath that patch is another dielectric region (Lower substrate) with the same properties as the first. A ground plane then exists under the lower substrate, with a section cut out of the ground plane. This section is known as the aperture. Finally, there is a third dielectric region (Feed substrate) underneath the ground plane with a feed line below it (transmission line). Figure 3.29 shows the regions from the side in the FEKO design.

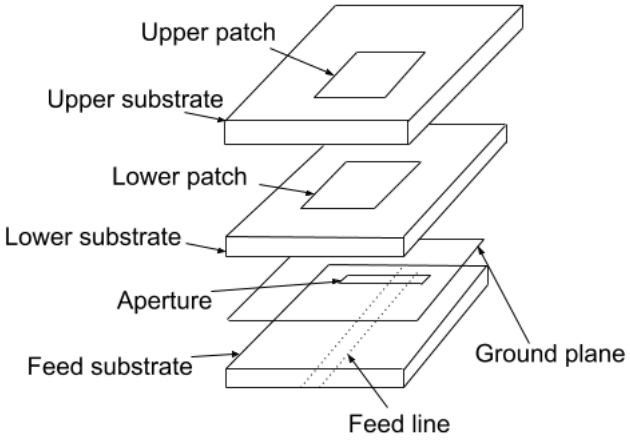

Figure 3.27: A Multilayered aperture coupled patch antenna design

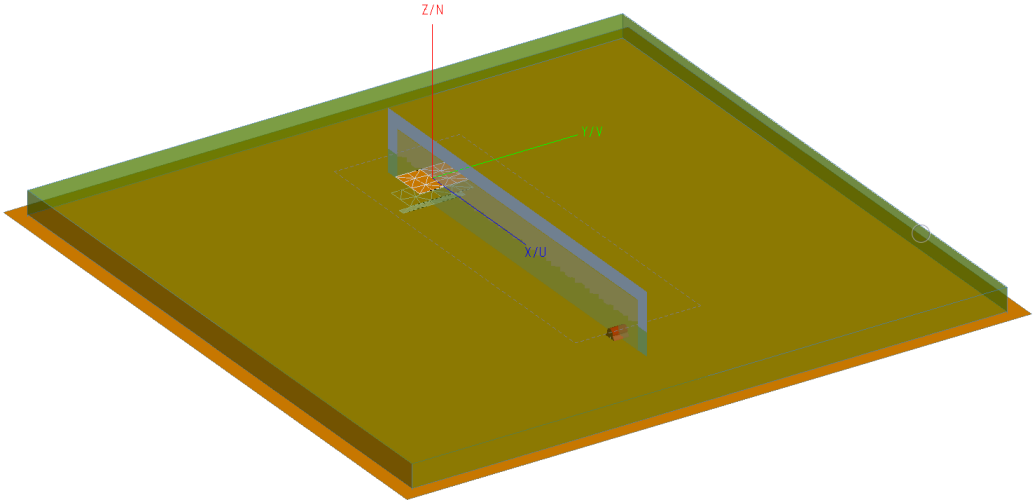

Figure 3.28: A Multilayered aperture coupled patch antenna design in FEKO

Figures 3.30 and 3.31 show the top view above the ground plane and the bottom view underneath the ground plane of the FEKO design, respectively.

The multilayer aperture coupled patch antenna has the advantage of having a relatively high fractional bandwidth compared to the standard patch antennas. If the antenna operates efficiently over the region from f_h to f_l, where f_h is the highest frequency and f_l is the lowest frequency where the antenna performance is deemed efficient, then the fractional bandwidth is defined as:

$$FBW = \frac{f_h - f_l}{f_c}, \tag{3.81}$$

where f_c is the centre frequency of operation, which is 22.2 GHz for this thesis.

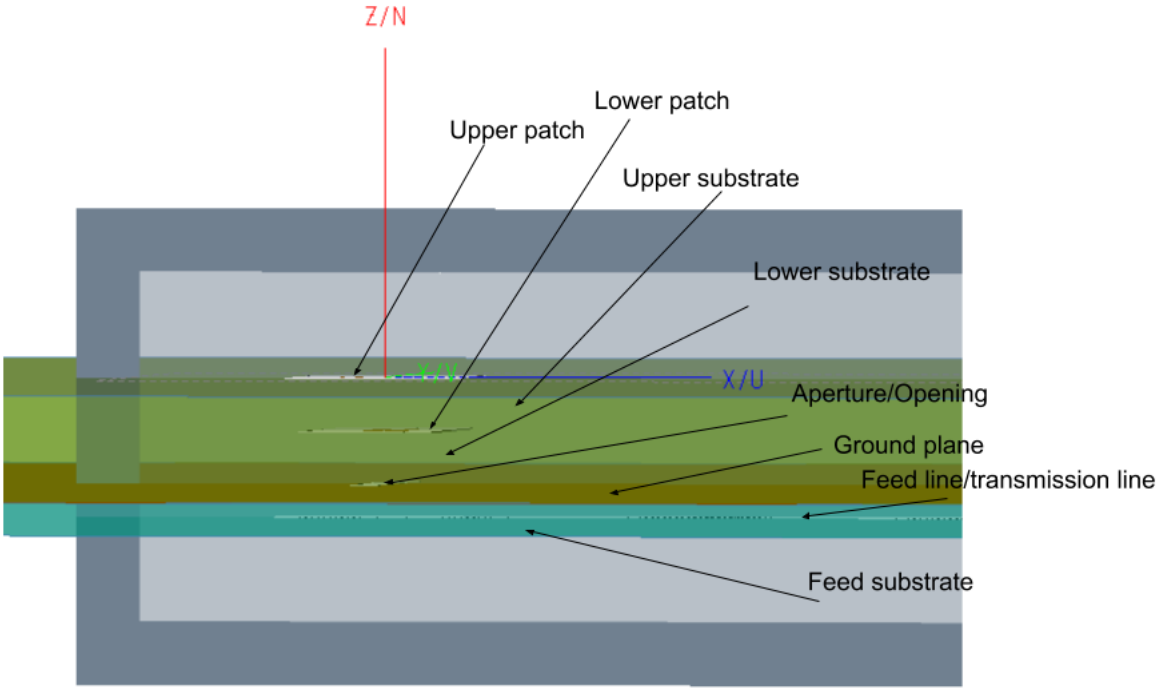

Figure 3.29: Patch design in FEKO dissected (side view)

The requirement for efficient performance here is where the reflection coefficient (at the input port where the energy is inserted, and will always refer to that in this thesis) is $S_{11} < -10dB$. The reflection coefficient S_{11} quantifies how much energy being inserted is reflected and by reducing the amount of energy reflected the amount of energy radiated is increased. Due to the reciprocal theorem this also applies to how much of the energy received is reflected. If the amount of energy being reflected is relatively low over a certain frequency range, then the antenna's gain or performance does not deteriorate noticeably over that range, as most of the energy is not reflected but instead received. Having an efficient antenna over a relatively high frequency band means it has a relatively high fractional bandwidth, which once again, is important to have at high frequency design.

It is difficult to manufacture a high frequency design exactly as precise as needed. The small differences in geometry can shift the centre frequency f_c of

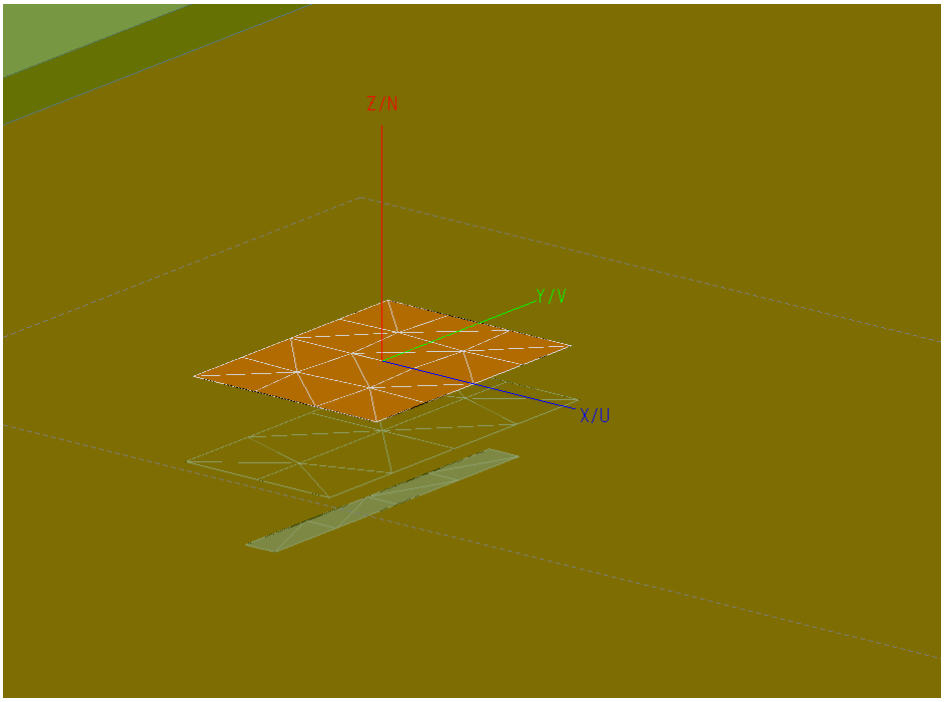

Figure 3.30: Top (above ground plane) view of patch design in FEKO

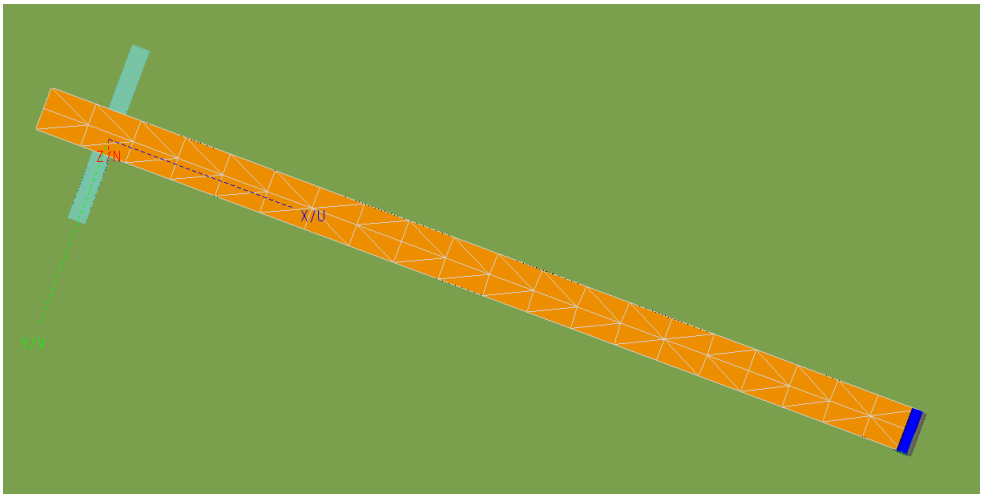

Figure 3.31: Bottom (below ground plane) view of patch design in FEKO

the antenna's operation. If the antenna does not have a high enough bandwidth, the shift can cause the centre frequency f_c to fall outside of the antennas operating frequency, $f_c < f_l$ or $f_c > f_h$. At that point the antenna does not operate in its efficient region any more and consequently does not operate as designed. Having a relatively high bandwidth at high frequency is thus important.

The Stellenbosch University's tolerance on PCB manufacturing is 0.02 mm and the tolerance of manufacturing of lines and terminations are 0.1 mm. Trax, a commercial company, can, however, do manufacturing at micrometers [15]. The design will first be manufactured at the university and thus requires a relatively high tolerance design.

The radiation pattern produced by the multilayer aperture coupled patch antenna design is relatively insensitive to changes to the dimensions of the patches in the antenna. In Figures 3.33, 3.34, 3.35 and 3.36 this is shown where the top patch receives a relatively large change. The upper patch width increases from 3.46 mm to 6 mm and its length increases from 2.6 mm to 4 mm. The width and length is defined as shown in Figure 3.32. Despite these changes, the patterns look relatively similar. The orange and blue plots are for the two different designs and they are overlapped on the same graphs for comparison.

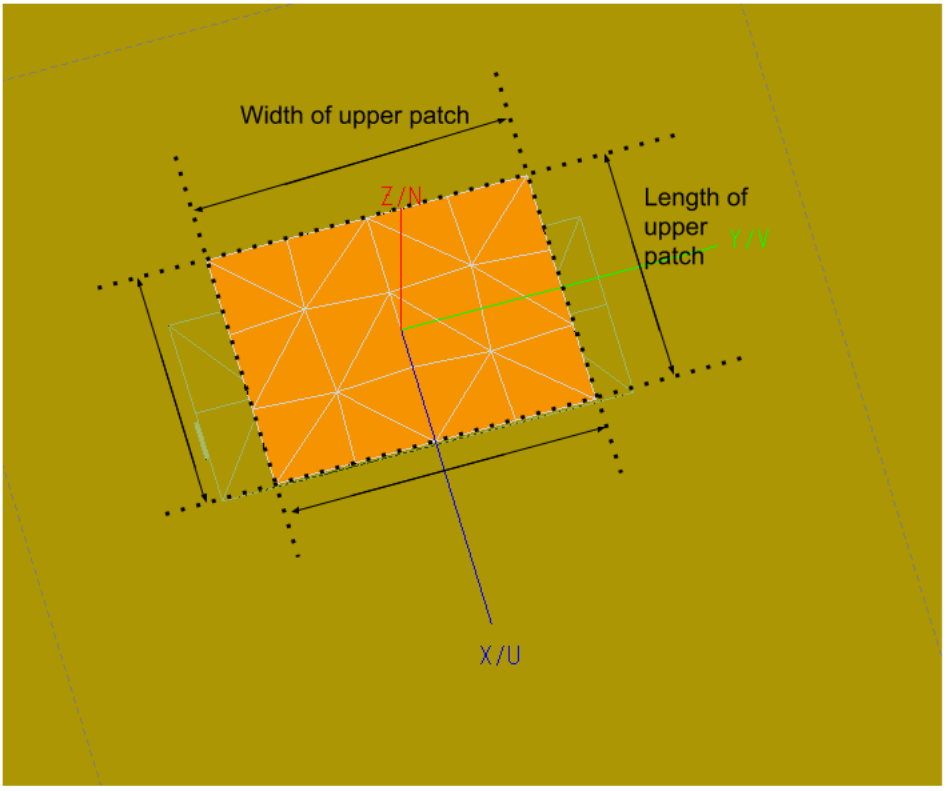

Figure 3.32: Width and length description of patch

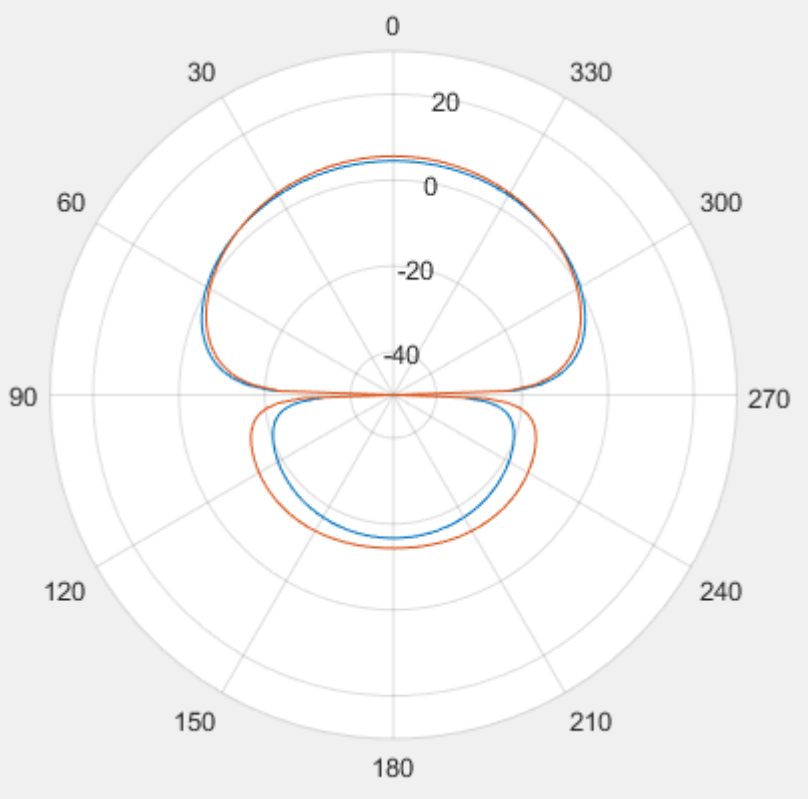

Figure 3.33: Compared radiation pattern of two different patch designs. Phi = 90

The FEKO design of the multilayer aperture coupled patch antenna was optimised. Since the radiation pattern is relatively insensitive, the parameter that was optimised was the reflection coefficient S_{11} over a frequency range to increase the bandwidth of the antenna design with its feed network.

Finding an optimum design for the patch was done by using optimisation tools available in FEKO. The goal for the optimisation was to have S_{11} below -15 dB over a 20 percent fractional bandwidth, from $f_l = 19.98$ GHz to $f_h = 24.42$ GHz, where $f_c = 22.2$ GHz.

Many variables were allowed to vary to find a good optimised design. This did increase the optimisation time notably, however, a relatively good result was obtained. The variables that were allowed to vary are shown in Table 3.1.

After the optimisation was done, the following results were obtained as shown in Figure 3.37.

From Figure 3.37 it can be noticed that the reflection coefficient S_{11} is below -10 dB over the entire frequency range from 19.98 GHz to 24.42 GHz. It is true

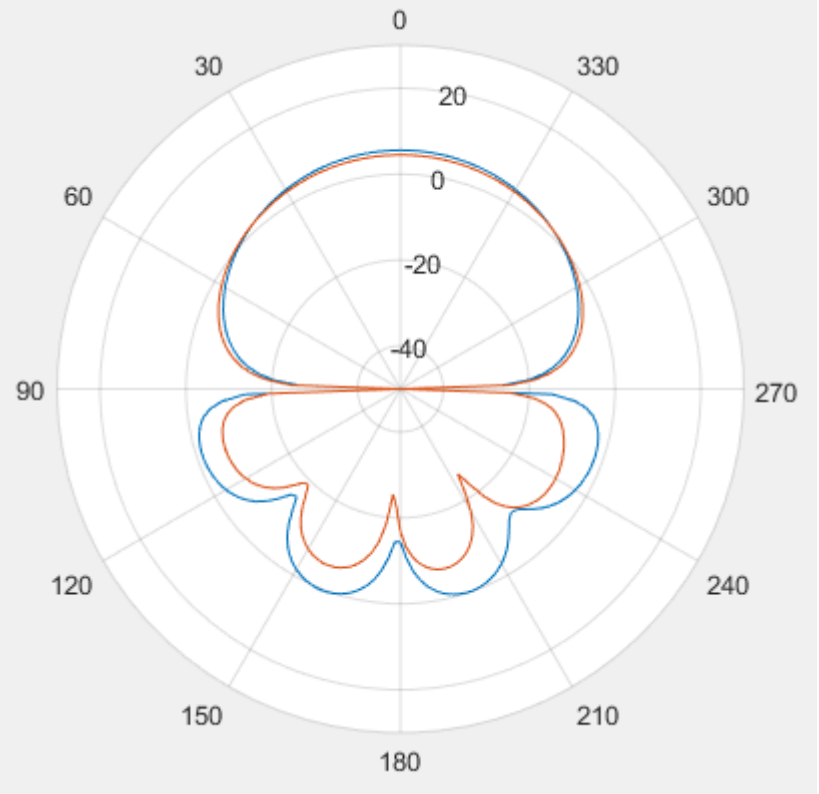

Figure 3.34: Compared radiation pattern of two different patch designs. Phi = 0

that the goal was set to -15 dB, however, -10 dB is a sufficiently low amount of energy being reflected over the region to ensure effective functioning of the antenna over the range. With the parameters of a single aperture coupled multilayered patch antenna optimised, an array design needs to be considered. Since an array will necessarily have coupling between the elements, an optimisation like this will have to be done again for the array configuration.

Before the physical array design is discussed, a choice had to be made in terms of which feed network will be used. A serial feed network is shown in Figure 3.38. A corporate feed network is shown in Figure 3.39. The series feed network has less losses than the corporate feed network, due to there being less transmission lines so it is more compact. The series feed network, however, has different line lengths to each antenna element, meaning the waves arrive at different times and has inherent phase differences, so it steers by itself. The corporate feed network is more inefficient in terms of line losses since there are more transmission lines. All the waves, however, arrive at the elements at the same time thus the length of transmission line to each antenna element is exactly the same. This means it has no inherent steering and the steering can be controlled by phase shifters. Due to this, the corporate feed network is chosen.

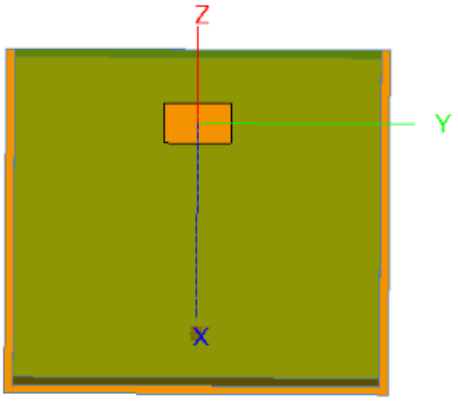

Figure 3.35: Patch (after size increase) radiation pattern shown in Figures 3.33 and 3.34

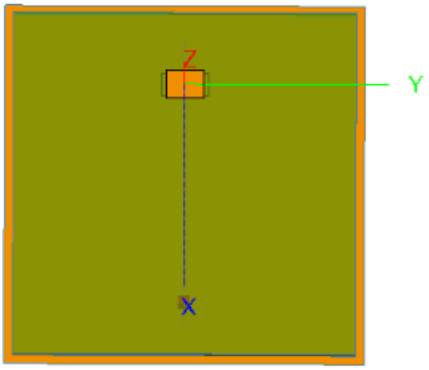

Figure 3.36: Patch (before size increase) radiation pattern shown in Figures 3.33 and 3.34

The Figure 3.38 shows the principal feed network design, however, the feed network is more complex if it is to be efficiently used. Figure 3.40 shows a better design. The improved design is discussed in detail next.

A quarter wave transformer is shown in Figure 3.42. A quarter wave transformer is used to match the combining line segments so that reflections do not occur at these junctions as shown in Figure 3.41, which would noticeably reduce the network's efficiency. Two 100 Ω line impedances, connecting to the 50 Ω transmission line, would have a resulting impedance of 50 Ω. This impedance match removes the reflections at this junction. Thus the quater wave transformer matches 100 Ω to 50 Ω, as 50 Ω transmission lines are used. The transformer impedance is $Z_0 = 70.71\ \Omega$, according to (3.82) where Z_L and Z_{in} are the load and source impedances, respectively.

Table 3.1: Parameters optimised for single patch design

Variables
Length of the aperture
Width of the aperture
Width of the upper patch
Length of the upper patch
Width of the lower patch
Length of the lower patch
Height of the upper substrate
Height of the lower substrate
Length of the transmission/feed line
Width of the transmission/feed line
Feed line length past the aperture

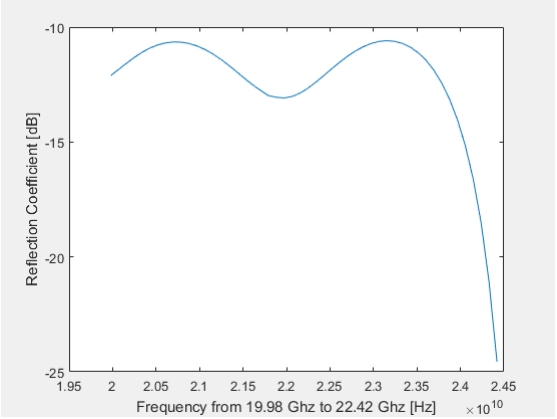

Figure 3.37: S_{11} result of optimised design over frequency range

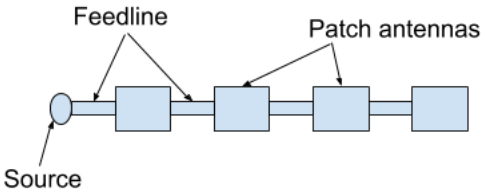

Figure 3.38: Series feed network for linear array

$$\begin{aligned} Z_0 &= \sqrt{Z_L Z_{in}} \\ Z_0 &= \sqrt{(100)(50)} \\ Z_0 &= 70.71\ \Omega. \end{aligned} \tag{3.82}$$

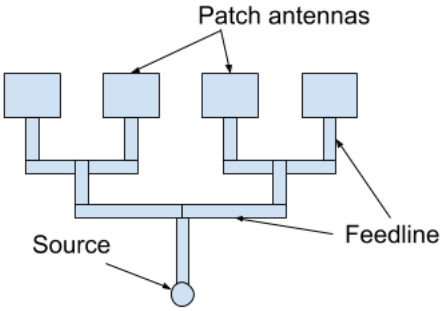

Figure 3.39: Corporate feed network for linear array

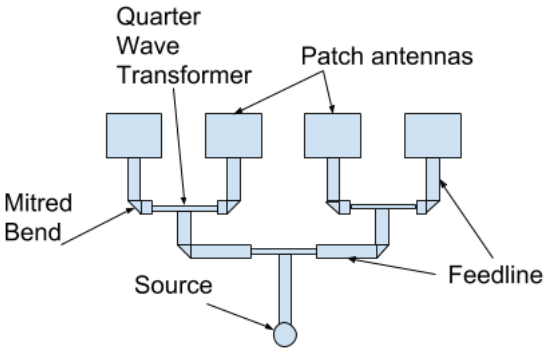

Figure 3.40: Practical corporate feed network for linear array

The next added mechanism is the Mitred Bends. When dealing with a 90° bend, as can be seen in Figure 3.39, two problems are encountered. The first is that the bend causes a discontinuity which changes the characteristic impedance of the line adding shunt capacitance. The second problem is that the bend causes the transmission lines effective length to be shorter than the centreline lengths because the electromagnetic waves have a shorter path to the next line segment than going through the centre of the current line. This can change the time it takes the waves to reach the elements and cause phase problems. Mitred bends attempts to mitigate these issues.
Their design is done according to a paper by R.J.P Douville and D.S. James [16]. The equations follows for the dimensions as given by Figure 3.43. The relative permittivity of the substrate is ϵ_r.

$$D = W\sqrt{2} \tag{3.83}$$

$$X = D(0.52 + 0.65e^{-1.35(\frac{W}{H})}) \tag{3.84}$$

$$A = (X - \tfrac{D}{2})\sqrt{2}. \tag{3.85}$$

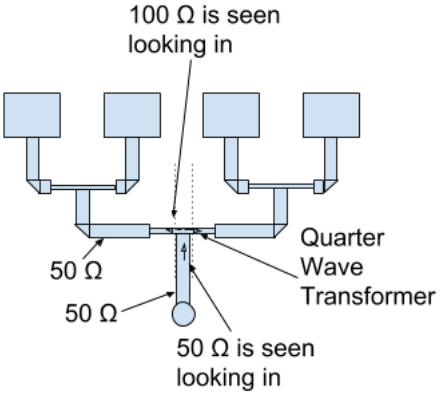

Figure 3.41: Quarter wave transformer matching combining line segments

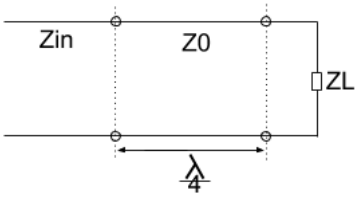

Figure 3.42: Quarter wave transformer

These equations are only valid as long as:

$$0.25 \leq \frac{W}{H} \leq 2.75 \tag{3.86}$$

$$2.5 \leq \epsilon_r \leq 25. \tag{3.87}$$

Doing this corporate feed network design on linear or planar array designs follow the same principles, however the network does look slightly different. Figure 3.44 shows a corporate feed network design for a planar array design.

These designs were implemented in a multilayered aperture coupled patch antenna array design in FEKO for both linear and planar versions. Instead of directly linking the feed lines to the patch antennas, it was coupled through the aperture in much the same way as it was done in the single multilayered aperture coupled patch antenna design.

The linear array design is shown from below and above in Figures 3.45 and 3.46, respectively.

Using the same design values as was found in the optimisation for the single multilayered aperture coupled patch antenna, this design was also optimised using the same goal of -15 dB reflection coefficient over a fractional bandwidth

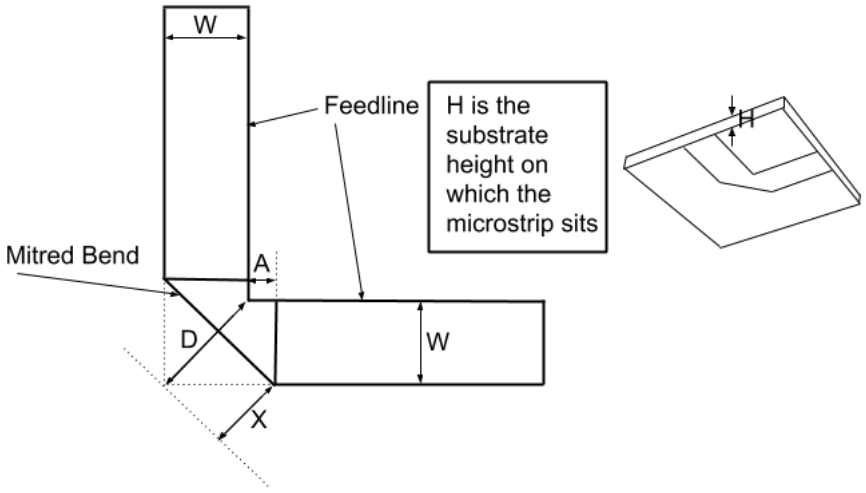

Figure 3.43: Mitred bend design

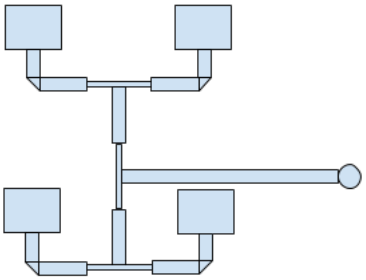

Figure 3.44: Practical corporate feed network for planar array

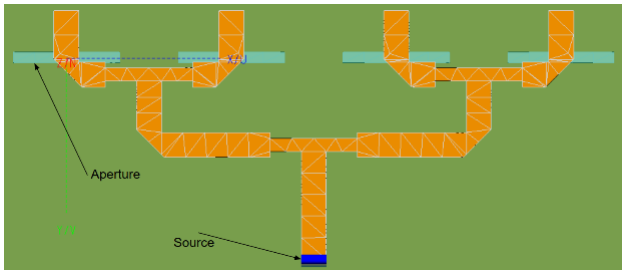

Figure 3.45: Practical corporate feed network for linear array in FEKO (from below ground plane)

of 20 percent from 19.98 GHz to 24.42 GHz from the centre frequency of 22.2 GHz. The parameters that were optimised are shown in Table 3.2.

In Figure 3.47 the result from the optimisation is shown. Over the bandwidth region of interest, the reflection coefficient remains below -10 dB which is similar to the case for the single patch antenna.

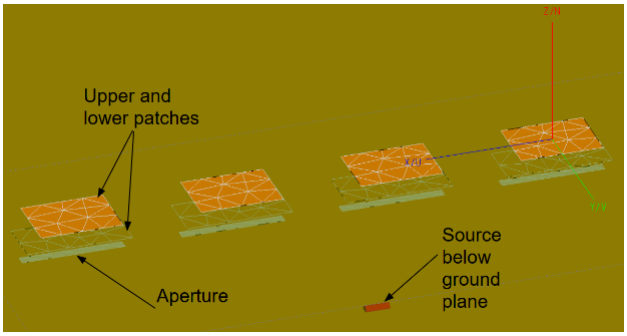

Figure 3.46: Top (above ground plane) view of linear array design

Table 3.2: Parameters optimised for array design

Variables
Line width of transmission lines (Determines characteristic impedance of lines)
Feed line length
Length of transmission line past the aperture

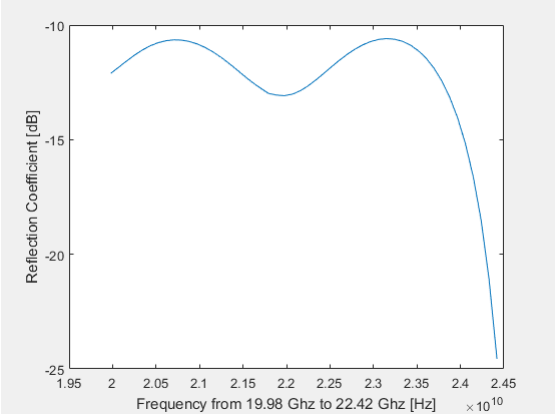

Figure 3.47: S_{11} result of optimised linear array design

For the case of the planar array, Figures 3.48 and 3.49 show the bottom and top views, respectively. The result after the optimisation is shown in Figure 3.50. The reflection coefficient is even better than it was in the previous two cases, maintaining an S_{11} of almost -15 dB over nearly the entire frequency range of interest.

With these results the feed network works well. Now the array radiation pattern for both cases has to be considered. The linear array will give an indication as to how many elements will be required for an adequately narrow mainlobe beam to reach the specification. The planar array will give an indication to

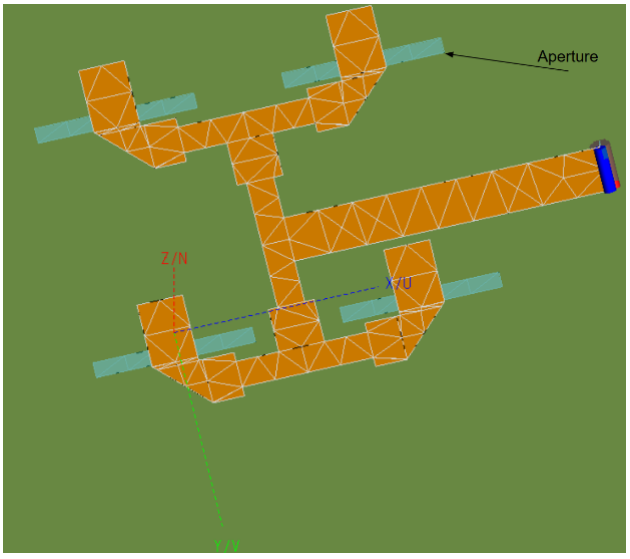

Figure 3.48: Practical corporate feed network for planar array in FEKO (from below ground plane)

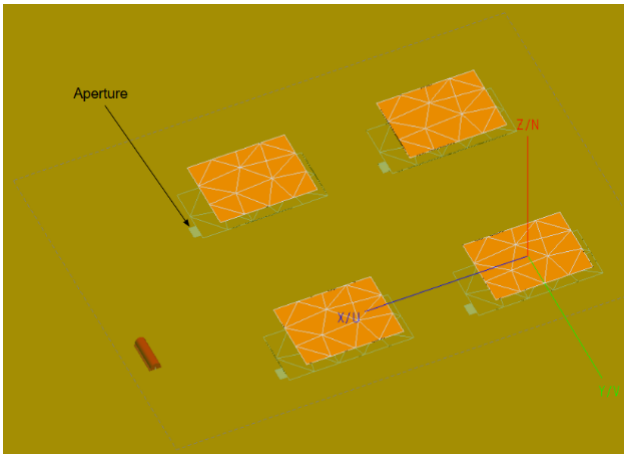

Figure 3.49: Top (above ground plane) view of planar array design

how well this beam can be transformed into a pencil beam.

Figure 3.51 shows the mainlobe of the linear array. At 24° for a -3 dB beamwidth, it is far from reaching specification. This agrees with the analysis that was done earlier, indicating that many more elements would be required to reduce the mainlobe to a reasonable level to reach the specifications.

In Figures 3.53 and 3.54 the far field results for the planar array are shown. Two cuts are taken in both axis, respectively. Since the beamwidths are relatively similar this is a good indication of how well the pencil beam would

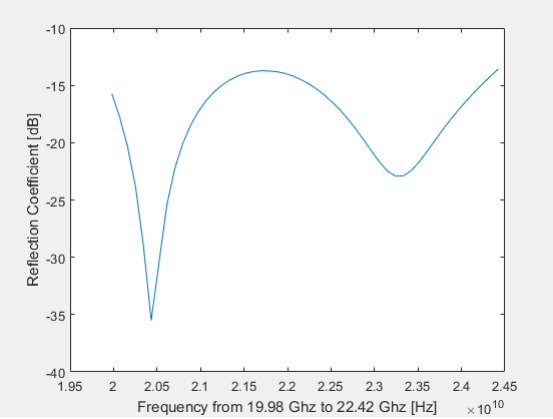

Figure 3.50: S_{11} result of optimised planar array design

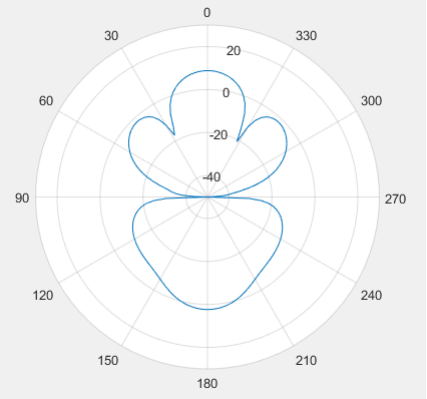

Figure 3.51: Linear array radiation pattern

be formed. By increasing the number of elements in both axes (keeping the number the same in both axes) of the planar array, the pencil beam width can be reduced.

After this entire FEKO implementation and simulation with it correlating well to the analysis done before, the design of an array for the solution to the antenna design for a low cost water vapour radiometer is not practical. This is because even for $N = 16$ elements, the feed network for 16x16 elements would be difficult to make and keeping the 16 phase shifters in sync would also prove difficult. A different approach needs to be taken.

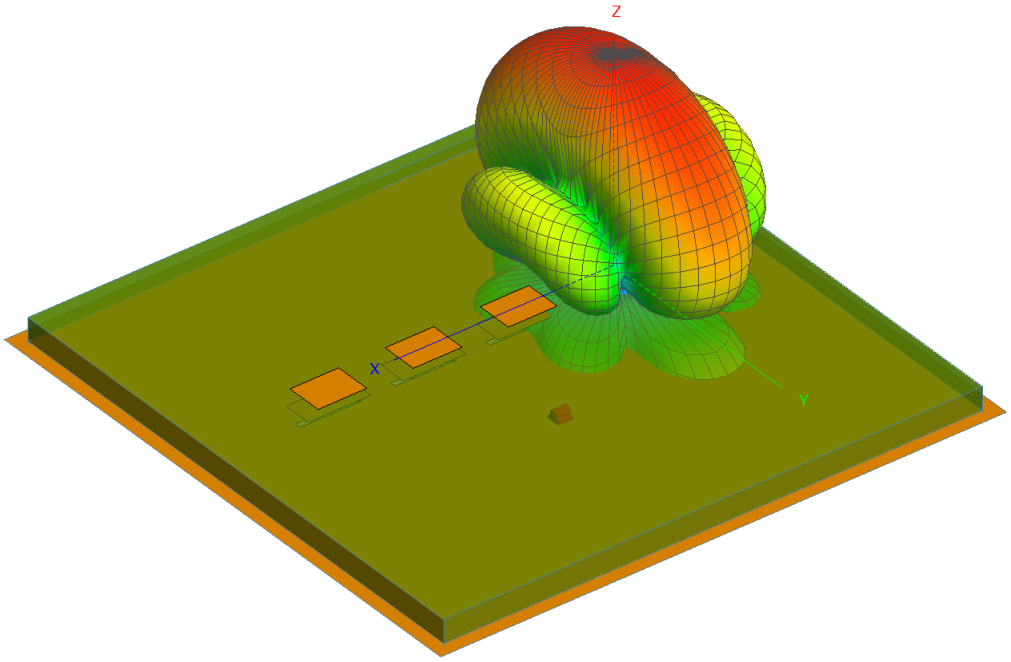

Figure 3.52: Radiation pattern on linear array design

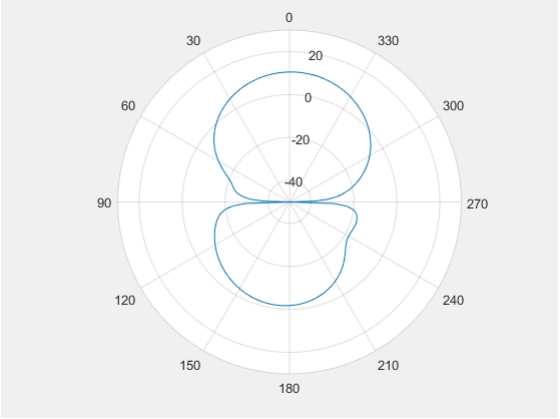

Figure 3.53: Planar array radiation pattern in y-axis

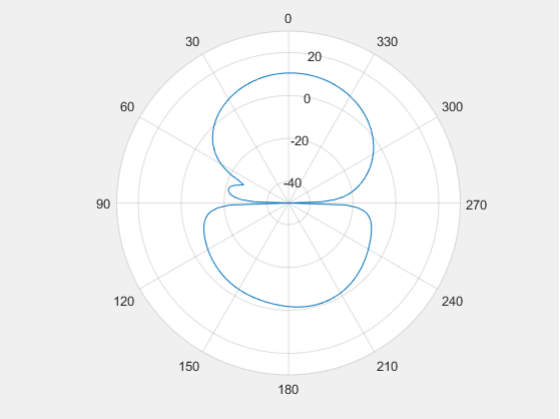

Figure 3.54: Planar array radiation pattern in x-axis

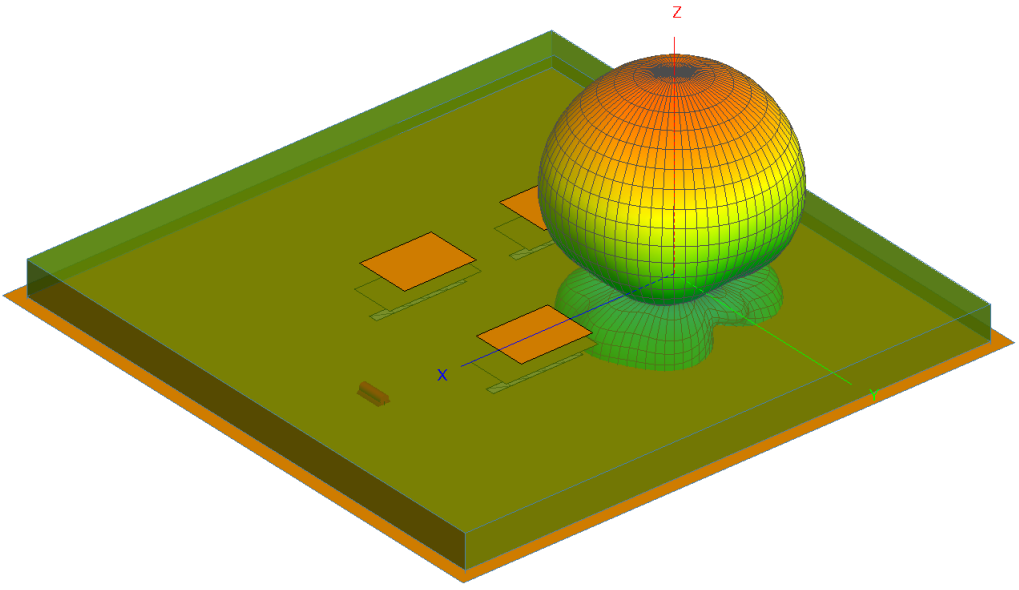

Figure 3.55: Radiation patterns on planar array design

Chapter 4

Antenna for Water Vapour Radiometry

4.1 Reflector Basics

Reflectors in antennas refer to a surface that reflects electromagnetic radiation or waves. What makes them particularly useful is how high their gain can be, making them effective for increasing the gain of a system. Reflectors are made out of a metal so that it has high conductivity and can easily reflect the radiation. Its physical form varies, but a popular reflector design is the parabolic reflector found on radio telescopes as seen in Figure 4.1 below. They are also used in other applications.

Figure 4.1: Example of parabolic reflector in the real world [3]

Many types of reflectors exist. A spherical reflector focus the incoming energy to a specific line in space, where a parabolic reflector focus the incoming energy to a specific point. A parabolic reflector is chosen for the design as the ability to focus the energy to a focus point is particularly useful for a horn type feed that has a phase centre. The phase centre is the location in the horn from which the energy has to be radiated to radiate a spherical wave front. The phase is the same everywhere on the wave front.

In parabolic reflectors there are also different types. Figure 4.2 below shows some examples. Notice from Figure 4.2 that a parabolic reflector has a feed antenna. In the receiving context, the main purpose of the reflector is to concentrate the electromagnetic radiation or waves to this feed antenna to increase gain. For a parabolic reflector, by making some assumptions like the feed pattern being circularly symmetric, linearly polarised and neglecting cross-polarisation contributions, its directivity (as seen in [10]) is given by (4.1),

$$D_0 = (\tfrac{\pi d}{\lambda})^2 \epsilon_{ap}. \tag{4.1}$$

The variable ϵ_{ap} is the aperture efficiency, and d is the aperture diameter of the reflector. By increasing the aperture diameter of the reflector, its gain or directivity can be increased. Thus the larger the reflector, the more the gain of the antenna system can be increased. Similarly, the larger the array was in Chapter 2, the smaller the beamwidth was. When the perceived aperture forming the beam reduced while steering, the beamwidth increased.

Aperture efficiency is generally the product of 6 factors [10], and is shown in (4.2),

$$\epsilon_{ap} = \epsilon_s \epsilon_t \epsilon_p \epsilon_x \epsilon_b \epsilon_r, \tag{4.2}$$

where ϵ_s is the spill over efficiency that describes how much of the total power radiated by the feed is intercepted and reflected by the reflector. The taper efficiency, ϵ_t, is how uniform the amplitude distribution of the feed radiation pattern is over the reflector surface. Phase efficiency, ϵ_p, is the phase uniformity of the field over the aperture plane. Polarisation efficiency, ϵ_x, is the polarisation uniformity of the field over the aperture plane. Aperture blockage, ϵ_b, which will be discussed later. Finally, the random error efficiency, ϵ_r, is random errors over the reflector surface.

One of the reasons these reflectors are fed by a horn antenna is due to the fact that horn antennas are highly directive antennas too, so they are sensitive to radiation from the direction of the reflector. This means the system has even higher gain in a specific direction than if an omni directional antenna, like a half-wave dipole, would have been used instead. Higher gain horns does

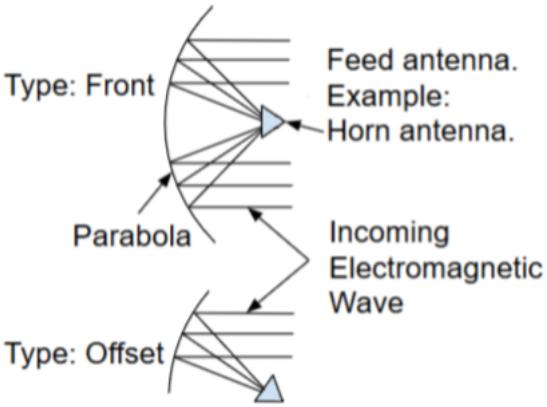

Figure 4.2: Types of parabolic reflectors

not necessarily lead to higher gain reflector systems. If the reflector surface is uniformly illuminated by the horn, the reflector will have a higher gain than if the horn illuminated mainly the centre of the reflector, tapering to the edges of the reflector. This is because the far field formed from the Fourier transform of the aperture field is more directive if the aperture is uniformly illuminated, compared to if it was primarily illuminated in the centre. Illuminating primarily the centre of the reflector, with tapering to the edges of the reflector, leads to a lower sidelobe level compared to uniform illumination. If a Gaussian pattern were to be used for the feed horn radiation pattern, the far field of the aperture of the reflector would be the Fourier transform of a Gaussian, which is another Gaussian. The beamwidth thus increases, however, the sidelobes are lower.

Additionally between all the different types of designs, since a system with a high gain is highly valued in this case, the aperture blockage has to be kept to a minimum. Aperture blockage is how much of the area in front of the reflector is obstructed which prevents it from reflecting radiation. For example if the entire aperture, or front, of the reflector is blocked it will result in a massive aperture efficiency decline of the reflector, where the reflector will reflect almost no radiation. Keeping aperture blockage to a minimum thus increases the aperture efficiency of the reflector which increases the gain of the system. Figure 4.3 explains this graphically.

For this design, two feeds and two reflectors will be required and will have the form as shown in Figure 4.4. This will be discussed later. It is important to have a unique feed for each reflector as each feed horn's phase centre has to be on the focus point (where the energy is directed to) of each reflector, otherwise scan loss occurs which reduces the system's gain. Aperture blockage can be caused by other antennas being physically in the way of each others

radiating directions, which could also decrease system effectiveness by increasing sidelobes. The offset reflector which has the feed antenna at its side causes very little aperture blockage and thus is chosen for the design.

Additionally, the mechanical mounts to keep the feeds in place might also cause aperture blockage which is another incentive to keep the feeds away from the aperture of the reflector. By using an offset design it becomes possible to keep the feeds relatively close to each other which makes it possible to use a single mechanical structure and only separate the mechanical design where the two feeds need to be connected to it. This saves material which reduces cost which is in line with the goal of a low cost system. Figure 4.4 shows a proposed design to further motivate this argument.

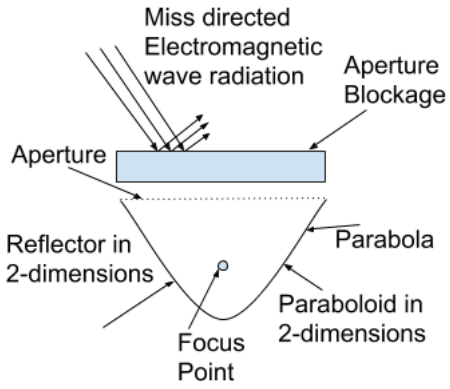

Figure 4.3: Reflector suffering from aperture blockage

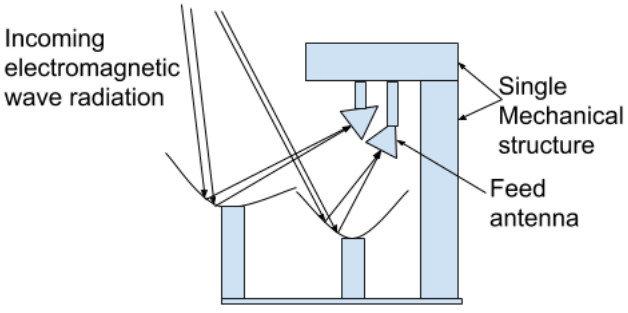

Figure 4.4: Feeds close to each other reduces the amount of material needed to anchor both feeds which reduces cost

4.2 Reflector Design

A parabolic reflector has a shape that follows the analytical function of a paraboloid in 3-dimensions. A paraboloid is the 3-dimension extension of the parabola shape in 2-dimensions. It is possible to create a paraboloid from a parabola, by rotating the parabola around its central axis for a full revolution. This is made explicitly clear in Figure 4.5.

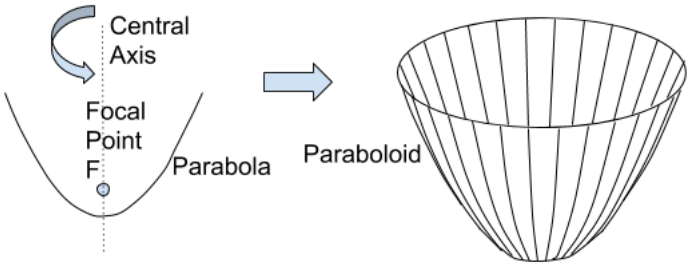

Figure 4.5: Paraboloid formed from rotation of parabola around central axis

To design the reflector antenna for the low cost water vapour radiometer, a parabolic reflector and a horn feed needs to both be designed. The reflector is designed first. The reason for this is that the horn feed radiation pattern, or gain pattern, can be approximated as a Gaussian pattern. The Gaussian pattern has a certain taper, specified to have a certain reduction in gain at a specific angle from the mainlobe. In other words, the Gaussian beam is defined to have the highest gain at its center, reducing outwards. Figure 4.6 describes this, the horn is not offset from the reflector in this figure to better and more clearly explain what is meant by the Gaussian pattern and tapering.

Since the horn radiation can initially be approximated as a Gaussian pattern, the reflector can be designed first without a horn design. A horn design is then done after, relating to the Gaussian pattern that was used for the reflector design. If the reflector is offset, the angle at which the horn antenna would illuminate the reflector surface can be considered. The taper of the Gaussian pattern can be used to determine how wide the beam is. This information can be used to determine which part, out of the larger parabola, the offset parabolic reflector would have to be cut out off. This is made clear in Figure 4.7 below.

The entire discussion surrounding forming an offset reflector surface from a conic section was done with reference to the article [17].

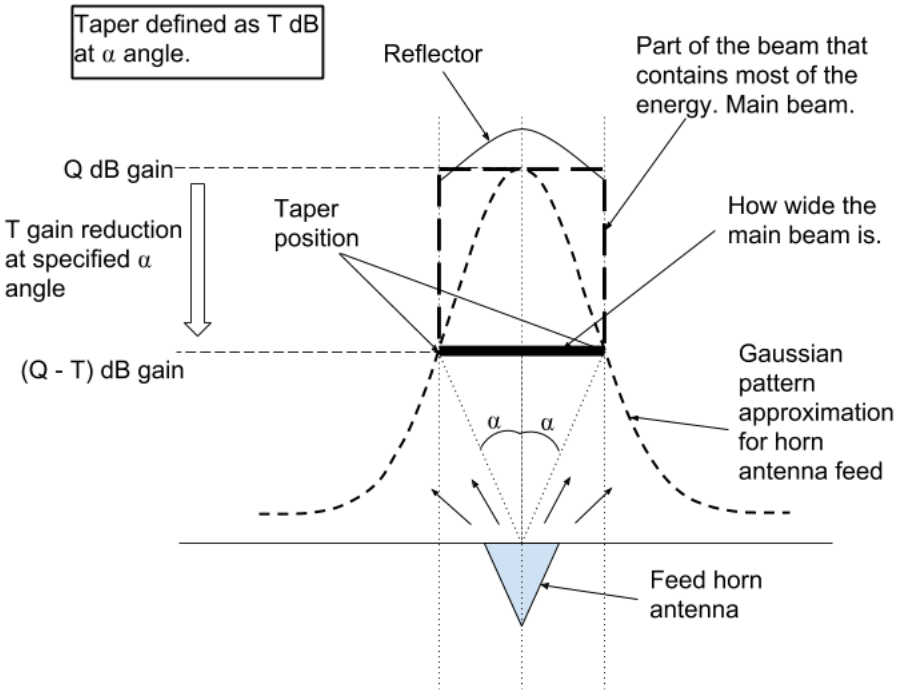

Figure 4.6: Gaussian approximation pattern with taper specified

In Figure 4.7, the horn antenna would be located at the origin of the co-ordinate system, it would be directed towards the parabola at an angle of β, and its beam pattern would be defined in such a manner that most of the radiation power would be contained within the angle α from the central angle β. The reflector surface would then be cut out of the parabola from M_1 to M_2 and the resulting reflector surface shape cut (projected to the $x-y$ plane) is seen on the right hand side of Figure 4.7.

Naturally, this Figure 4.7 and this explanation surrounding it is of concern for a 2-dimensional situation, however, by simply extending the arguments into 3-dimensions by rotating the parabola about the z-axis to form a 3-dimensional curve and using a circular 3-dimensional cone with its central axis in the $y-z$ plane so that it is symmetric around the $y-z$ plane, would result in a 3-dimensional reflector surface being cut out if the same procedure is followed.

Reflectors are usually steered using some form of mechanical steering, including motors and physically moving arms manoeuvring the reflector around for an optimal position. This is not viable for the low cost system that needs to be designed, as mechanical components that move, such as motors, have a tendency to break down and require maintenance to keep the system functioning.

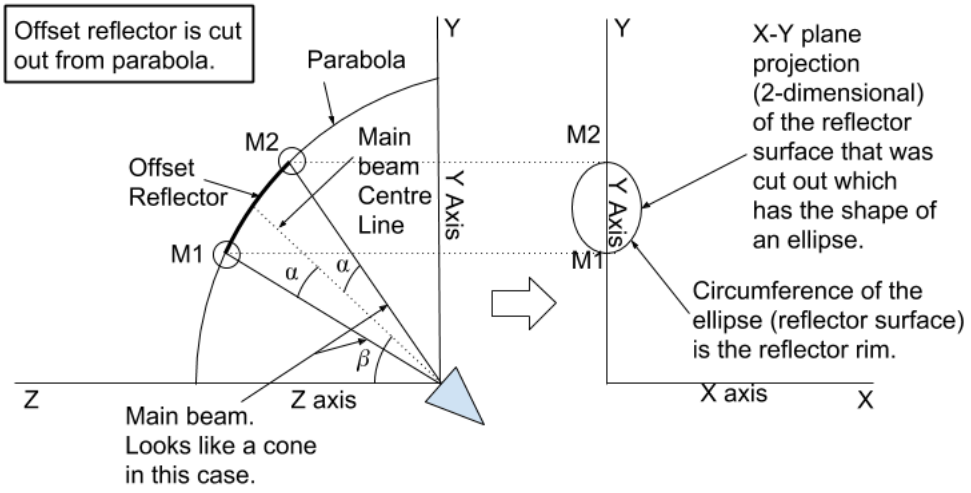

Figure 4.7: Offset parabolic reflector formed from cone intersection with parabola

This increased maintenance, increases the cost of the system. The solution to this problem is to remove the need for any form of steering, by designing the reflector system to observe in a few distinct directions. This still meets the requirement that would have been met by steering, however, no steering is needed. This is what makes the reflector design viable.

Since the reflector system would have to be designed to have the antenna system observe in a few distinct directions, a method of doing this would be to have an n amount of reflectors and an n amount of feeds for the n amount of directions to observe in. Each feed primarily illuminates a single reflector surface. Each of these reflectors with their respective feeds would be designed to observe in a single direction, leading to n amount of distinct directions the combined system could observe in.

Furthermore, if the directions to observe in is symmetric around the central axis of the combined reflector system, the system can also be symmetric around its central axis, both mechanically and electrically. This leads to the conclusion that only half of the entire system has to be created for a demonstrator project. Thus the entire design will consist of two feeds and two reflectors (for $\theta_o = 10°$, $\theta_o = 30°$) since the system has to observe in four directions total (θ_o = -30°, θ_o = -10°, $\theta_o = 10°$, $\theta_o = 30°$), and the other side (θ_o = -30°, θ_o = -10°) can be duplicated leading to no additional design required. Figure 4.8 shows exactly what is being meant here.

Since the earlier argument regarding the intuitive expansion of the 2D design to 3D, and the symmetrical nature of the design, the 2-dimensional (planar) design of the system is adequate in many cases. This is why the radiation

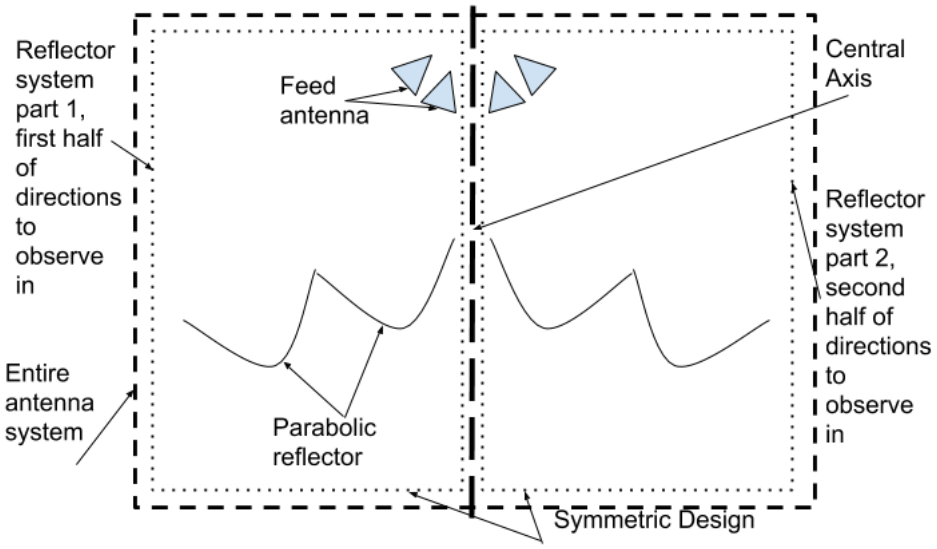

Figure 4.8: Types of conic sections

patterns are considered mainly in a 2-dimensional scope where θ is changed but ϕ is kept constant. This results in a 2-dimensional (projected) radiation pattern dependant on θ, since the pattern is symmetric around the plane being projected to. The reflectors and horns are also positioned on this plane and thus the design can be done in 2-dimensions. Figure 4.9 shows how the symmetric design being done.

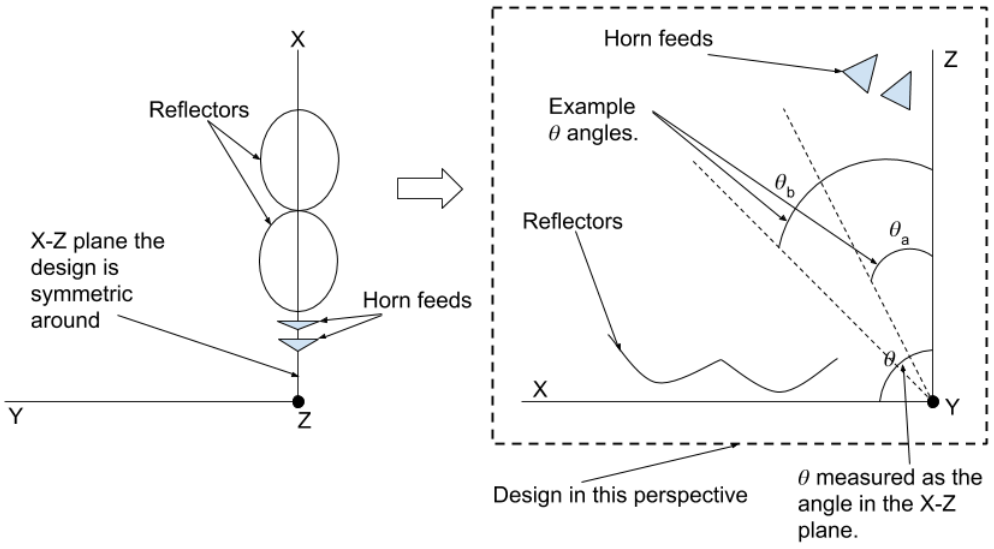

Figure 4.9: Designing in 2-dimensions frequently due to symmetrical nature of design

With the general ideas discussed, the mathematical design of the offset parabolic reflector can commence.

A conic section, is a curve obtained by the intersection of a plane and a cone as shown in Figure 4.10 below. A parabola, hyperbola, ellipse and circle can be found in this manner and are resulting 2-dimensional planar curves (can be fully described with only two variables), laying in the intersecting plane.

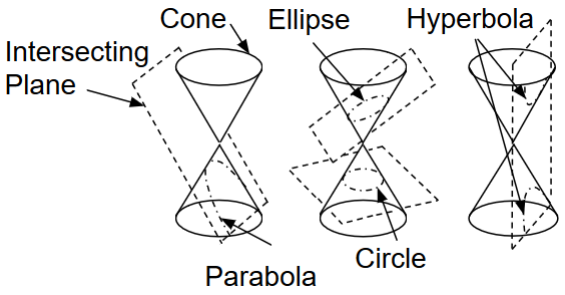

Figure 4.10: Conic section formed from a plane intersecting a cone

The focus, focus point or focal point of a curve are specially named points with which any arbitrary point on the curve have some special relationship. The focus is thus usually a variable in the analytical description of the curve. An ellipse, for example, has the requirement that the sum of each point's distance to both foci are the same. Figure 4.11 shows this clearly.

A circle is a special case of an ellipse. For a circle both the focus points are on the same location and each arbitrary point's sum of their distance to both foci respectively is required to be the same, since a circle is an ellipse, so a ring (or circle) is formed with a distance, called the radius, from the focus point to each point on the circle or ring.

As the focus points separate, the curve also changes shape to still accommodate the requirement that the sum of each point's distance to both foci are the same. The edge points have to be close to one of the focus points and far away from the other one to have the same summed distance as the points in the middle which are the same distance from both focus points. A parabola is a special case of an ellipse, in that one of the foci is at infinity.

The focal length, is the distance from a focus point to the nearest apex. In Figure 4.12 below, f is the focal length and c is the distance between the two focus points. The analytical equation to construct the conic sections as shown in Figure 4.12 is

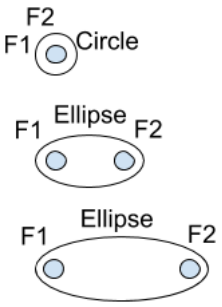

Figure 4.11: Ellipse and circle relation to focus points

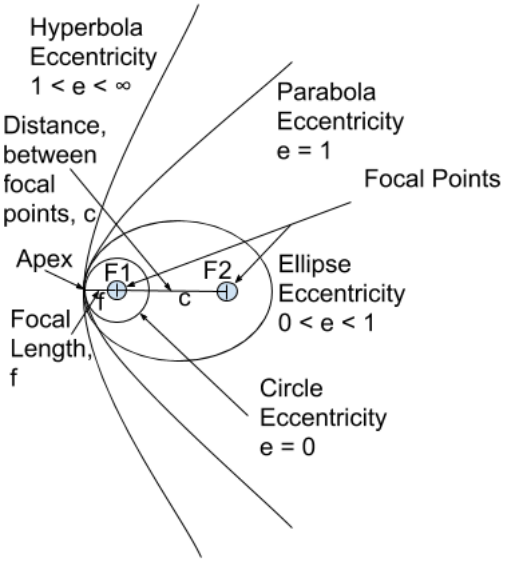

Figure 4.12: Types of conic sections

$$\frac{(z-c)^2}{(f+c)^2} + \frac{y^2}{(f+c)^2-c^2} = 1. \tag{4.3}$$

An important concept is the eccentricity of the curve. As shown in Figure 4.12, a parabola has an eccentricity of 1 and a hyperbola has an eccentricity between 1 and ∞. Eccentricity is a measure of how much a curve deviates from a circle, with a circle having an eccentricity of 0. More formally, eccentricity is a measure of how much the focal points are off-center, where the center is located at the midpoint of the foci. Thus if both foci are on top of each other, they are both centred and the eccentricity is 0. The analytical equation for eccentricity is

$$e = \frac{c}{c+f} = \frac{1}{1+\frac{f}{c}}. \tag{4.4}$$

Taking this definition of eccentricity, rearranging it into making c the object of the equation, and inserting it into (4.3) describing the conic section, results in

$$\frac{(z-\frac{ef}{1-e})^2}{\frac{f^2}{(1-e)^2}} + \frac{y^2}{\frac{(1-e^2)f^2}{(1-e)^2}} = 1. \tag{4.5}$$

The equation for a parabola is found where $e = 1$, and is the result of taking the $\lim_{e\to 1}$ for (4.5) above, as

$$\lim_{e\to 1} \frac{(z-\frac{ef}{1-e})^2}{\frac{f^2}{(1-e)^2}} + \frac{y^2}{\frac{(1-e^2)f^2}{(1-e)^2}} = 1, \tag{4.6}$$

which leads to

$$(z+f) - \frac{y^2}{4f} = 0. \tag{4.7}$$

The equation for a parabola is shown in (4.7). As mentioned before, a 3-dimensional paraboloid can be constructed from rotating a 2-dimensional parabola around its main, or focal, axis. This is how the reflector surface is formed. This necessarily leads to a rotationally symmetric reflector surface.

If the conic section would be rotated around the z-axis to make it 3-dimensional, it would effectively mean that y^2 needs to be replaced by $x^2 + y^2$ to reflect this change. The resulting equation would be:

$$\frac{(z-\frac{ef}{1-e})^2}{\frac{f^2}{(1-e)^2}} + \frac{x^2+y^2}{\frac{(1-e^2)f^2}{(1-e)^2}} = 1. \tag{4.8}$$

The cone with its central axis in the $y-z$ plane, following the same angle parametrisation as shown in Figure 4.13 would have the equation

$$(x^2 + y^2 + z^2)\cos^2\alpha = (y\sin\beta - z\cos\beta)^2. \tag{4.9}$$

The intersection curve of the cone and the conic section is the solution of (4.8) and (4.9) above. By eliminating the x variable from these equations the intersection curve on the $y-z$ plane can be found and has the following form

$$y\sin\beta - z\cos\beta = \pm[ez + (1+e)f]\cos\alpha. \tag{4.10}$$

Selecting the positive sign so that the projection in the second quadrant of the $y-z$ plane is chosen, the equation reduces to

$$y = \frac{(\cos\beta + e\cos\alpha)z}{\sin\beta} + \frac{((1+e)\cos\alpha)f}{\sin\beta}. \tag{4.11}$$

What is of particular note with this equation above is that it is a straight line equation. Where two perpendicular planes intersect, a straight line equation

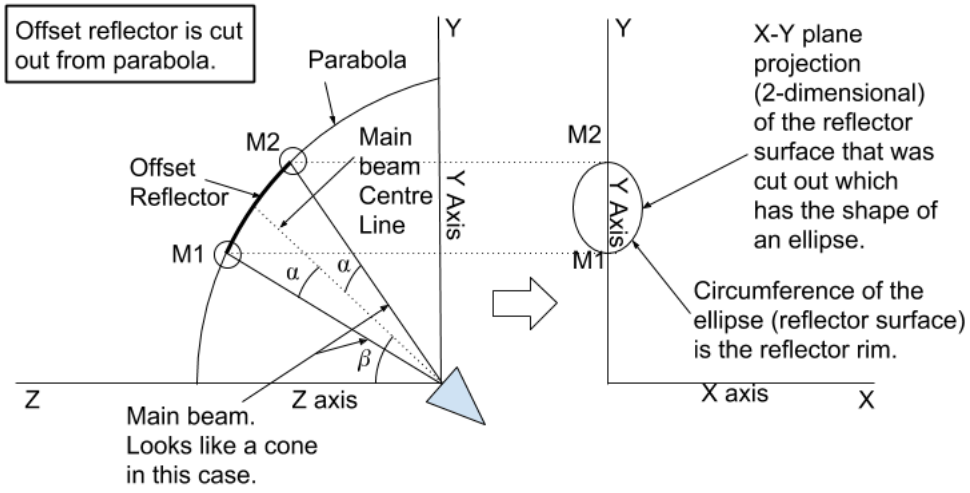

Figure 4.13: Offset parabolic reflector formed from cone intersection with parabola

is the result. What makes this significant is that it is a proof that the reflector surface rim is in fact a planar curve, it lies in a plane perpendicular to the $y-z$ plane, and more particularly it is an ellipse.

To find the intersection curve on the $x-y$ plane the z variable is eliminated from the equations instead of the x variable and this leads to:

$$\frac{x^2}{a^2}+\frac{(y-y_0)^2}{b^2}=1 \tag{4.12}$$

$$y_0=\frac{(1+e)(e\cos\beta+\cos\alpha)(\sin\beta)f}{(1-e^2)\sin^2\beta+(\cos\beta+e\cos\alpha)^2} \tag{4.13}$$

$$a^2=\frac{(1+e)^2(\sin^2\alpha)f^2}{(1-e^2)\sin^2\beta+(\cos\beta+e\cos\alpha)^2} \tag{4.14}$$

$$b^2=\frac{(1+e)^2(\cos\beta+e\cos\alpha)^2(\sin^2\alpha)f^2}{((1-e^2)\sin^2\beta+(\cos\beta+e\cos\alpha)^2)^2}. \tag{4.15}$$

No other information is necessary after this point to construct the reflector surface. Since the intersection curve on the $x-y$ plane provides the $x-y$ plane region of the conic section that will be used as the reflector surface. By cutting that region out of the conic section and associating the applicable conic section z coordinate information with the region, which is possible since 3-dimensional information about the entire conic section is available, the full 3-dimension reflector surface can be obtained.

This entire process has the result of being able to produce reflector surfaces that are only dependant on three variables and thus explicitly stated can only be influenced and changed by these variables. They are:

1) β angle of the horn. The angle at which the horn observe the reflector.

2) α angle of the horn. The taper angle of the horns pattern.

3) F of the reflector. The focal length of the reflector. How far the focus point is from the reflector's apex.

The angles are the same angles as seen in Figure 4.13. The focus point of the reflector is where the energy is being directed to. Thus the feed will be at the focus point to receive the most reflected radiation energy. The feed horn has a phase centre, similar to a focus point, and thus the feed horn's aperture cannot be positioned at the focus point of the reflector, but the feed horn's phase centre has to be placed at the focus point. Figure 4.14 shows this.

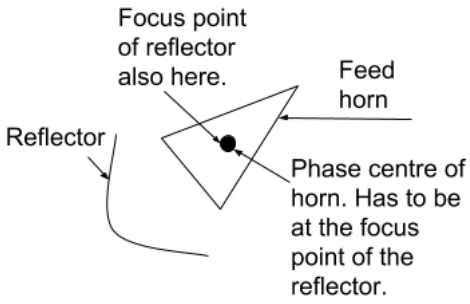

Figure 4.14: Phase centre of horn needs to be at focus point of the reflector

From these variables listed above and Figure 4.13, certain deductions can be made before designing the system.

1) β angle of the horn. This variable will change the part of the conic section that will be cut out for the reflector surface. This variable thus changes the shape of the reflector surface.

2) α angle of the horn. This variable changes the size of the reflector surface, since when the α angle increases, more of the conic section is cut out.

3) F of the reflector. This variable will change the size of the reflector surface. When the focal length becomes larger the feed is further away from the reflector, since the feed has to be at the reflector's focus point. The reflector surface has to be larger now to still reflect most of the energy inside the taper angle specified for the horn pattern.

Thus an offset reflector system, by using these three variables, has to be designed. The amount of distinct angles to observe in is four, requiring four reflectors and four feeds, but only two of each have to be designed since the system is symmetrical. The reflectors should not overlap as they would cause aperture blockage for the reflector they overshadow reducing that reflector's efficiency.

Consider the case shown in Figure 4.15 below. If the angle to observe in is not directly in front of the reflector, but shifted by an arbitrary amount, for example 30° or $\frac{\pi}{6}$ radians, it would look like it is shown in Figure 4.16:

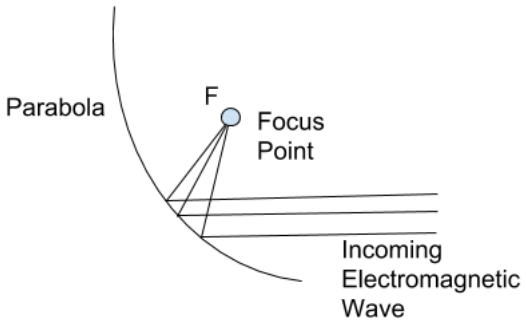

Figure 4.15: Parabola reflecting waves to a focus point

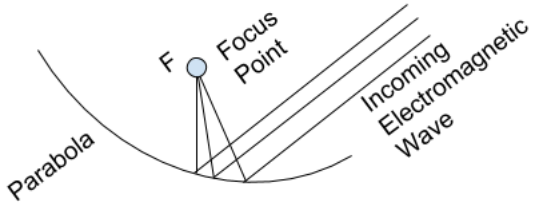

Figure 4.16: Rotating to receive wave from a different angle and reflect to focus point

This is effectively done by rotating the reflector or parabola by the same angular amount. Additionally, the reflector would have to be translated to ensure that it does not intersect with other reflectors. Taking all these requirements and variables into account, a design was done and shown in Figure 4.17.

This design takes into account all the previous requirements stated, but it also expands on it. The reflectors are positioned next to each other so that one large interpolated reflector can be formed. The biggest advantage of this one large

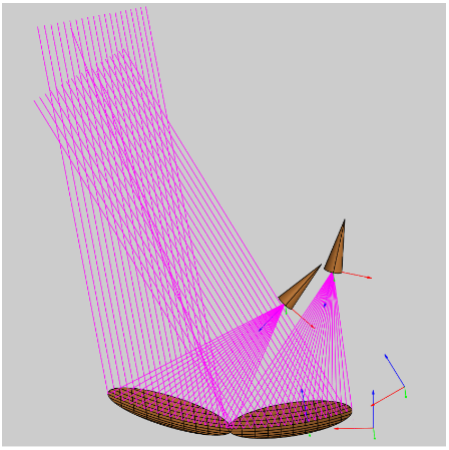

Figure 4.17: Feed horns and two reflectors to receive at 10° and 30° angles

interpolated reflector, is that it is easier to manufacture leading to a lower cost.

Additionally, the design also needed to satisfy the following requirement:

1) There are no intersections.

2) The reflectors are close to the same depth.

3) They have close to the same focal length, so that the distance from the feeds to their reflectors are relatively the same, which results in relatively the same size for the reflectors if the feeds' α angles are also the same. This also makes their gains relatively the same, thus not more or less sensitive in the different directions.

4) As little aperture blockage as possible.

5) Radiating in the correct directions.

6) Horns close to each other to make the mechanical design easier.

The design was done by taking all these requirements into account, and using the variables to adjust the position and size of the reflectors and horns manually, until a satisfactory result was obtained. The design in Figure 4.17 reaches all these specifications. The design values are listed in Table 4.1.

The program used here for development is called GRASP. The ray tracing seen in Figure 4.17 is a good indication of how the system will behave, but still an electromagnetic analysis is required to see the radiation patterns the system will form. These are also generated by the same program and can be seen in Figure 4.18. Physical Optics (PO) is used and is valid because the reflector is

Table 4.1: Parameters for designing the offset reflector system

Parameter	**Value**
α_1	20°
α_2	20°
β_1	42.95°
β_2	52.64°
F_1	0.36 m
F_2	0.33 m
Taper Angle	20°
Taper dB	-10 dB
Reflector_1 Rotation Angle_1	30°
Reflector_2 Rotation Angle_2	10°
Reflector_1 Translate in x	0.08 m
Reflector_2 Translate in x	-0.165 m
Reflector_1 Translate in z	0.108 m
Reflector_2 Translate in z	0.01 m

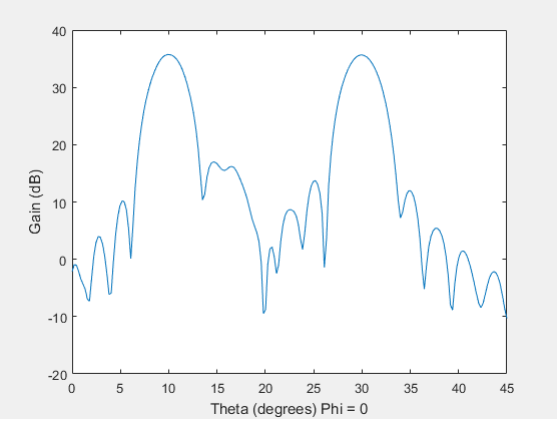

Figure 4.18: Radiation pattern of offset reflector system design

a smooth surface.

From this radiation pattern the directions of observation (the peaks) are exactly where it was designed at 10° and 30°. The gain of both reflectors are similar meaning they will have similar sensitivity in their respective directions of observation, which is required.

Furthermore the sidelobe level is 16.91 dB -35.73 dB $= -18.79$ dB. It is not quite the -20 dB designed for, but it is close. This is a prototype design at its core. Its function is to test the viability of the design, it thus does not have to meet the required specifications strictly, but has to at least be viable

and strive for them to validate any consideration to be recognised as a proof of concept. By increasing the size of the reflectors in this design, the gain can be increased and the sidelobe level can go even lower.

The next step is to interpolate the reflector surface using the method in [18]. The result of the method is shown in Figure 4.19. The reason the reflector surface is interpolated is to merge the two reflectors, while keeping the resulting surface area smooth.

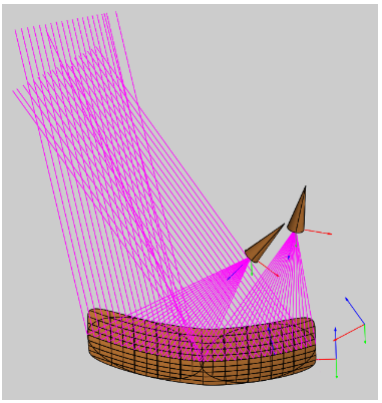

Figure 4.19: Merging both offset reflectors into one using interpolation techniques

A super ellipse is used so that the single interpolated reflector surface has a rim in the shape of an super ellipse, with the resulting single surface area deviating as little as possible (low error) from the two individual reflectors surface areas. The super ellipse is used because the individual reflectors are ellipses, which means that the super ellipse wraps around the surfaces easily. Figure 4.20 shows this.

Using a super ellipse keeps the added surface material to a minimum for cost, but also because any surface material added in this way is outside of the design and will likely result in some radiation in unwanted directions.

The error will increase with additional surface area added as well as the relative position of the surface area added. If it is added in location with high radiation, then the error it will cause (increasing the sidelobes) will be significantly more than if it was placed at an edge location where there is not a lot of radiation. Since the area added by the interpolation technique is at the edges of the reflectors where the radiation is less significant, the expected result is that the effect on the radiation pattern will be reduced.

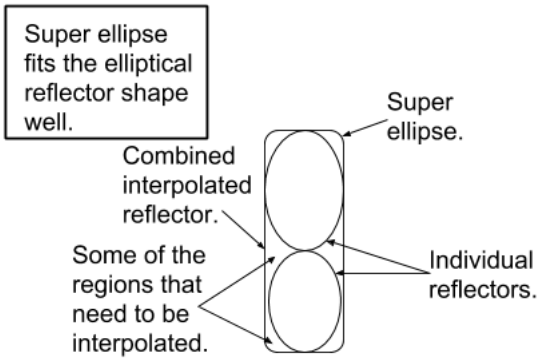

Figure 4.20: Super ellipse used with interpolation technique to wrap the two reflector surfaces into one combined one

In Figure 4.19 the original two reflectors are also shown in the interpolated reflector for comparison to the one large interpolated reflector. The interpolation performed well keeping the entire surface smooth. This is relatively important since at a high frequency small errors (like bumps) in the surface could result in sidelobes increasing noticeably, because the waves are so small they react to small surface discontinuities. The interpolated reflector has a projected x-axis length of 0.6168 m and a projected y-axis width of 0.294 m.

The radiation pattern and how much it is affected is shown next in Figure 4.21. The blue plot is the interpolated design, while the orange plot is the non-interpolated design.

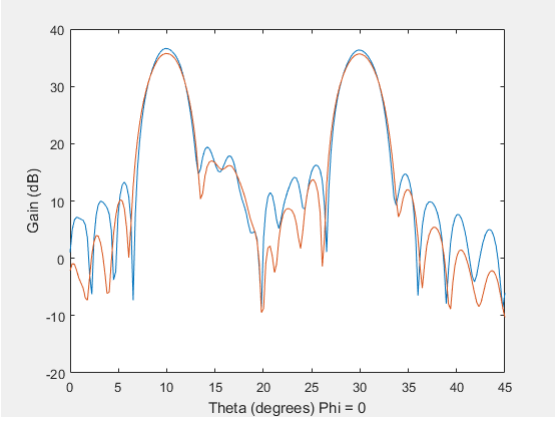

Figure 4.21: Radiation of interpolated reflector design

The system performs similar. The sidelobe levels did raise noticeably and now sits at 19.26 dB -36.61 dB $= -17.35$ dB, which is a bit higher than before the interpolation. This is not unexpected, having more surface area than

originally intended in the design, means that some radiation gets scattered into directions never designed for. This will lead to increased sidelobe levels. It is still acceptable. The next step will be to do a full-wave analysis in FEKO.

In Grasp, the feeds are approximated as radiating Gaussian beams with a certain taper. Their size are also approximated as the equivalent horn antenna that would be required to produce a pattern similar to what is specified. The feed horns, however, are never designed. Thus, they have to be designed in FEKO before a full-wave electromagnetic analysis can be done to see how well the system performs.

4.3 Conical Feed Horn Design

A conical horn has to be designed so that the feed horns have a relatively circular radiation pattern, as a circular pattern for the horn was used in how the offset reflector was formed from the conic section and how the design was done in GRASP. To do this design the equations for a conical horn antenna as shown in [10] was used.

The Gaussian beam pattern used in GRASP as seen in Table 4.1 had the specifications of -10 dB taper at 20°. A horn with a similar pattern is thus required to mimic the behaviour of the approximated horn design by GRASP. The equation for calculating the directivity D of the conical horn antenna as shown in [10] is rewritten to make the aperture radius a the object as shown in the equation below.

$$D = 10log_{10}\epsilon_{ap}\frac{4\pi}{\lambda^2}(\pi a^2) \tag{4.16}$$

$$a = \sqrt{(10^{(\frac{D}{10})})\frac{\lambda^2}{4\epsilon_{ap}\pi^2}}. \tag{4.17}$$

The variable ϵ_{ap} is the aperture efficiency and the directivity of a conical horn antenna is optimum (max gain for given length) when the aperture diameter d_m of it is $d_m \simeq \sqrt{3l\lambda}$. This corresponds to an aperture efficiency of $\epsilon_{ap} \simeq 0.51$.

Figure 4.22 shows the relevant variables in relation to the conical horn and its circular waveguide.

The equations below show how these variables are deduced for an optimum directivity.

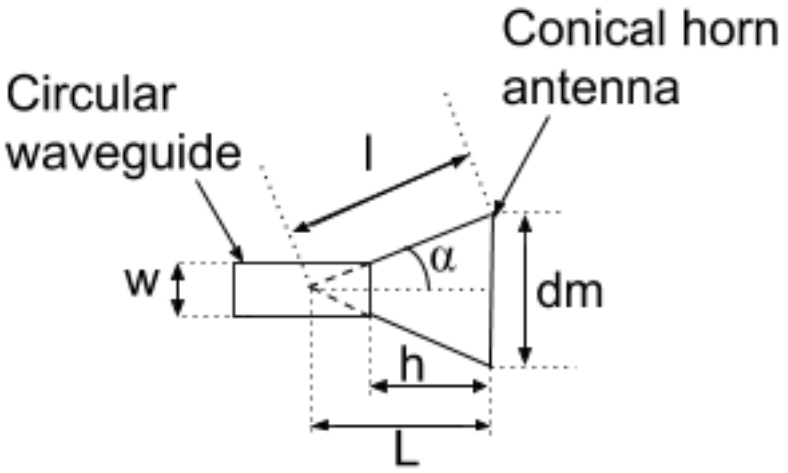

Figure 4.22: Conical horn and waveguide variables

$$l = \frac{((2a)^2)}{(3\lambda)} \tag{4.18}$$

$$\alpha = sin^{-1}\frac{a}{l} \tag{4.19}$$

$$L = lcos\alpha \tag{4.20}$$

$$h = L - \frac{\frac{w}{2}}{tana}. \tag{4.21}$$

Before the horn construction is discussed, a circular waveguide also needs to be designed to attach to the base of the horn. This waveguide is seen in Figure 4.22. To have the waveguide operate at the required frequency of 22.2 GHz the following (4.22) designs for it [19]:

$$f_c = \frac{1.8412c}{2r\pi}. \tag{4.22}$$

In (4.22) f_c is the cut-off frequency where the wave gets attenuated (filtered) if the frequency is below the cut-off. This frequency is chosen as $f_c = 0.7(22.2)$ GHz which is 30 percent below the operating frequency. Rearranging (4.22) to have the radius of the waveguide $r = \frac{w}{2}$ as the object results in (4.23):

$$r = \frac{1.8412c}{2f_c\pi}. \tag{4.23}$$

Substituting the variables, where c is the speed of light in a vacuum, yields $r = 5.66$ mm. This is thus chosen as the radius for the waveguide.

Finally, since only the radius r of the waveguide is used to determine the cut off frequency in (4.22), the length can be chosen arbitrarily. The length is thus chosen as 30 mm.

The beam angle needs to be 20° at -10 dB taper. The directivity is set to 18 dB and these variables shown above, a, l, α, L and h are calculated. The design is then constructed in FEKO as shown in Figure 4.23.

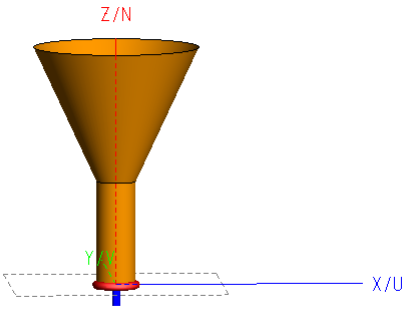

Figure 4.23: Horn antenna designed in FEKO

The variables were determined as, $a = 47.8$ mm, $l = 56.4$ mm, $\alpha = 25.06°$, $L = 51.1$ mm and $h = 39$ mm. It has a length of 69 mm. It is important that the feed does not become too large as it becomes both expensive, heavy and makes the design more difficult as it could cause aperture blockage. Since GRASP takes approximate horn sizes into account, this horn design size should be well within the acceptable parameter. It has an aperture diameter size of 47.8 mm. The radiation pattern is shown in Figure 4.24.

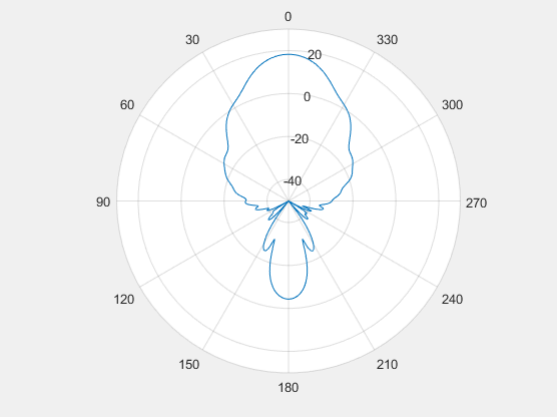

Figure 4.24: Polar Radiation (Gain) pattern of horn antenna

This design has a taper of 8.15 dB -18.2 dB $= -10.05$ dB at 20° which is what was designed for. A corrugated horn design could have been made, but it is more expensive to make and the design specification is already met. Adding

corrugations can also lead to the horn being heavier which requires more sturdy mechanical components to keep it in place which increases cost [1].

The final step is to see how well this performs in the combined system, doing a full electromagnetic analysis in FEKO. The simulation model is shown in Figure 4.25.

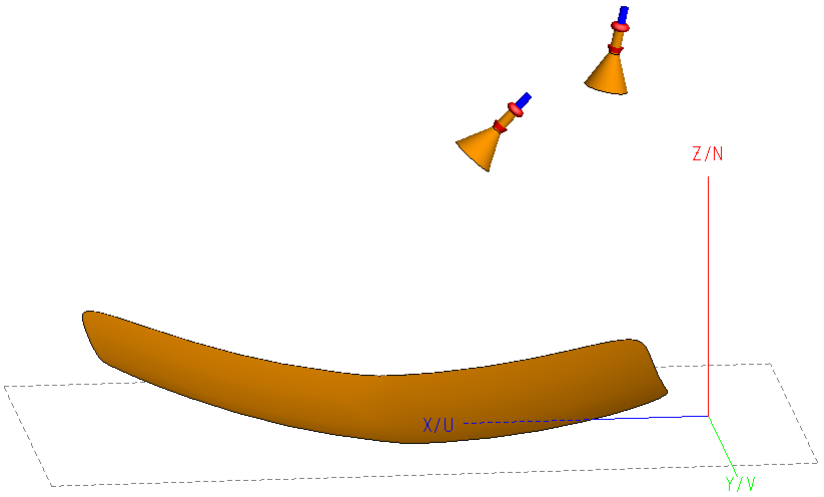

Figure 4.25: Full interpolated reflector with horn antennas designed in FEKO

The radiation pattern of this design is shown in Figure 4.26.

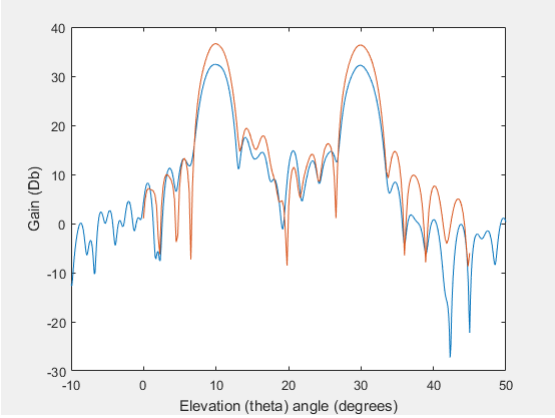

Figure 4.26: Radiation pattern of full reflector design comparing gains at 10° and 30° angles

In Figure 4.26 the blue plot shows the reflector system radiation pattern using the designed horn, while the orange plot shows the GRASP reflector system radiation plot. The reflector system using the designed horn, has similar gain at the peaks, with about a 0.2 dB difference between the gain at 10° and 30°. The closer the gain at both angles are compared to each other the better, so this result is good. The sidelobes have dropped to 17.5 dB − 32.4 dB = −14.9 dB. This is not good, and is simply too far below specification for the design to pass as a proof of concept. The gain also dropped notably by about 4 dB compared to the GRASP plot. One solution to this problem would be to design a horn with a higher gain and a higher taper at the specified angle and using a larger reflector.

Designing a horn antenna that performs well and manufacturing such an antenna requires both time and money. Instead of following this route, a horn antenna with a lens and a higher gain was purchased. Purchasing this antenna would not be significantly more expensive than manufacturing a unique design, in fact it might be cheaper. It also has a lens which makes the antenna smaller for a higher gain.

4.4 New Feed Horn Simulations

The horn that was purchased is shown in Figure 4.27. The electrical specifications of the horn is listed below in Table 4.2.

Figure 4.27: Horn that will be bought [4]

This antenna has a total length of 4.04 inches or 102.616 mm. This length is longer than the original GRASP design horn, which means it could cause aperture blockage, or stated differently, it could cause the system to have high sidelobes since some of the energy from the one horn will be bouncing off the other horn, as the other horn is in its path of radiation. That energy then gets

Table 4.2: Electrical characteristics of bought horn [4]

Parameter	Minimum	Typical	Maximum
Frequency	22 GHz	N.A.	26.5 GHz
Gain	N.A.	22 dBi	N.A.
3 dB Beamwidth	N.A.	12°	N.A.
Side Lobes	N.A.	N.A.	-20 dB
Polarisation	Linear	Linear	Linear
Return Loss	N.A.	1.2:1	N.A.

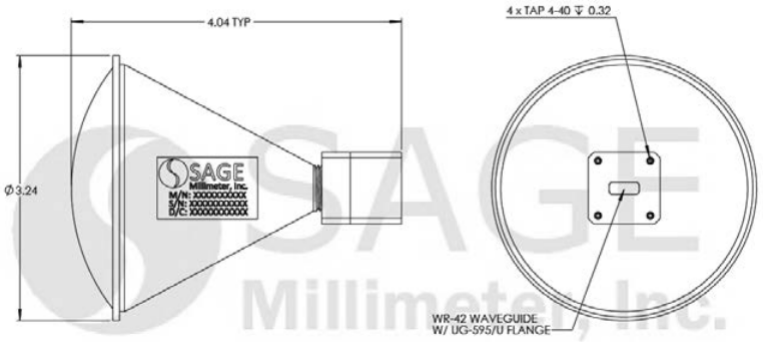

Figure 4.28: dimensions of bought horn [5]

scattered resulting in higher radiation in unwanted directions which naturally causes the sidelobes to rise.

The first step thus has to be to make sure that this design does not cause notable aperture blockage. The testing procedure for this is to find a manner in which the full antenna design can be simulated without taking into account the aperture blockage caused by the antenna, and then simulating it with the effect taken into account. If both these simulations yields similar results, then aperture blockage cannot have a noticeable effect. If they do not, then the system will have to be redesigned.

A difficult part of the simulation regarding this bought horn is that a model of the horn is not available. The entire antenna thus has to be designed in FEKO or some software package which would take considerable time, or certain parts of the antennas behaviour can be simulated which will be much faster. If the geometry has to be tested as is the case for determining aperture blockage by the horn, then the most important information is the antenna size. A horn antenna that has the same size without necessarily the same electrical characteristics would be able to be used to determine aperture blockage, since in this case it is mainly due to one horn antenna being in the radiation path of

the other one.

Furthermore, if the electrical characteristics of the antenna being bought is of concern then the physical dimensions does not have to be exact. This makes modelling the bought antenna behaviour much faster without compromising notably on the integrity of the tests.

A Physical Optics (P.O.) simulation will be performed first, which does not take into account the aperture blockage of the antenna at all, since the antennas are considered individually. Secondly, a multilevel fast multipole method (MLFMM) simulation will be done, which does take aperture blockage into account.

A comparison between the MLFMM and P.O. simulations are shown in Figure 4.29 and Figure 4.30 below. The orange plot is the MLFMM simulation, while the blue plot is the P.O. simulation.

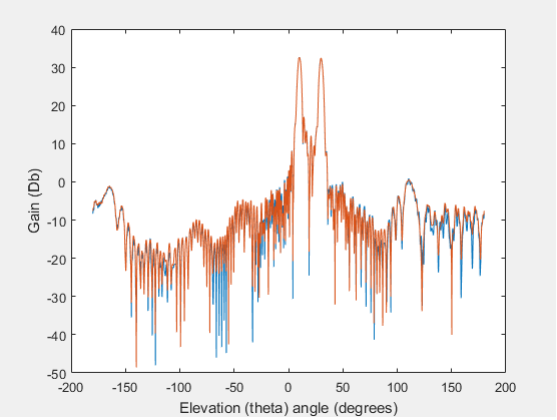

Figure 4.29: MLFMM and P.O. simulation radiation patterns compared

From Figure 4.30 the radiation patterns are similar. Thus aperture blockage has almost no effect on the simulation results, meaning the horn is not big enough to cause noticeable aperture blockage. If aperture blockage were to have occurred, it would likely have occurred at the 30° angle because the 10° horn would be in its way, if the horns were too large. Figure 4.31 shows what is being meant.

To determine the radiation patterns of the reflector system using the bought antenna is difficult because no model is available. The radiation pattern behaviour of the bought antenna, however, is known and is shown in Table 4.2. To model the electrical characteristics, the geometry is not that important. The

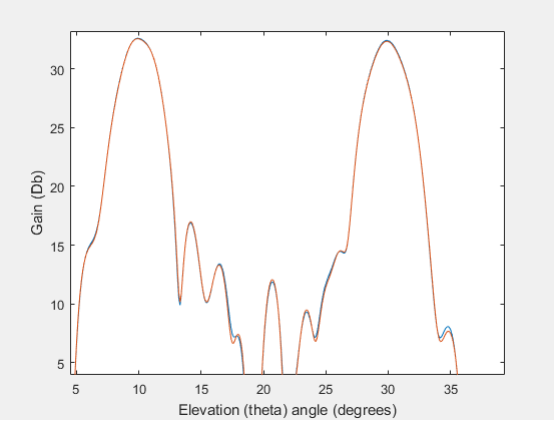

Figure 4.30: MLFMM and P.O. simulation mainlobes compared

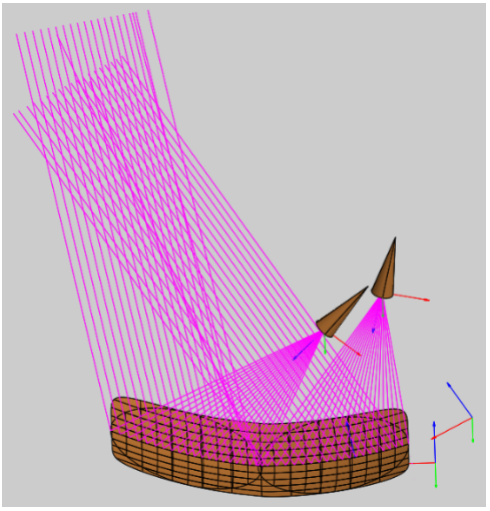

Figure 4.31: Horn responsible for receiving at 10° could have potentially blocked radiation received by the horn responsible for receiving at 30°

important parts is to have approximated 22 dB gain, 12° -3 dB beamwidth and -20 dB sidelobes. Figure 4.32 shows a horn antenna design that satisfied these parameters.

The gain radiation pattern of this horn antenna design is shown in Figure 4.33 below.

This design has a slightly higher gain of 0.3 dB at 0° compared to the bought horn and -3 dB taper at 12°, so 6° on each side from 0°. Getting both exactly the same is difficult to do, so a good approximation is chosen. Furthermore, the sidelobes and back radiation are well below -20 dB from the mainlobe at 0°. The most important thing to approximate is the gain and the taper pattern

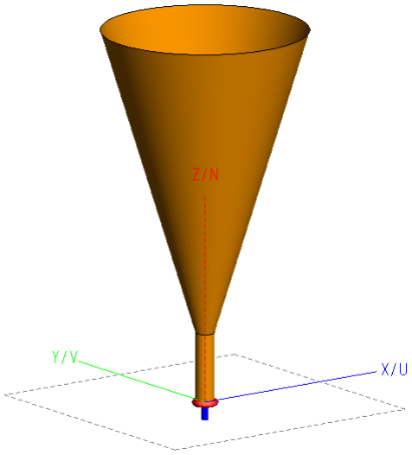

Figure 4.32: Horn design for approximating the electrical characteristics of the bought horn

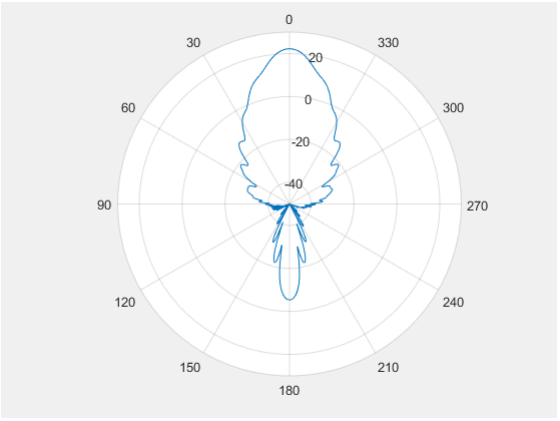

Figure 4.33: Radiation pattern of the approximated horn design

so that the gain radiation pattern at specifically 10° and 30° can be accurately determined.

This horn design electrical characteristics will not be exactly the same as the horn being bought, since they have fundamentally different designs. This horn, however, approximates most of the important characteristics and will be a good indicator of how the bought horn will behave in the system.

It is important to note that the antennas designed here are significantly larger than the horns that will be bought and will probably cause aperture blockage. These horns, however, do approximate the electrical characteristics. To do a simulation without taking the aperture blockage into account that these approximated horns might cause, a P.O. simulation will be done. The results

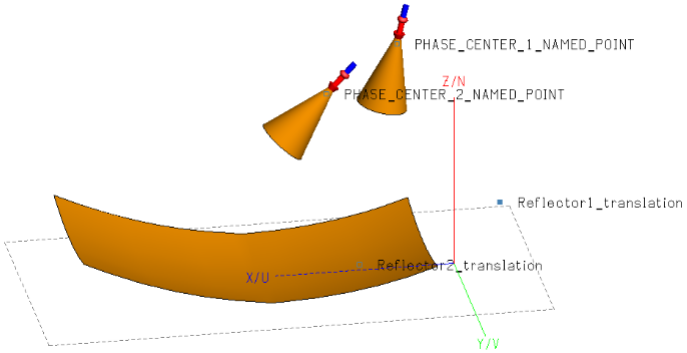

Figure 4.34: Using the new horn approximating the electrical characteristics of the bought horns

are shown in Figures 4.35, 4.36, 4.37 and 4.38.

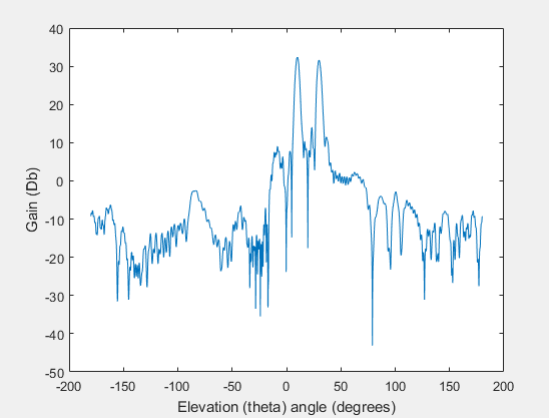

Figure 4.35: Radiation pattern of the full reflector system with the approximated horn designs

In Figure 4.36 the blue plot is the reflector system radiation pattern using the approximated horn design. The orange plot is for the reflector system using the designed horn and the yellow plot is the reflector system radiation pattern from GRASP. The sidelobes using the approximated design is notably lower than when using the designed horn.

For the reflector system using the approximated horn design, the gain difference between the two major angles is 32.38 dB -31.53 dB $= 0.85$ dB. The sidelobe level is at 13.99 dB -31.53 dB $= -17.54$ dB. A sidelobe level of -20 dB instead of -17.5 dB would be preferable as well as a gain difference of about 0.1 dB. It has a -3 dB beamwidth of about $30° - 28.3° = 1.7°$. A -3 dB beamwidth of less than 3° would have been desirable, so this result is better

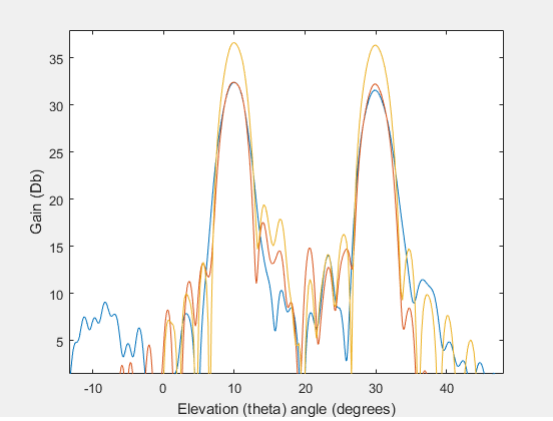

Figure 4.36: Comparing gains at the two major angles for the full reflector system using the approximated horn designs

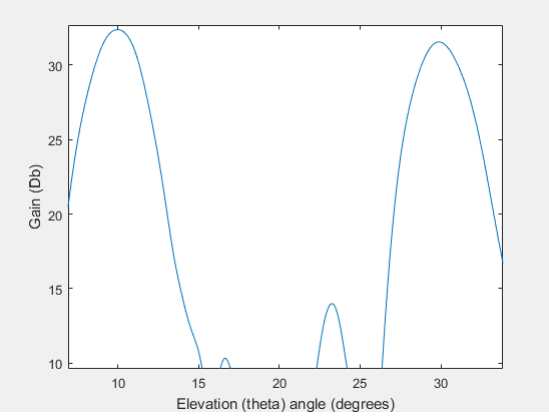

Figure 4.37: Comparing the sidelobe level to the mainlobe of the full reflector system

than the specification.

The antenna system behaves well, but improvements can be made. Redesigning the system a few times to try and get the gain differences at the peaks to be closer can be done or a more directional horn antenna can be designed to bring the sidelobe level lower. A larger reflector can then be used to increase the gain of the system. In the end this design serves as a proof of concept whether this design is feasible, and in that regard the design succeeded as the results are acceptable and improvements can be made.

The last steps are to design the mechanical support for both the reflector and the horns to keep them in place and then to test the system.

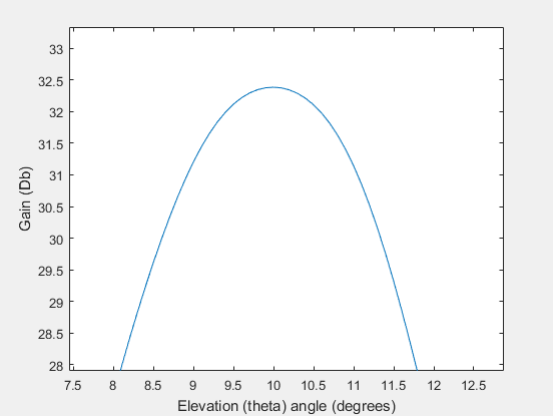

Figure 4.38: Showing the -3 dB beamwidth of the full reflector system

4.5 Measured Results

The bought horn was measured at the University Stellenbosch antenna measurement room with an NSI instrument, doing a spherical near field measurement that was then transformed to a far field. Its measured radiation pattern was imported into GRASP. In GRASP various simulations were performed at various distances K from the reflector focus point, along the horn axis, to determine experimentally where the phase centre of the bought horn was. The concept is shown in Figure 4.39. The dotted horn in Figure 4.39 is not present in the simulations, and only serves to show what is meant by the horn axis. Only one horn was bought, and thus only one of the horn positions are used. Both horns are removed from the system and only the imported radiation pattern is varied to determine the distance K that results in the maximum gain for the system.

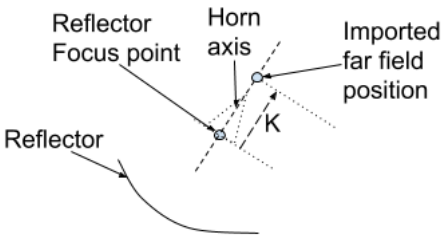

Figure 4.39: K varied to determine phase centre of horn

After this simulation was performed at distances K from 0 mm to 68 mm, having a resolution of 1 mm (0.0741λ) for 0 mm to 20 mm and then a resolution of 2 mm (0.1482λ) from 20 mm to 68 mm, the mainlobe gain (at 30°) were plotted for various K values (orange plot) and a parabola was fitted to the

results (blue plot). This is shown in Figure 4.40. The peak of the parabola occurs at 13.7 mm. The horn was measured relative to a coordinate system as shown below in Figure 4.41. The far field was extracted from this set up and thus the 13.7 mm value for K is interpreted relative to the relevant coordinate system. This puts the phase centre just below the SMA connector.

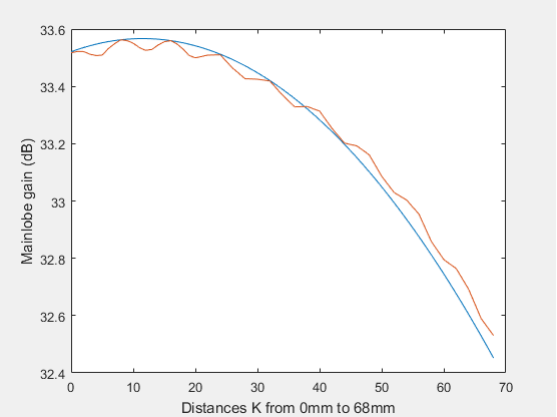

Figure 4.40: Gain for various K distances

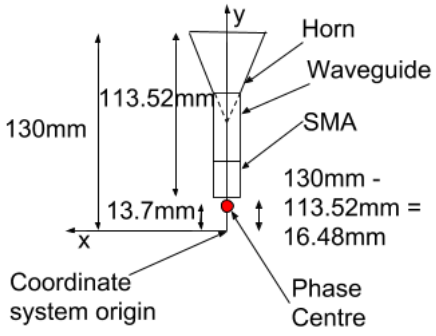

Figure 4.41: Phase centre for measured horn

The FEKO simulations for the conical horns had their waveguides start at the coordinate axis origin, as shown below in Figure 4.42.

The phase centre for the horn modelling the behaviour of the bought horn has to be calculated to correct the simulation positions. This is important as the positions for the horns relative to the reflector is needed to accurately measure the reflector system. Thus, moving the measured horn, as seen in Figure 4.43, down by 16.48 mm to the coordinate system origin also moves the phase centre

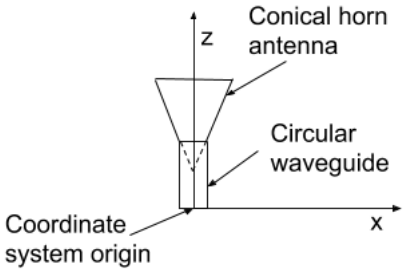

Figure 4.42: Simulated horn setup

down 16.48 mm.

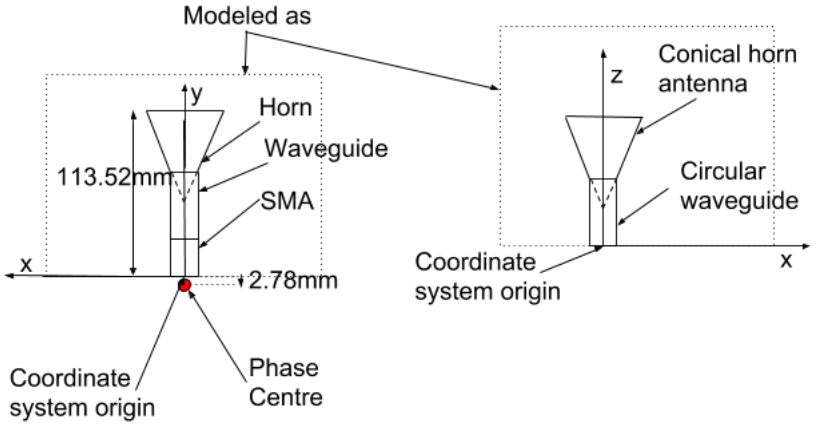

Figure 4.43: Phase centre for simulated horn

The phase centre of the horn has to be positioned in the reflector system exactly on the focus point of the reflector to maximize the gain. This is shown in Figure 4.44, where $U = 13.7$ mm $-$ 16.48 mm $= -2.78$ mm.

The final positions of the horns relative to the reflector is shown in Figure 4.45. The distance is measured from the edge point of the reflector to the start of the waveguide of the horns, in the centre.

The physical reflector system built is shown in Figures 4.46, 4.47 and 4.48. It is also shown in the measurement room, just before being measured in Figure 4.49. The reflector is made from aluminium and the mechanical supports are constructed in the form mentioned earlier in the thesis to reduce aperture blockage. Finally, the mechanical supports allow the horn to be repositioned which is useful as only one horn is bought. This horn is then positioned on

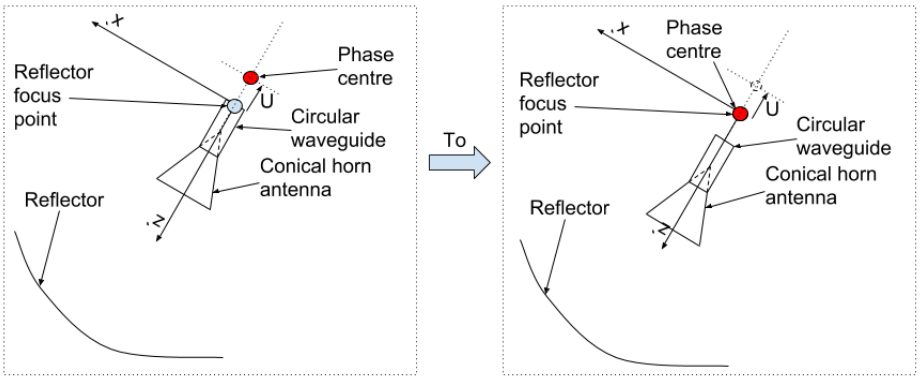

Figure 4.44: Moving horn phase centre to focus point in reflector system

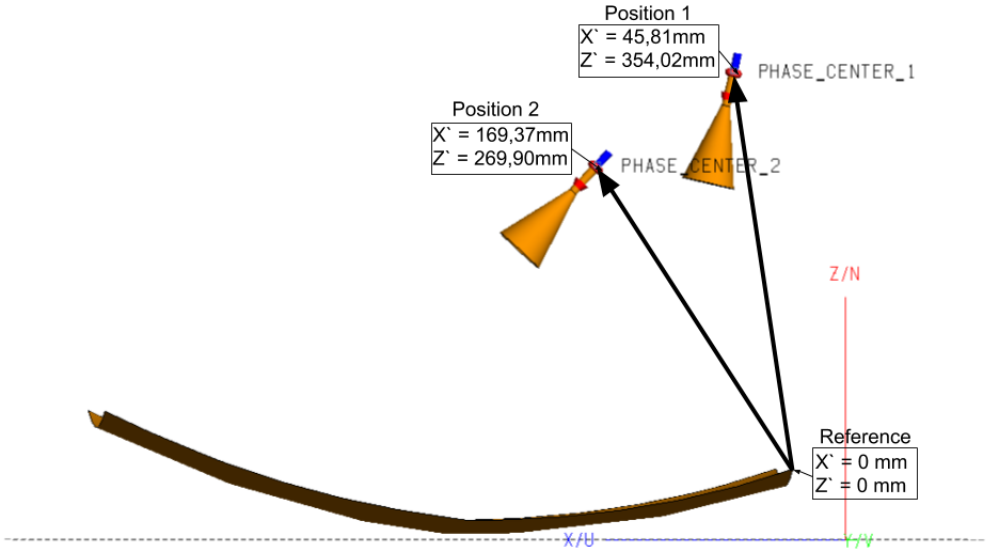

Figure 4.45: Horn positions relative to reflector

both horn positions to measure the radiation patterns.

The reflector system measurement will consist of doing a planar near field measurement that will then be transformed into a far field. Three different near field areas were simulated to determine what area to measure to still be accurate. The first simulation is shown in Figure 4.50 below. As stated earlier the relatively large horns, compared to the bought horn, model the radiation pattern of the bought horn and Physical Optics simulation is used to ignore the aperture blockage that can be caused by their size.

In Figure 4.51, the blue plot is the transformed near field while the orange plot is the far field simulation of the reflector system. They compare relatively well around the main radiation angles, being 1 dB off at the main lobes, while

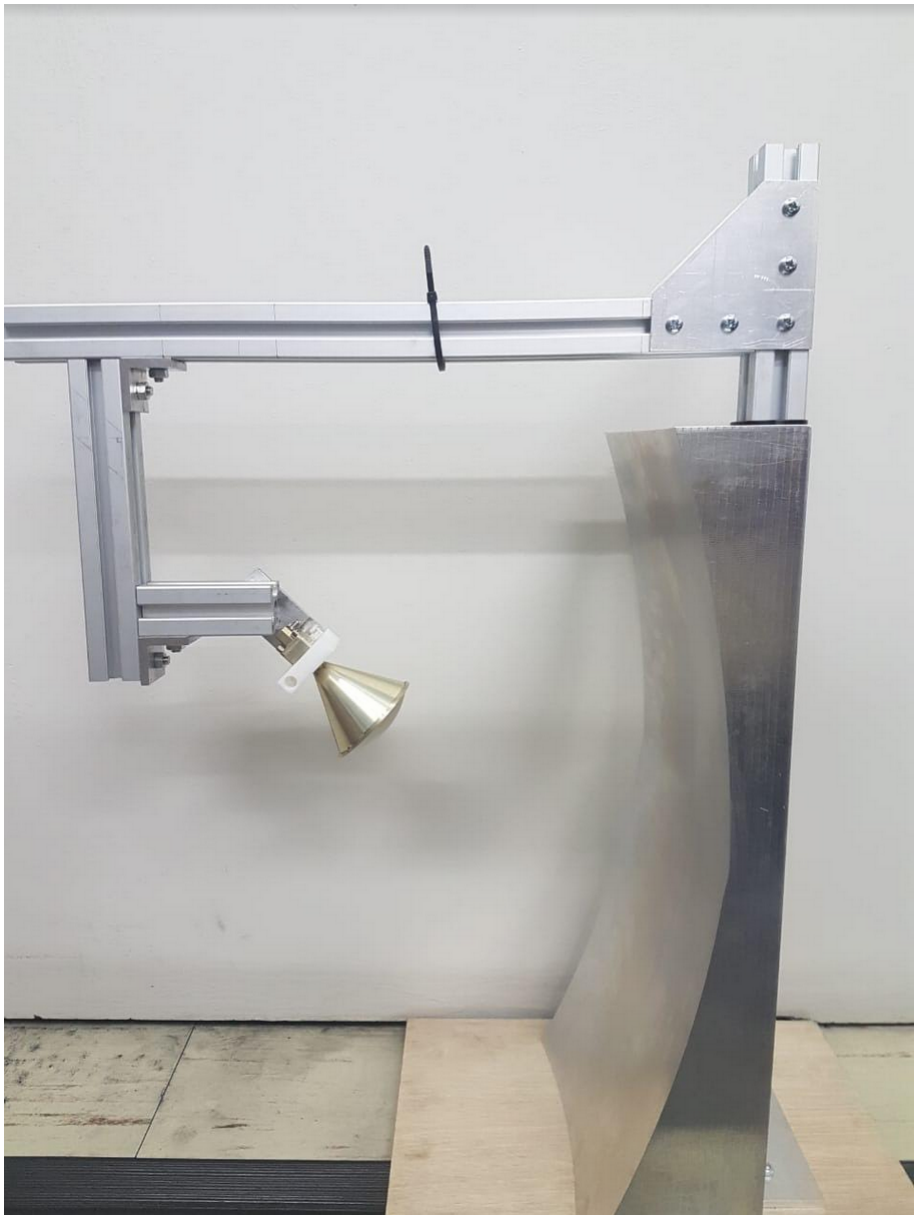

Figure 4.46: Physically built reflector system

being completely mismatching at the other angles. This makes sense as the near field area captures most of the radiation in the main radiation angles while not capturing the radiation in the other angles, thus the representation in the other angles will be inaccurate. This, however, is not important as the other angles have radiation notably lower than the sidelobes and can thus be ignored. In Figure 4.52 below the second smaller near field area (medium area) simulation is shown. This smaller near field simulation compares worse with the far field simulation, than the previous bigger near field simulation did. The result can be seen in Figure 4.53. This is understandable as the smaller zone

Figure 4.47: Physically built reflector system

means less radiation information is captured and thus the representation of the far field is less accurate. Finally, the third smallest near field plane (small area) is shown in Figure 4.54. The result is shown in Figure 4.55. This result is the worst as the sidelobes are notably higher than the far field simulation. From these tests, the largest near field plane was taken as the area to measure for relatively accurate results, even though it has a 1 dB error. The reason for this is that it is difficult to set up the horn in the correct position, and a 1 mm or 1° error is easy to make. Additionally the larger the plane that will be measured, the longer the antenna takes to measure. Even if a plane can

Figure 4.48: Physically built reflector system

be chosen that perfectly measures the antenna, the positioning errors for the horn during measurement would cause inaccurate results.

Since only one horn was bought, only one horn position was measured in the reflector system at one time. The result for the horn responsible for the majority of the radiation at 30° is shown in Figure 4.56. The measured result is the orange plot while the simulated result is the blue plot. The far fields are normalized.

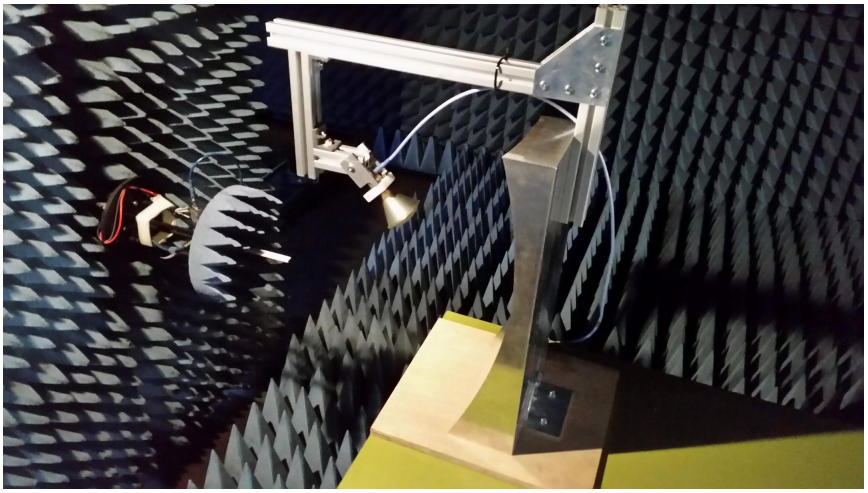

Figure 4.49: Physically built reflector system just before measurement

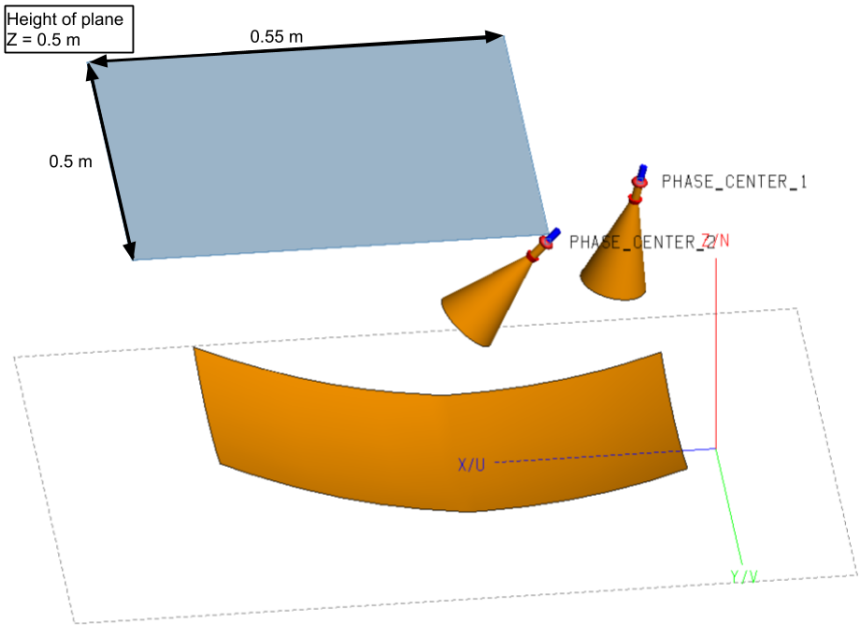

Figure 4.50: Large near field area simulation set up

From Figure 4.56 the measured result has notably higher sidelobes making the sidelobe level around -16 dB. The mainbeam corresponds almost exactly at the 30° angle making the measured beamwidth almost exactly the same as the simulated beamwidth. Doing measurement at relatively high frequency is difficult as small misalignments lead to notable changes in the results. Due to this the measured results corresponds relatively well with the simulated pattern, however, the sidelobe level of the physical system is too high at -16 dB.

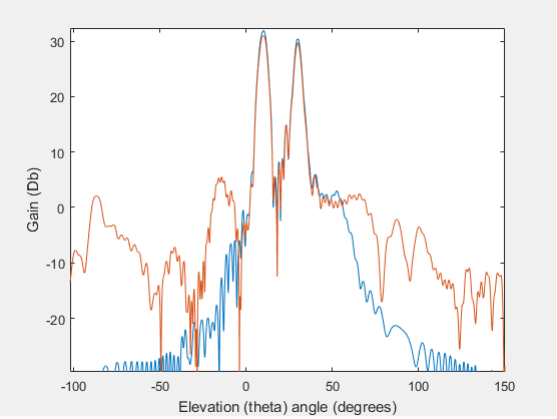

Figure 4.51: Large near field area simulation results

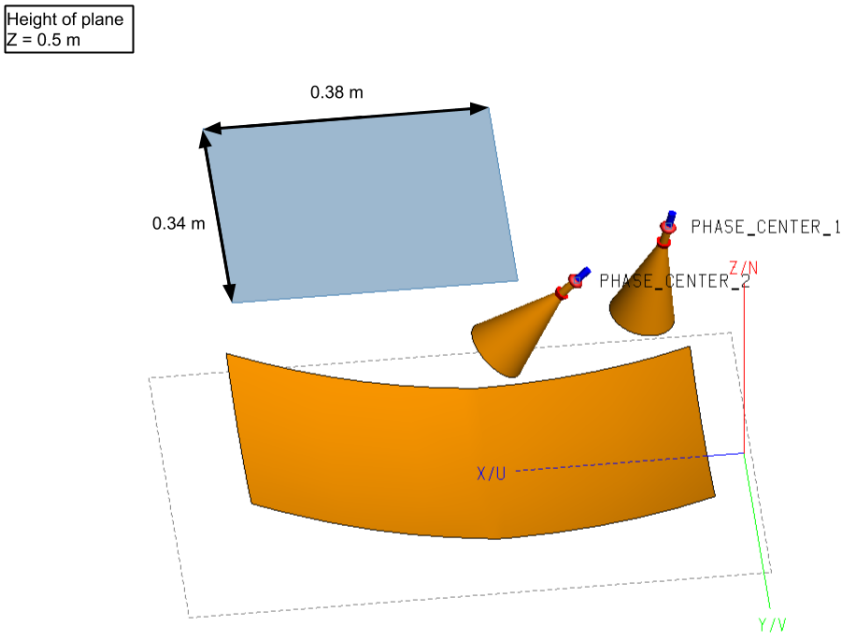

Figure 4.52: Medium near field area simulation set up

Finally the result for horn responsible for the majority of the radiation at 10° is shown in Figure 4.57. The orange plot is for the measured result while the blue plot is for the simulated result.

In Figure 4.57 the beamwidth corresponds very well again, while the sidelobes are notably higher than the simulated result. Once again at a sidelobe level of around -15 dB, it is too high. One reason why the measured results are not similar to the simulated radiation patterns is because it is difficult to set up the horn positions precisely where they need to be for the measurement.

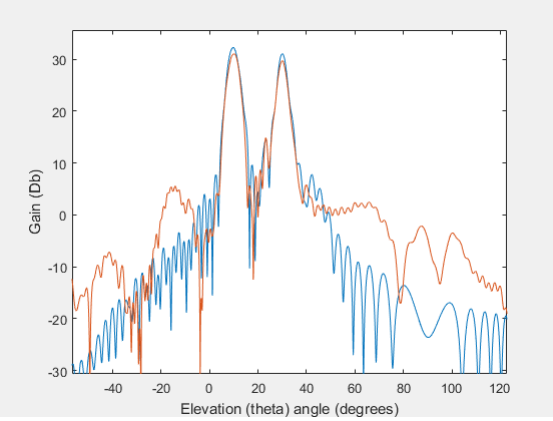

Figure 4.53: Medium near field area simulation results

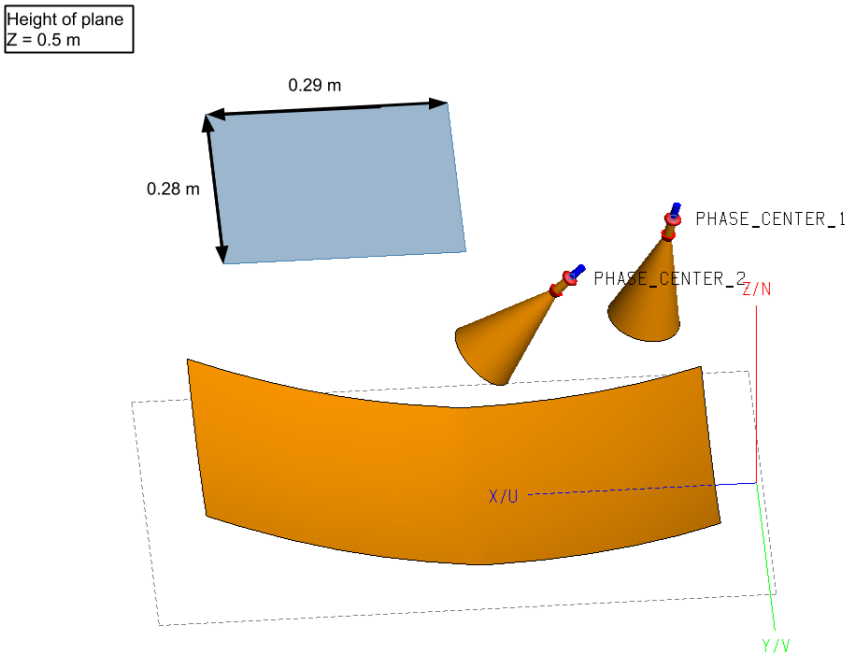

Figure 4.54: Small near field area simulation set up

Additionally, it could also be that the horn's phase centre is not exactly in the focus point of the reflector.

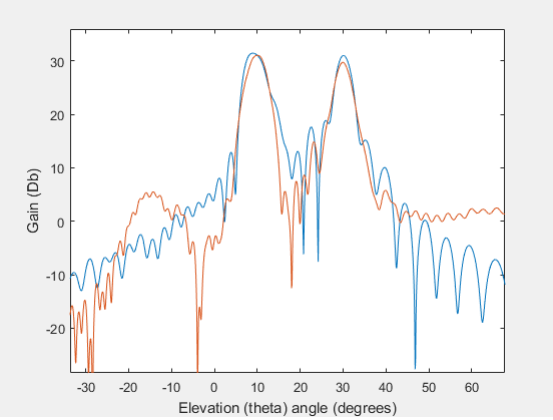

Figure 4.55: Small near field area simulation results

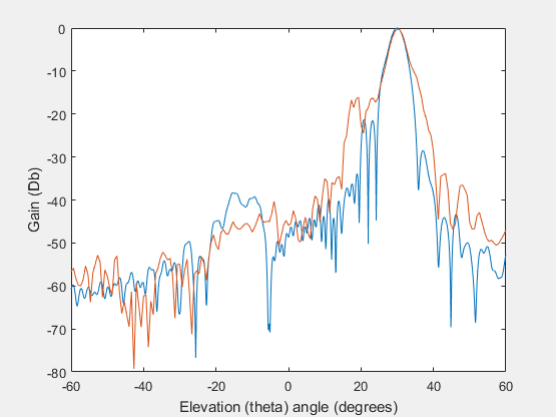

Figure 4.56: Measured results compared with simulation at 30°

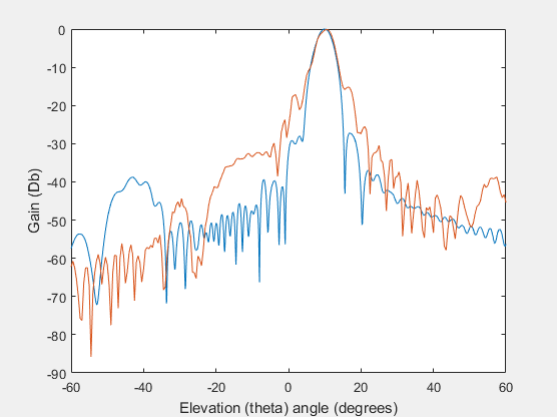

Figure 4.57: Measured results compared with simulation at 10°

Chapter 5

Conclusion

In this thesis an antenna solution for a low-cost water vapour radiometer had to be found. The design had to be able to be electronically steered to observe into a certain direction; needed to have a sidelobe level of lower than -20 dB and a -3 dB beamwidth lower than 3°. The initial focus was on designing a phased array, since phased arrays can be electronically steered. An investigation was done into how many elements would be required for a phased array to reach the specifications, or even come close to them, and was found to be too many to be feasible at the number of elements required being 16x16. A 2x2 and a 1x4 multilayered aperture coupled patch antenna array with a corporate feed network was designed in FEKO to test the reliability of the investigation and to see if a better patch design and a feed network can improve the result, however, this also proved that an array design was not feasible.

A reflector system was then considered. The problem of needing to be steered was solved by having multiple reflectors with associated horn feeds statically observe in the different directions required. Mechanical steering was not possible as maintenance costs on the mechanical components would be too high for a low cost system. Two reflectors was designed in GRASP and merged into one large reflector through interpolation. The design was then exported to FEKO where a conical horn was designed. After this design proved ineffective a new horn was used. This new horn was bought instead of designed as the cost of manufacturing would be similar. Two models in FEKO was designed for the radiation pattern of the bought horn and the physical dimensions of the horn, respectively. This new horn design proved to almost reach specifications at around -18 dB sidelobe level and a -3 dB beamwidth of around 2° which is better than specification. Since the new horn was larger than the old horn, an aperture blockage test was done using the physical dimension model and a PO (not taking aperture blockage into account) and MLFMM (taking aperture blockage into account) simulation, respectively, and comparing them. The result proved that aperture blockage was not notably caused by the new bigger horns.

The system was then measured. The horn was measured using a spherical near field measurement which was then transformed into a far field. The result from this was used to determine the phase centre of the new horn. From this the final horn positions relative to the reflector could be determined and physically set. The reflector system was then measured using a planar near field scan which was then transformed into a far field. The planar near field area to measure was determined from a simulation test to relatively accurately measure the reflector system. The results of the measured system to the simulated system was then compared and the measured system proved to have notably higher sidelobes, however, the main beam -3 dB beamwidth was almost exactly similar. The measured sidelobes were too high at around -16 dB, but the beamwidth was within specification. To reduce the sidelobes a horn with a higher gain can be designed. Additionally, to increase the gain of the system a larger reflector could have been used.

Finally, because it was difficult to position the horn exactly where it needed to be for the measurement, it is possible that the horn's phase centre was not in the reflector's focus point. By changing the horn position in the simulated reflector system and comparing the result with the measured results, it is possible to determine if this was the reason the measured results does not compare well with the simulation results.

List of References

[1] P. Pingree, M. Janssen, J. Oswald, S. Brown, J. Chen, K. Hurst, A. Kitiyakara, F. Maiwald, S. Smith: Microwave Radiometers from 0.6 to 22 GHz for Juno, A Polar Orbiter around Jupiter. 2008. [Online].
Available at: https://trs.jpl.nasa.gov/bitstream/handle/2014/44820/08-0304_A1b.pdf?sequence=1

[2] M. Britcliffe, D. Hoppe, M. Franco: A Low-Cost Water Vapor Radiometer for Deep Space Network Media Calibration. 2012. [Online].
Available at: https://ipnpr.jpl.nasa.gov/progress_report/42-188/188C.pdf

[3] R. Nemiroff, J. Bonnell: Astronomy Picture of the Day. 2006. A Big Dish at the VLA Radio Observatory [Online].
Available at: https://apod.nasa.gov/apod/ap061129.html

[4] HASCO: 22 GHz to 26.5 GHz Lens Corrected Antenna, 22 dB Gain, K Band, WR-42 Wavgeuide. 2017. [Online].
Available at: https://www.hasco-inc.com/millimeterwave-components/22-ghz-to-26-5-ghz-lens-corrected-antenna-22-db-gain-k-band-wr-42-wavgeuide/

[5] SAGE Millimeter: SAL-2232732212-42-S1 Datasheet. 2017. 22 GHz to 26.5 GHz Lens Corrected Antenna, 22 dB Gain, K Band, WR-42 Wavgeuide. [Online].
Available at: https://www.hasco-inc.com/content/Sage_Millimeter/SAL/SAL-2232732212-42-S1_DataSheet.pdf

[6] T. Stander: Low-cost water vapour radiometry. 2017. [Online].
Available at: https://www.eaobservatory.org/jcmt/wp-content/uploads/sites/2/2016/11/WVR-Project.pdf

[7] 2016. Altair Development S.A. (Pty) Ltd, Stellenbosch, South Africa. FEKO 14.0.
Available at: https://altairhyperworks.com/product/FEKO

[8] 2018. Ticra. Copenhagen, Denmark. GRASP 10.6.1.
Available at: https://www.ticra.com/software/grasp/

[9] T. Greicius: Juno Overview. 2018. [Online].
Available at: https://www.nasa.gov/mission_pages/juno/overview/index.html

[10] C. A. Balanis: *Antenna Theory: Anlaysis and Design*. 3rd edn. John Wiley & Sons, Inc., 2005.

[11] Lecture-7. . Dolph Chebyshev array [Online].
Available at: https://nptel.ac.in/courses/117107035/module6/lecture7/lecture7.pdf

[12] Lecture-8. . Chebyshev Array Design [Online].
Available at: https://nptel.ac.in/courses/117107035/module6/lecture8/lecture8.pdf

[13] HMC247. EverythingRF.
Available at: https://www.everythingrf.com/products/analog-phase-shifters/analog-devices/626-29-hmc247

[14] Gendreau Microsystems, Inc. Gendreau Microsystems, Inc.
Available at: http://www.gendreaumicrosystems.com/forms/instant-pcb-design-quote.htm

[15] Cape Town Factory Capabilities And Materials. Trax Interconnect (Pty) Ltd.
Available at: https://www.trax.co.za/capabilities

[16] R. J. P. Douville, D. S. James: Experimental study of symmetric microstrip bends and their compensation. *IEEE Transactions on Microwave Theory and Techniques*, vol. 26, no. 3, Mar 1978.

[17] V. Jamnejad-Dailami, A. Rahmat-Samii: Some important geometrical features of conic-section-generated offset reflector antennas. *IEEE Transactions on Antennas and Propagation*, vol. 28, no. 6, Nov 1980.

[18] J. R. Bergmann, F. J. V. Hasselmann, F. L. Teixeira, C. G. Rego: Comparison between techniques for global surface interpolation in shaped reflector analysis. *IEEE Transactions on Antennas and Propagation*, vol. 42, no. 1, Jan 1994.

[19] C. A. Balanis: *Advanced Engineering Electromagnetics*. 2nd edn. John Wiley & Sons, Inc., 2012.